

ABSTRACT

MA, JIANGUO. Multi-frequency Ultrasound Transducers and Their Applications in Tissue Ablation and Intravascular Acoustic Angiography. (Under the direction of Dr. Xiaoning Jiang).

Ultrasonic wave has been broadly applied to biomedical therapy and diagnosis as a means to deliver energy or information or both. Broadband ultrasound transducers have been increasingly important in advanced imaging and therapy. However, transducers made of high efficiency materials such as Lead zirconium titanate (PZT) or relaxor-based lead titanate (relaxor-PT) single crystals are limited in bandwidth (-6 dB fractional bandwidth less than 100%) because of the material properties and existing transducer designs. In this dissertation research, multi-layer, multi-frequency transducers were designed with the assistance of microwave theory to analyze wave propagation in the transducers, and these transducers were then fabricated and tested for both therapeutic and diagnostic applications.

Firstly, a dual frequency high intensity focused ultrasound (HIFU) transducer was designed with two identical active layers (PZT-2) bonded together, which broke the symmetry of the vibration boundary conditions and generated 1.5 MHz and 3 MHz ultrasonic waves with almost the same amplitudes. Acoustic power outputs of the single or dual frequency waves were calibrated with an acoustic power meter. The tissue ablation with 6 W acoustic power output from this transducer illustrated consistently higher heat generation efficiency with the dual frequency wave than conventional single frequency ones. The high efficiency of dual frequency HIFU tissue ablation indicated the possibility of reducing the energy deposition and ablation time for the same heat generation as in the conventional tissue ablations, which is expected to promote the safety and reduce the cost of the HIFU treatment.

Secondly, dual frequency intravascular ultrasound (IVUS) transducers were investigated with a low frequency (6.5 or 5 MHz) transmitter to excite nonlinear vibration of ultrasound contrast agent (microbubbles) and a high frequency (30 MHz) receiver to detect the super-harmonic responses from microbubbles. An anti-matching layer was sandwiched between the two active elements to suppress the aliasing echo in high frequency receiving waves and to enhance the low frequency wave propagation. Microwave theory were introduced to demonstrate the wave propagation in the multi-layer transducers. The transmitter (6.5 MHz or 5 MHz) was evaluated by a hydrophone and at least 1 MPa pressure was generated. The receiver was characterized by pulse echo experiment, and it showed the loop sensitivity of -27 dB and the -20 dB pulse length of 116 ns. Aliasing echo was suppressed to -23.7 dB compared to the target reflection signal. Imaging result elucidated the detection of a cellulose micro-tube (mimicking vasa vasorum) with diameter of 200 μm . The measured length of the pulses received from microbubbles was equivalent to about 70 μm , indicating its capability of high resolution intravascular acoustic angiography, which is promising for assessment of plaque vulnerability and diagnosis of atherosclerotic cardiovascular disease.

In conclusion, multi-frequency ultrasound exhibited unique performances which can be significant in biomedical applications for both therapy and diagnosis. The wave propagation control methods in the multi-layer transducers were successfully demonstrated for development of advanced multi-frequency ultrasound transducers. Specific dual frequency HIFU transducers were studied to achieve high efficiency heat generation for enhanced tissue ablations, and the dual frequency IVUS transducers were demonstrated for vasa vasorum imaging and acoustic angiography for vulnerable plaque identifications.

© Copyright 2014 Jianguo Ma

All Rights Reserved

Multi-frequency Ultrasound Transducers and Their Applications in Tissue Ablation and
Intravascular Acoustic Angiography

by
Jianguo Ma

A dissertation submitted to the Graduate Faculty of
North Carolina State University
in partial fulfillment of the
requirements for the degree of
Doctor of Philosophy

Mechanical Engineering

Raleigh, North Carolina

2014

APPROVED BY:

Dr. Yun Jing

Dr. Michael B. Steer

Dr. Paul A. Dayton

Dr. Xiaoning Jiang
Chair of Advisory Committee

DEDICATION

To my parents and family with love.

To Chinese Scholarship Council that supported students for advanced education.

BIOGRAPHY

Jianguo Ma received his B.S. degree and the M.S. degree both from School of Physics, Shandong University, China, in 2008 and 2011, respectively. He joined Dr. Xiaoning Jiang's Micro/Nano Engineering Laboratory in 2011 and has since been pursuing his Ph.D. degree in the Department of Mechanical and Aerospace Engineering (major) and Department of Electrical and Computer Engineering (minor) in North Carolina State University, Raleigh, NC. His main research interests include multi-frequency ultrasound transducers for biomedical applications, particularly the wave control methods associated with microwave networks.

ACKNOWLEDGMENTS

Foremost, I would like to express my sincere gratitude to my advisor Dr. Xiaoning Jiang for the continuous support of my Ph.D. study and research. His patience, motivation, enthusiasm, carefulness assures the research being done in the correct direction and in the scheduled pace. Training under his advice leads me to be closer towards an independent researcher. Besides, his kindness makes the research group as a family.

I appreciate Dr. Yun Jing for his erudition on acoustics that helped me on my research. The techniques of acoustics he offered are essential for the ultrasound applications in this research.

I would sincerely thank Dr. Michael B. Steer, who not only provided me the knowledge needed to fulfill my research as a microwave designer, but also led us to respect Mother Nature, and follow the rules of her instead of fight against her.

I'm greatly thankful to Dr. Paul A. Dayton, who advised me on therapy and diagnosis applications with ultrasound. His guidance and the biomedical platform in his lab were inseparable from this research.

Thanks to all lab members of the Micro/Nano Engineering Lab, Laura Tolliver, Seol Ryung Kwon, Shujin Huang, Hui Zhang, Wenbin Huang, Sijia Guo, Baoyu Hsieh, Kyungrim Kim, Saurabh Bakshi, Sibon Li, Zhuochen Wang, Jinwook Kim, Weiyi Chang, Taeyang Kim, Joseph Johnson, Longlong Shu, Xiaohua Jian, Di Wu, Won Tae Kwon and Yongbin Liu, together with collaborating members, Karl H. Martin (UNC-CH), Qifa Zhou (USC), and Yang Li (USC).

Last but not least, my special thanks are given to my parents, who have been offering me everlasting love and support over the time and space.

TABLES OF CONTENTS

LIST OF TABLES.....	viii
LIST OF FIGURES.....	ix
Chapter 1. Introduction	1
1.1 Piezoelectricity	2
1.1.1 Piezoelectric effect.....	2
1.1.2 Piezoelectric materials for ultrasound transducers.....	14
1.2 Ultrasonic wave.....	26
1.2.1 Theory and terminologies.....	26
1.2.2 Interaction between ultrasound and tissue medium	36
1.3 Medical applications of ultrasound.....	39
1.3.1 High intensity focused ultrasound	39
1.3.2 Imaging ultrasound	40
1.4 Microwave.....	42
1.4.1 Transmission line	42
1.4.2 Smith chart.....	46
1.4.3 Impedance matching	48
1.5 Dissertation structure	50
Chapter 2. Dual Frequency High Intensity Focused Ultrasound Transducer	52
2.1 Background.....	52
2.2 Theoretical analysis.....	54
2.2.1 Single layer vibration	54
2.2.2 Double layer resonator	57
2.3 Dual frequency transducer.....	59
2.3.1 Transducer design.....	59
2.3.2 KLM modeling	61
2.3.3 Acoustic field simulation.....	61

2.3.4	Fabrication	62
2.3.5	Transducer characterization	64
2.4	Tissue ablation.....	65
2.5	Results and discussion.....	69
2.5.1	Transducer prototype	69
2.5.2	Electrical characteristics	70
2.5.3	Pulse-echo test.....	72
2.5.4	Beam profile.....	73
2.5.5	Tissue ablation	78
2.6	Summary	80
Chapter 3.	Dual Frequency Intravascular Super-Harmonic Imaging Transducer	82
3.1	Background.....	82
3.2	Dual frequency IVUS transducer	86
3.2.1	Transducer design.....	86
3.2.2	Fabrication	93
3.2.3	Acoustic characterization.....	95
3.3	Imaging tests	96
3.3.1	Microbubble response test.....	96
3.3.2	Fundamental imaging	98
3.3.3	Super-harmonic imaging.....	99
3.4	Preliminary results	100
3.4.1	Prototype and housing.....	100
3.4.2	Electrical characterization.....	101
3.4.3	Acoustic characterization.....	103
3.4.4	Microbubble response	107
3.4.5	Fundamental imaging	111
3.4.6	Super-harmonic imaging.....	112
3.5	Performance optimization	114

3.5.1	Optimization approaches.....	114
3.5.2	Transmission output	116
3.5.3	Imaging results.....	119
3.6	Summary	122
Chapter 4.	Acoustic Filter Layer Design with Microwave Analysis.....	126
4.1	Microwave analysis of piezoelectric transducers	127
4.1.1	Electrical-mechanical equivalence.....	127
4.1.2	Quarter wavelength impedance inverter	130
4.2	Anti-matching layer for high frequency receiving wave	133
4.2.1	Requirement of an anti-matching layer.....	133
4.2.2	Mechanism analysis	136
4.2.3	Microwave analysis.....	138
4.3	Passive amplifier for the low frequency transmitting wave	145
4.4	Summary	155
Chapter 5.	Conclusion.....	157
5.1	Dual frequency transducer for HIFU	157
5.2	Dual frequency intravascular transducer for acoustic angiography	158
5.3	Acoustic filter layer design	161
5.4	Suggestions for future work on dual frequency IVUS transducers.....	163
REFERENCES	165

LIST OF TABLES

Table 1.1 Piezoelectric parameters and coefficients.....	7
Table 1.2 Properties of the piezoelectric materials discussed above.....	20
Table 2.1 Summary of vibration modes of the transducer.....	60
Table 2.2 Parameters of the materials on the transducer	63
Table 2.3 Beam profile of the acoustic field. Beam width and depth are referred to -3dB value.	76
Table 2.4 Voltage to be applied to the transducer to generate 6 W acoustic power.....	78
Table 3.1 Typical parameters of some candidate piezoelectric materials	91
Table 3.2. Fabrication parameters of the dual frequency transducer.....	92

LIST OF FIGURES

Figure 1.1 Schematic diagram of electrostrictive material a) at the initial shape, b) and c) with external electric field, and d) with external mechanical compression.	3
Figure 1.2 Classification of the dielectric materials.	3
Figure 1.3 Schematic diagram of the reverse piezoelectricity: a) at the initial shape without external electric field; b) expanded by external forward electrical field; and c) compressed by reverse electric field.	4
Figure 1.4 Schematic diagram of the direct piezoelectricity: a) at the initial shape without external pressure; b) being stretched by external force; c) being compressed by external force.	5
Figure 1.5 a) Mechanical schematic diagram of the dynamic behavior of the piezoelectric material and b) the electrical equivalent circuit. c) Impedance response of the vibrating system.	11
Figure 1.6 Coordinate system used to indicate the piezoelectric constants.	13
Figure 1.7 Perovskite structure of the PZT material a) in a cubic shape at $T > T_C$ and b) in polarized shape at $T < T_C$. c) Phase transformation of PZT dependent on the composition and temperature.	16
Figure 1.8 Schematic diagram of the carbon chain of PVDF polymer.	18
Figure 1.9 Structure of piezoelectric 1-3 composite consisting of active posts and passive filling materials (usually epoxy).	22
Figure 1.10 Schematic diagram of 1-D wave propagation.	28
Figure 1.11 Standing wave vibration modes of the free-free, fixed-fixed, and fixed-free boundary conditions.	31
Figure 1.12 a) Reflection and transmission of ultrasonic wave at impedance boundaries. b) Scattering of acoustic wave at particles smaller than the wavelength.	33
Figure 1.13 Schematic diagram of the transmission line circuit.	43
Figure 1.14 Example of a) an impedance Smith chart and b) an admittance Smith chart.	47
Figure 1.15 Locus of a transmission line in the Smith chart.	49

Figure 2.1 Configuration of a) single layer and b) double layer transducers.	55
Figure 2.2 Vibration modes of a single layer transducer. Values on Y-axis indicate the relative displacement in each mode. L is the thickness of the active (piezo) material.	56
Figure 2.3 Additional vibration modes of a double layer transducer. Values on Y-axis indicate the relative displacement in each mode. L is the total thickness of 2-layer piezo material....	58
Figure 2.4 Configuration of the dual frequency transducer. Arrows on the transducer indicate the polarization direction.	60
Figure 2.5 Signal waveforms generated by the function generator. a) 1.5 MHz signal. b) 3 MHz signal. (c-f) dual frequency signals. The rate of amplitudes between 1.5 MHz and 3 MHz is c) 1:1, d) 1:3, e) 1:5 and f) 1:10 respectively.....	68
Figure 2.6 Photograph of the fabricated dual frequency transducer.....	69
Figure 2.7 Impedance and phase of the transducer with a) both layer excitation and b) front layer excitation.....	70
Figure 2.8 Acoustic pressure output with 5-cycle burst input at a) 1.5 MHz and b) 3 MHz..	71
Figure 2.9 a) Reflected waveform and b) FFT of the waveform in pulse-echo test.	73
Figure 2.10 Ultrasound beam profile with frequency of a) & b) 1.5 MHz, c) & d) 3 MHz and e) & f) dual frequency. Figures a), c) and e) are from simulation while b), d) and f) are from hydrophone measurement. g) Color bar is shared by all the figures.	75
Figure 2.11 Acoustic pressure generated by the transducer with different frequency configurations. In this case, the dual frequency means 1.5 MHz and 3 MHz with 1:1 amplitude ratio.	77
Figure 2.12 Porcine tissue ablation tests using single-frequency ultrasound and dual frequency ultrasound with different frequency components under the same power (6 W). In the figure, single frequency ablations are shown with 1.5 MHz and 3 MHz for corresponding frequency. For dual frequency ablations, relative amplitude ratios of 1.5 MHz and 3 MHz are shown as 1:1 and 1:10.....	79
Figure 3.1 Structural dual frequency transducer design alternatives.....	87
Figure 3.2 Beam profile of the low frequency transmitter in the interleaved structure transducer.	88
Figure 3.3 Side view of the dual frequency IVUS transducer design.....	90

Figure 3.4 Fabrication process diagram of the dual frequency transducer.	94
Figure 3.5 Microbubble size distribution.....	97
Figure 3.6 Experimental setup for the imaging.	99
Figure 3.7 Prototype transducers a) housed on the tip of a 20 gauge hypodermic needle or b) integrated in a commercial catheter.	101
Figure 3.8 Electrical impedance of the a), b) 6.5 MHz element and c), d) 30 MHz from a), c) KLM modeling and b), d) measurement from impedance analyzer.	102
Figure 3.9 Peak rarefractional pressure at the contrast imaging area, 3 mm away from the center of the transducer, using a 5-cycle burst excitation on the low frequency (6.5 MHz) element at varied voltages.	103
Figure 3.10 Bema profile of the transmitter with strong pressure at the middle.	104
Figure 3.11 Pulse-echo response and its FFT spectrum of 30 MHz element in a) modeling and b) measurement. The aliasing echoes are marked by the red ellipses.	105
Figure 3.12 Transmission (2-cycle burst) and receiving (pulse-echo) bandwidth separation.	106
Figure 3.13 Amplitude of nonlinear microbubble response with sinusoidal bursts of a) 1-cycle, b) 2-cycle and c) 5-cycles at different voltage excitations.	108
Figure 3.14 Spectrum of microbubble responses at 70 V with a burst of a) 1-cycle, b) 2-cycles, c) 3-cycles, d) 4-cycles, e) 5-cycles. The spectrum of a water filled tube at 70 V with a burst of f) 5-cycles shown for comparison.	110
Figure 3.15 Fundamental imaging at 30 MHz.	111
Figure 3.16 Super-harmonic imaging of the microbubble tube and a steel rod.....	113
Figure 3.17 Setup of vasa vasorum imaging in vitro. Phantom was used to mimic the coronary vessel wall and an acoustically transparent micro-tube was used to mimic the vasa vasorum.	116
Figure 3.18 Transmission sensitivity of the prototype transducers with the transducers shown at the left and the excitations shown at the top. All the values are normalized to unit voltage as kPa/V.....	117

Figure 3.19 Comparison of contrast imaging with the a) 6.5 MHz and b) 5 MHz transmitters, both of which were made of PMN-PT single crystals are excited by 2-cycle bursts. 120

Figure 3.20 Comparison of contrast imaging with the 5 MHz transmitters made of PMN-PT single crystal and PMN-PT 1-3 composite. Both were excited by 1-cycle burst. 122

Figure 4.1 Schematic diagram of transmission and reflection in a 3-layer structure. 130

Figure 4.2 Demonstration of matching (blue solid line) and anti-matching (red dash line) effect of the quarter wavelength impedance inverter. 132

Figure 4.3 Aliasing echo generation. a) Schematic diagram; b) signal detected by the receiver. 134

Figure 4.4 Anti-matching (acoustic filter) design for the high frequency receiving wave. a) Structure of the dual frequency transducer; b) equivalent circuit for the high frequency wave propagation. 138

Figure 4.5 Simulation circuit of the anti-matching layer with different characteristic impedances. 141

Figure 4.6 Loci of the quarter wavelength anti-matching layer. The numbers in the legend followed by “AM” indicate the relative impedance of the anti-matching layer. 142

Figure 4.7 Insertion loss of the anti-matching layer dependent on the relative impedance Z_{AF}/Z_{LA} (values labeled in legend) and thickness L_{AF} (x-axis). 143

Figure 4.8 Insertion loss of the anti-matching layer with attenuation (in dB/cm/MHz) labeled as legend numbers followed by “A”. Relative impedance of the passive amplifier is 0.157 (from actual case). 143

Figure 4.9 High frequency pulse-echo response on transducer prototypes, a) without anti-matching layer and b) with anti-matching layer. 145

Figure 4.10 Passive amplifier (acoustic filter) design for the low frequency receiving wave. a) Structure of the dual frequency transducer; b) equivalent circuit for the low frequency wave propagation. 148

Figure 4.11 Simulation circuit of the passive amplification layer with typical parameters from the dual frequency transducer. 149

Figure 4.12 Loci of the input impedance of the front layers (high frequency matching, high frequency active and the passive amplifier layers). The numbers ahead of the underscores are the thickness of the high frequency active layer relative to low frequency wavelength. Numbers

followed the underscores are the corresponding passive amplifier thickness that make Z_{L3} zero phase. Relative impedance of the passive amplifier is 0.157 (from actual case)..... 152

Figure 4.13 Gain of the passive amplifier with different thicknesses of the high frequency active layer and passive amplifier layer. Relative impedance of the passive amplifier is 0.157 (from actual case)..... 153

Figure 4.14 Pressure amplitude measured from the traditional matched (transducer A, quarter wavelength matching) and transducer with high frequency active and acoustic layer (transducer E, P1 & AF) normalized to that without matching layers (No matching). 154

Figure 4.15 Gain of transmitting pressure output on the fabricated transducers normalized to that without matching layers. 155

Chapter 1.

Introduction

Piezoelectric ultrasound transducers have been widely utilized in biomedical applications as energy transduction between electrical and mechanical forms [1, 2]. According to recent research [3, 4], very broadband (-6 dB fractional bandwidth > 100%) ultrasound suggested promising features in both therapy and diagnosis. However, conventional transducer designs using high efficiency piezoelectric materials such as Lead zirconium titanate (PZT) ceramics or relaxor-based lead titanate (relaxor-PT) single crystals were limited in bandwidth (-6 dB fractional bandwidth < 100%). In order to take the advantage of the broadband ultrasound wave, multi-layer, multi-frequency transducers were investigated in this research. Vibration modes in the multi-frequency transducers are relatively complex compared to single frequency transducers. To make the analysis more intuitive, the multi-layer transducer was analyzed as a microwave circuit with transmission lines. In this chapter, background of the related information was introduced, including the piezoelectricity, ultrasonic wave, medical applications of ultrasound, and microwave theory. At the end of this chapter, a brief introduction of the dissertation structure was described.

1.1 Piezoelectricity

1.1.1 Piezoelectric effect

Background

An electrical insulator can be polarized by an applied electric field \vec{E} . Electric charges inside the material do not flow freely or accumulate at the surfaces as a conductor, but just shift slightly by the external electric field from their equilibrium positions. As the positive and negative charges shift towards opposite directions, the material shows net negative charge at the high electric potential side and positive charge at the low electric potential side. This phenomenon is dielectric polarization, which is defined as $\vec{P} = \epsilon_0 \chi \vec{E}$, where ϵ_0 is the dielectric constant in vacuum and χ is the electric susceptibility. The dielectric polarization generates an internal electric dipoles that compensate the external electric field and result in a lower electric field inside the material. If the material is originally centro-symmetric or isotropic, then the material can be deformed by the external electrical field because of polarization, and this effect is denominated as the electrostrictivity, as shown in Figure 1.1. The dipoles are generated by external force, so the material is always elongated by the external electric field (Figure 1.1 b and c). Mechanical compression could not generate charges on the surfaces because there are no inherent dipole if external electric field is absent (Figure 1.1 d). A classification of the dielectric materials is shown in Figure 1.2.

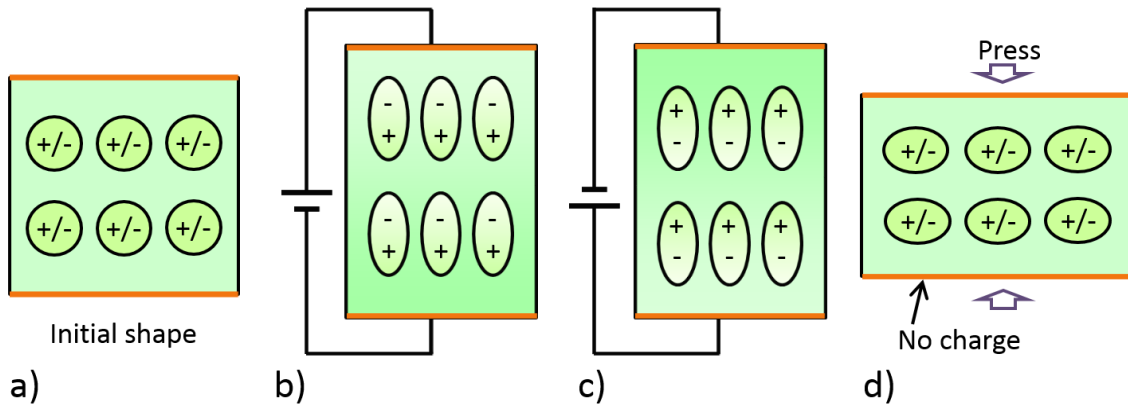


Figure 1.1 Schematic diagram of electrostrictive material a) at the initial shape, b) and c) with external electric field, and d) with external mechanical compression.

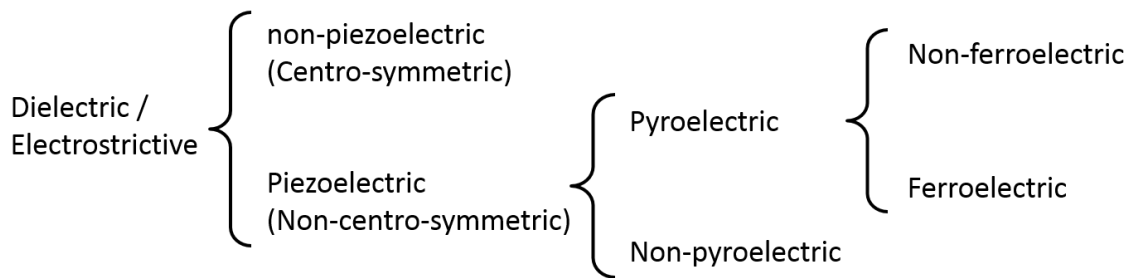


Figure 1.2 Classification of the dielectric materials.

On the contrary if the material is non-centrosymmetric (Figure 1.3 a), the external electric field could either expand (Figure 1.3 b) or compress (Figure 1.3 c) the material with a relatively large deformation compared to electrostrictive effect. The non-centrosymmetry of the material indicates the fact that the positive charge center does not overlap the negative one. An applied external source pushes the positive center to the low potential direction while pushing the negative center to the positive direction. As a result, the material expands if the external electric

field is the same as the polarization of the material and shrinks if it is reversed. Such electric field-induced deformation is denominated as reverse piezoelectric effect and such material is denominated as piezoelectric material. If the polarization is sensitive to temperature, then the material is pyroelectric material. Some pyroelectric materials are ferroelectric materials, the characteristics of which are that the polarization can be reversed by external electric field, and residual polarization exists after the external electric field is removed. Most high performance piezoelectric materials are ferroelectric materials, such as Lead zirconium titanate (PZT) or relaxor-based lead titanate (relaxor-PT) such as lead magnesium niobate-lead titanate (PMN-PT). Relationships among these materials are shown in Figure 1.2.

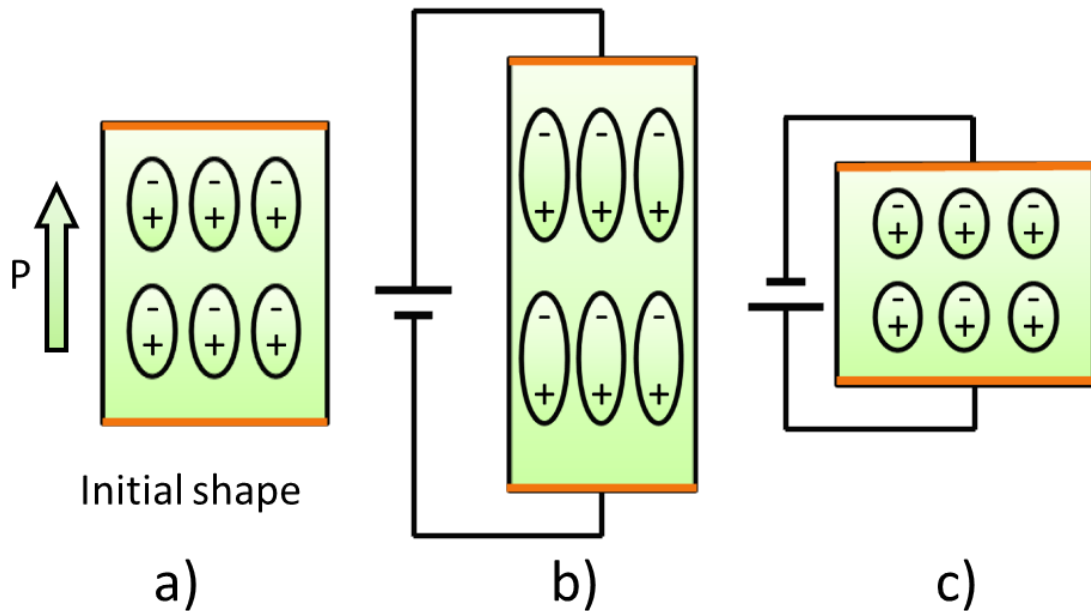


Figure 1.3 Schematic diagram of the reverse piezoelectricity: a) at the initial shape without external electric field; b) expanded by external forward electrical field; and c) compressed by reverse electric field.

Applying force on the piezoelectric material in the polarization direction, electric charges are generated. This is the direct piezoelectric effect found by Curie brothers [5] earlier than the reverse piezoelectric effect. In steady state (Figure 1.4 a), the internal diversion of positive and negative charge center is neutralized by the ambient charges so that there are no net charges on the surfaces. The applied external force pushes the two charge centers closer (Figure 1.4 c) or pull them farther (Figure 1.4 b), breaking the neutralization and generating net charges at surfaces of the piezoelectric material. The direct and reverse piezoelectric effects are the opposite scenarios that transduce the energy between electrical and mechanical form.

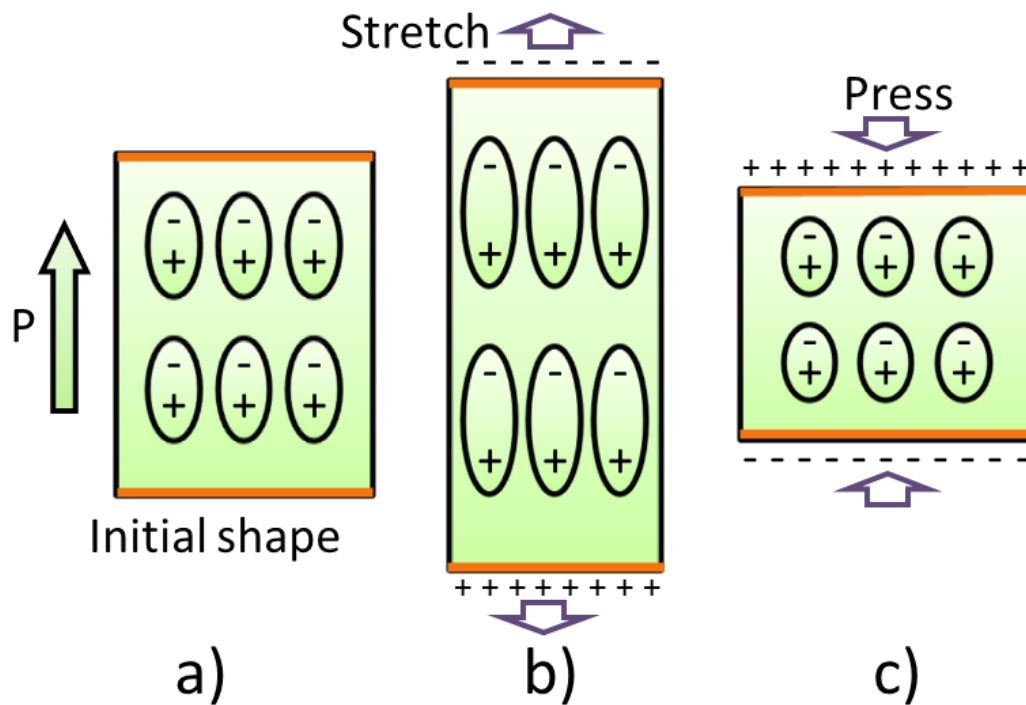


Figure 1.4 Schematic diagram of the direct piezoelectricity: a) at the initial shape without external pressure; b) being stretched by external force; c) being compressed by external force.

Theory and terminologies

Piezoelectric equations are employed to illustrate such an electro-mechanical coupling effect. The electrical parameters consist of electric field and electric displacement, which are related by the electrical coefficients such as dielectric permittivity, electric susceptibility and so on. The mechanical parameters consist of stress and strain, which are related by elastic stiffness and compliance. The piezoelectric coefficients are those coupling the electrical and mechanical parameters. A collection of the parameters and coefficients are shown in Table 1.1. The two units for d , g , e , and h respectively are equivalent taken the identity of $[V] = [N \cdot m / C]$.

Table 1.1 Piezoelectric parameters and coefficients.

Parameters and coefficients	Symbols	Units
Stress	T	N/m ²
Strain	S	-
Electric field	E	V/m
Electric flux density	D	N/m ²
Polarization	P	C/m ²
Elastic stiffness	<i>c</i>	N/m ²
Elastic compliance	<i>s</i>	m ² /N
Dielectric permittivity	ϵ	F/m
Electric susceptibility	χ	-
Relative permittivity	ϵ_r	-
$\frac{\text{polarization}}{\text{stress}}$ or $\frac{\text{strain}}{\text{electric field}}$	<i>d</i>	C/N or m/V
$\frac{\text{electric field}}{\text{stress}}$ or $\frac{\text{strain}}{\text{polarization}}$	<i>g</i>	V•m/N or m ² /C
$\frac{\text{polarization}}{\text{strain}}$ or $\frac{\text{stress}}{\text{electric field}}$	<i>e</i>	C/m ² or N/V•m
$\frac{\text{electric field}}{\text{strain}}$ or $\frac{\text{stress}}{\text{polarization}}$	<i>h</i>	V/m or N/C
Electromechanical coupling	<i>k</i>	-

Without piezoelectricity, the dielectric properties and the mechanical deformation properties are isolated. For electric properties, the relationships among dielectric parameters are $\vec{D} = \varepsilon_0 \vec{E} + \vec{P} = \varepsilon_0 \varepsilon_r \vec{E}$, where the relative permittivity is $\varepsilon_r = 1 + \chi$. For mechanical properties, the relationship between strain and stress is governed by Hooke's Law $S = sT$ or $T = cS$ ($s = 1/c$).

Taking the piezoelectricity into account, the electrical and mechanical parameters are all coupled together by the electromechanical coupling coefficients d , g , e and h . In the calculation of parameters in one field (electrical or mechanical), boundary conditions in the other field (mechanical or electrical) need to be defined as well.

The electrical parameters are calculated by defining the mechanical boundary condition as "free" or "clamped". If the material is mechanically free, then the stress (pressure) is constant while movement is free at the surface. The electrical parameters are

$$D = \varepsilon^T E + dT, \quad (1.1)$$

$$E = D / \varepsilon^T - gT, \quad (1.2)$$

where the superscripts $()^T$ indicate the constant stress. If the material is clamped, then the boundaries of the material are fixed while the stress can vary. In this case, the electrical parameters are

$$D = \varepsilon^S E + eS, \quad (1.3)$$

$$E = D / \varepsilon^S - hS, \quad (1.4)$$

where the superscripts $()^S$ indicate the constant strain.

Similarly, the mechanical parameters are calculated by defining the electrical boundary conditions as “short circuit” or “open circuit”. If the electrical boundary condition is short circuit at surfaces of the material, then the mechanical parameters are

$$S = dE + s^E T, \quad (1.5)$$

$$T = -eE + c^E S, \quad (1.6)$$

where the superscripts $()^E$ indicate the constant electric field (short circuit). If the electrical boundary is open circuit at surfaces of the material, then the mechanical parameters are

$$S = gD + s^D T, \quad (1.7)$$

$$T = -hD + c^D S, \quad (1.8)$$

where the superscripts $()^D$ indicate the constant electric flux (open circuit).

Equations (1.1) – (1.8) are associated with on one another. The relationships among electromechanical coupling coefficients are

$$d = es^E = \varepsilon^T g, \quad (1.9)$$

$$e = dc^E = \varepsilon^S h, \quad (1.10)$$

$$g = hs^D = d / \varepsilon^T, \quad (1.11)$$

$$h = gc^D = e / \varepsilon^S. \quad (1.12)$$

The energy transform efficiency is defined as

$$k^2 = \frac{\text{stored mechanical energy}}{\text{input electrical energy}} \quad (1.13)$$

or

$$k^2 = \frac{\text{stored electrical energy}}{\text{input mechanical energy}}. \quad (1.14)$$

and k denominates the electromechanical coupling factor and indicates the energy transduction efficiency between electrical and mechanical forms. The efficiency can be calculated from the coupling coefficients as

$$k^2 = \frac{d^2}{\varepsilon^T s^E} = \frac{e^2}{\varepsilon^S c^D} = \frac{g^2 \varepsilon^T}{s^E} = \frac{h^2 \varepsilon^S}{s^D}. \quad (1.15)$$

Dynamic behavior of the piezoelectric materials (Figure 1.5 a) could be equivalent to an AC electric circuit for analysis (Figure 1.5 b) [6]. In the equivalent circuit, C_0 is the static capacitance defined as $C_0 = \varepsilon A / d$, where A and d are the area and thickness of the piezoelectric material. Equivalence of the other parameters are labeled in Figure 1.5. The mechanical system includes the external excitation force F , mass M , spring constant K , and the damper R_M . The equivalent electrical system consist of the excitation voltage V , inductor L , the parallel and serial capacitors C_0 and C , and the damper R_E . Equivalences between the two groups are

$$\begin{aligned}
 F &\Rightarrow V \\
 M &\Rightarrow L \\
 \frac{1}{K} &\Rightarrow C \\
 R_M &\Rightarrow R_E \\
 \text{Velocity} &\Rightarrow \text{Current}
 \end{aligned}
 \tag{1.16}$$

Parameters of the equivalence are shown in Figure 1.5.

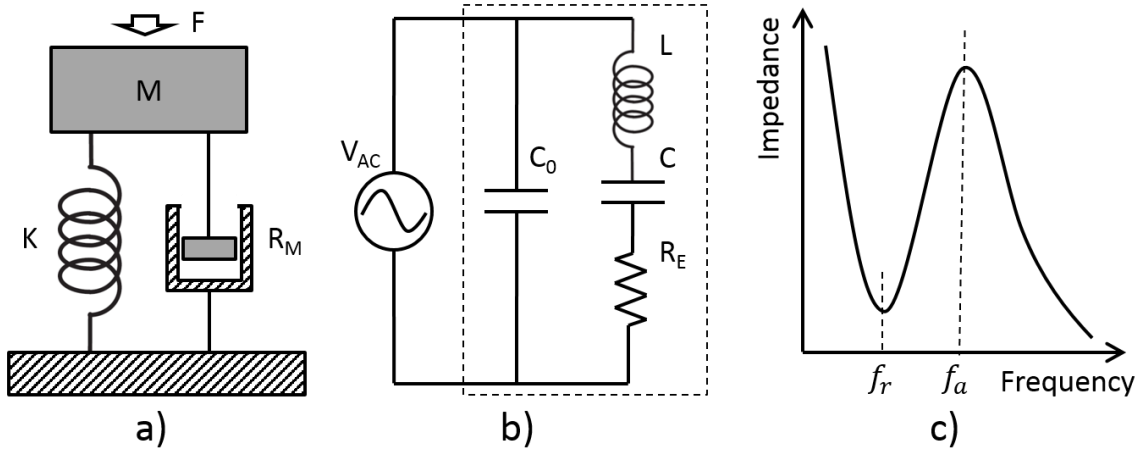


Figure 1.5 a) Mechanical schematic diagram of the dynamic behavior of the piezoelectric material and b) the electrical equivalent circuit. c) Impedance response of the vibrating system.

The impedance of a piezoelectric resonator is a function of the frequency (Figure 1.5 c). The resonant frequency f_r is the frequency with minimum impedance. Losses of most piezoelectric materials are usually sufficiently small ($\sim 1\%$). If the loss is neglected, then the resonant frequency is the LCR serial branch resonance f_s .

$$f_r = f_s = \frac{1}{2\pi} \sqrt{\frac{1}{LC}} . \quad (1.17)$$

The anti-resonant frequency f_a is the frequency of the parallel resonance f_p . Neglecting the loss, the anti-resonant frequency is

$$f_a = f_p = \frac{1}{2\pi} \sqrt{\frac{C + C_0}{LCC_0}} . \quad (1.18)$$

The electromechanical coupling factor k can be calculated from the resonant frequency and anti-resonant frequency, which could be measured by an impedance analyzer.

$$k^2 = \frac{\pi f_r}{2 f_a} \cot\left(\frac{\pi f_a - f_r}{2 f_a}\right) . \quad (1.19)$$

In order to describe the anisotropic piezoelectric materials, all the piezoelectric parameters and coefficients are tensors in the 3D space. Electrical parameters D and E are first-rank tensor (vector) so that ε is a second-rank tensor. In mechanical field, S and T are second-rank tensors so that c and s are fourth-rank tensors. Piezoelectric coefficients correlate the electrical D and E with mechanical S and T , so they are third-rank tensors. In the right-handed Cartesian coordinate system, the X-, Y-, and Z-axes are represented by 1, 2, 3 and the rotations with the X-, Y-, and Z-axis are represented by 4, 5, and 6, respectively (Figure 1.6). For conventional ultrasonic transducers, the poling direction is attributed to axis 3. Based on such definition, the mechanical parameters S and T can be reduced to a 6-value vector, so that all the coefficients could be reduced to second-order tensors (matrices). According to the routine, two numbers

are used as a subscript to indicate the direction of the parameter with the former one denoting electric and latter one denoting mechanical fields. For example, a parameter d_{31} correlates the electric field in the poling direction (3-axis) and the mechanical strain in the lateral direction (1-axis).

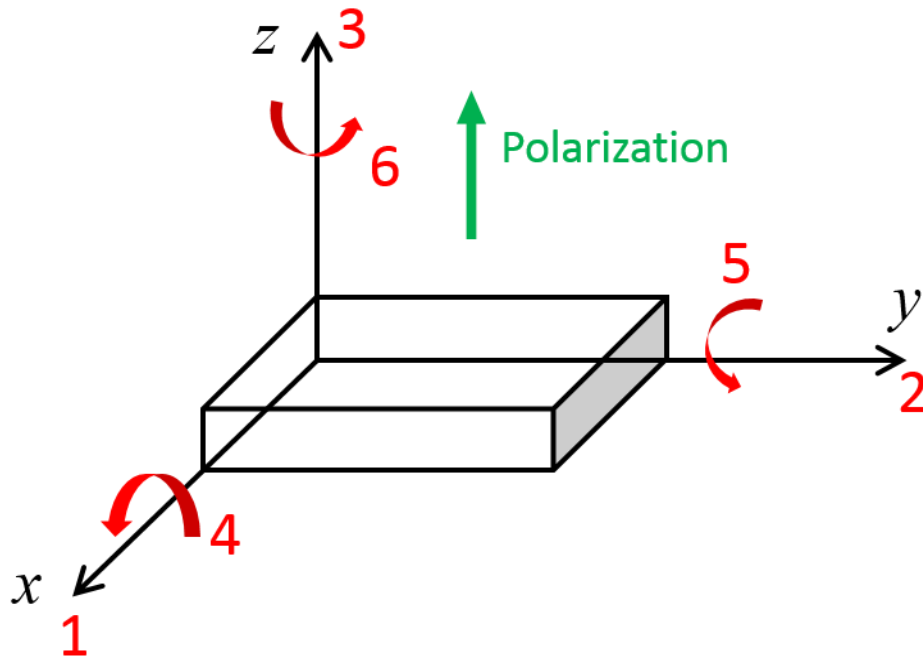


Figure 1.6 Coordinate system used to indicate the piezoelectric constants.

In longitudinal vibrating transducer with both fields corresponding to the poling direction, the coefficient d_{33} is one of the key value indicating the electric field induced strain or stress induced electric flux. The electromechanical coupling factor k_{33} is another critical value

representing the energy transduction efficiency in the longitudinal direction. The k_{33} value is approximately achievable only if the piezoelectric material is not clamped, which requires the shape of the material to be a long (3-axis) bar. In most cases, the piezoelectric materials are used with a shape of thin plate with polarization in the thickness direction (3-axis). In that case, the material is clamped in the lateral direction and the coupling factor is replaced by k_t with the subscript t , representing the thickness mode.

1.1.2 Piezoelectric materials for ultrasound transducers

Taking advantage of the transduction capability between electrical and mechanical energy, piezoelectric materials are widely used in for ultrasonic wave (> 20 kHz) generation from electrical wave input, or electrical wave generation from mechanical wave input. Piezoelectric materials consist of many forms of materials, including crystal, ceramic, polymer, and composites of piezoelectric material with passive polymers.

Introduction of piezoelectric materials

Quartz, a piezoelectric crystal, was the first material found with piezoelectricity, which is one of the few naturally available piezoelectric materials. Quartz exhibits extremely high ($\sim 10^4$ order) quality factor (Q factor), together with good reliability, long life and very low dependency on temperature. Consequently, quartz could provide extremely stable frequency output, which has been widely used for watch and electrical oscillation clocks for digital circuit. Quartz was also used as ultrasound transducers for tissue ablation [7] and marine sonar in early

days. However, the piezoelectric performance of quartz is very low, with $d_{33} \sim 2pC / N$ and $k_t \sim 0.07$. Quartz was seldom used for ultrasound transducer any more after PZT was developed around 1952.

PZT, $Pb[Zr_{1-x}Ti_x]O_3$ ($0 \leq x \leq 1$), is a ceramic with perovskite crystal structure (Figure 1.7 a, b) that exhibits much higher piezoelectric properties than natural piezoelectric materials [8] and, therefore, was the most widely used as active material for ultrasound transducers after being developed. Structure of PZT depends on both the percentage of Ti ($\frac{Ti}{Zr + Ti}$ in mol) and the temperature of the material (Figure 1.7 c) [9]. At temperature higher than the Curie temperature T_c ($\sim 350^\circ C$), PZT is a cubic structure (Figure 1.7 a) without polarization and therefore no piezoelectricity. Below Curie temperature, PZT exhibits polarization (Figure 1.7 b) and it performs the best piezoelectricity at a Ti percentage of 48 ~ 52%, close to the morphotropic phase boundary (MPB). For different applications, PZT materials are modified to induce domain wall motions for different properties. If donors are doped, metal (cation) vacancies are generated to produce high piezoelectric properties, with the expense of larger loss due to the internal friction. The high piezoelectric coefficients, high loss, donors doped PZTs are usually named as “soft PZT”, which are used in low power applications such as imaging transducers to take advantage of the performance without being damaged by the high loss. Typical piezoelectric constants of soft PZT are $d_{33} \sim 400 - 700pC / N$, loss $\sim 1 - 2.2\%$, and $k_{33} \sim 0.7 - 0.75$. On the contrary, if the PZT is doped with acceptors, oxygen (anion) vacancies are generated, lowering the loss but sacrificing the piezoelectric properties of PZT.

The acceptor doped PZTs are usually named as “hard PZT”, which are typically used in high power applications to avoid heat generation from the high loss even with compromised piezoelectric properties. Typical piezoelectric constants of hard PZT are $d_{33} \sim 200-350 \text{ pC/N}$, loss $\sim 0.2-0.5\%$, and $k_{33} \sim 0.68-0.7$. Actually, there is no strict threshold between soft PZT and hard PZT. Various doping recipes were used to cover the performances range from soft PZT to hard PZT.

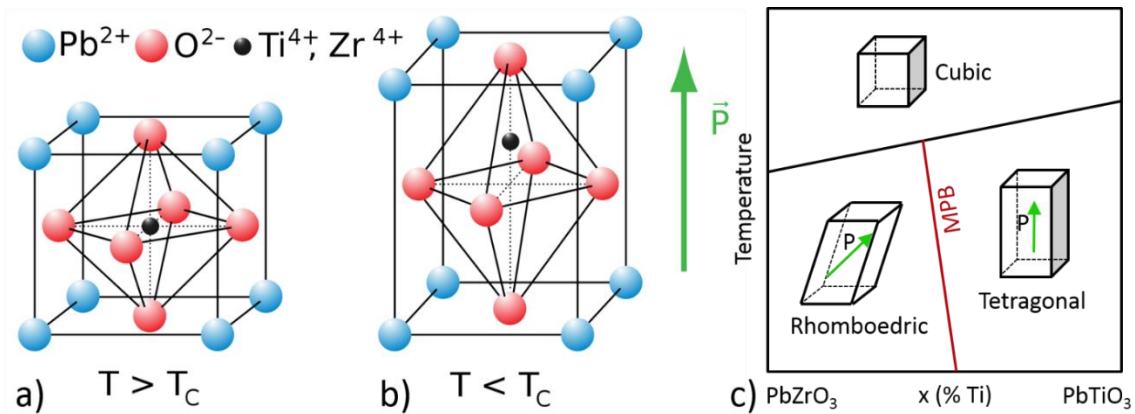


Figure 1.7 Perovskite structure of the PZT material a) in a cubic shape at $T > T_c$ and b) in polarized shape at $T < T_c$. c) Phase transformation of PZT dependent on the composition and temperature.

Relaxor based ferroelectric single crystal [10] is a group of piezoelectric material possessing extraordinary piezoelectric properties, $d_{33} > 2500 \text{ pC/N}$, $k_t \sim 0.6$, and $k_{33} > 0.9$. This group of relaxor-PT based crystals include $\text{Pb}[\text{Mg}_{1/3}\text{Nb}_{2/3}]\text{O}_3\text{-PbTiO}_3$ (PMN-PT), $\text{Pb}[\text{Zn}_{1/3}\text{Nb}_{2/3}]\text{O}_3\text{-PbTiO}_3$ (PZN-PT), $\text{Pb}[\text{Yb}_{1/2}\text{Nb}_{1/2}]\text{O}_3\text{-PbTiO}_3$ (PYN-PT), $\text{Pb}[\text{In}_{1/2}\text{Nb}_{1/2}]\text{O}_3\text{-PbTiO}_3$

Pb[Mg_{1/3}Nb_{2/3}]O₃-PbTiO₃ (PIN-PMN-PT) and so on [11, 12]. PMN-PT exhibits superior performances ($d_{33} \sim 2800$ pC/N, $k_{33} \sim 0.94$) [13] in the relaxor-PT family and is consequently one of the most widely used material for high end piezoelectric transducers. The drawback of PMN-PT material is the relatively low operation temperature (Curie temperature $T_c = 130 - 170$ °C, phase transformation temperature $T_{rt} = 60-95$ °C), so that other alternative relaxor-PT crystals ($T_c = 200 - 360$ °C, $T_{rt} > 100$ °C) are also widely researched for high temperature applications, although the piezoelectric properties are slightly lower ($d_{33} \sim 1200$, $k_{33} \sim 0.9$) [11, 14]. In addition to the working temperature, the coercive field of relaxor-PT based crystals are usually lower than PZT. Because of the high piezoelectric properties and the relatively more vulnerability to temperature and electric field, relaxor-PT based crystals are preferred for low power imaging transducers, whereas not ideal for high temperature high power applications.

The semi crystalline polymer polyvinylidene fluoride PVDF, $([C_2H_2F_2]_n)$ and the copolymer polyvinylidenedifluoride-trifluoroethylene P(VDF-TrFE) exhibit polarization because of the asymmetry alignment of hydrogen and fluorine atoms (PVDF in Figure 1.8) [15]. As a polymer, PVDF exhibits very different properties from the piezoelectric ceramics or crystals [16]. Characteristic acoustic impedance and stiffness of PVDF are very low, making it an ideal material for acoustic wave reception. Besides, its flexibility and mechanical stability assured that it could be easily manufactured to various shapes. However, its low piezoelectric properties, $d_{33} \sim -30$ pC/N and $k_t \sim 0.15$, limit its utilization where high transmission performances are required. Dielectric constant of PVDF ($\epsilon_r \sim 7$) is much lower than PZT ($\epsilon_r > 1000$) and PMN-PT ($\epsilon_r \sim 4000 - 6000$), leading to a relatively high electrical

impedance for small aperture transducers. P(VDF-TrFE) has similar structure as PVDF but, in some units ($[C_2H_2F_2]$), one of the two hydrogen atoms is replaced by fluorine atoms, which makes the chain unit as ($[C_2HF_3]$). Properties of P(VDF-TrFE) is dependent on the ratio of trifluoroethylene, and the density of P(VDF-TrFE) is usually higher the fluorine atom is heavier than the hydrogen one.

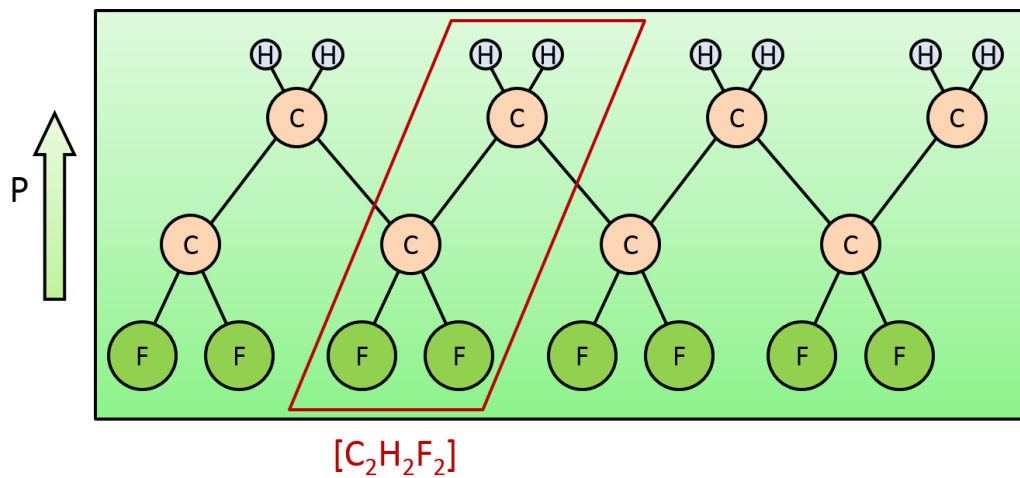


Figure 1.8 Schematic diagram of the carbon chain of PVDF polymer.

Properties of these widely used piezoelectric materials are summarized in Table 1.2. Relaxor-PT based crystals are supreme in the piezoelectric properties, which are widely used for high performance transducers. PZT materials show relatively high piezoelectric constants, and, especially hard PZT, are more robust in high voltage, high temperature ($< 350\text{ }^{\circ}\text{C}$) conditions, so that they are also widely used as sensors, actuators and transducers. PVDF has low piezoelectric properties and high compliance, and, consequently, is usually used as

broadband sensors. Piezoelectricity of quartz is very low so few transducers were made of quartz nowadays. As is shown in the table, k_{33} value differs a lot from k_t for a specific piezoelectric material. As stated previously, a piezoelectric material exhibits k_{33} only if its shape is a long bar in the poling direction. Unfortunately, considering the frequency response, beam forming and electric impedance of the transducers, actual dimensions of the piezoelectric material are commonly in plate shape, the electromechanical coupling factor of which is k_t instead of k_{33} .

Table 1.2 Properties of the piezoelectric materials discussed above.

Piezoelectric material	Piezoelectric constant d (pC/N)	Dielectric constant ϵ_r	Young's Modulus (GPa)	Quality factor	Electromechanical coupling k
Quartz	$d_{33} \sim 2$	3.8	76 – 79	$10^4 - 10^6$	$k_t \sim 0.07$
soft PZT	$d_{33} \sim 400 - 700$	1800 – 5000	~ 60	≥ 30	$k_t \sim 0.5$ $k_{33} \sim 0.7 - 0.75$
hard PZT	$d_{33} \sim 200 - 350$	1000 – 1400	~ 77	≤ 1900	$k_t \sim 0.5$ $k_{33} \sim 0.68 - 0.7$
PMN-PT	$d_{33} \sim 2800$ $d_{31} \sim -1330$	4000 – 6000	~ 18	~ 40	$k_t \sim 0.6$ $k_{33} \sim 0.94$
other relaxor-PT	$d_{33} \sim 900 - 2000$	~ 5000	~ 22	100 – 1300	$k_t \sim 0.6$ $k_{33} \sim 0.9$
PMN-PT 1-3 composite	$d_{33} \sim 2800$ $d_{31} \sim -1330$	~ 3000			$k_t > 0.7$
PVDF	$d_{33} \sim -30$	7	3.5	3 – 10	$k_t \sim 0.15$

In order to benefit from the piezoelectric properties of k_{33} rather than k_t , piezoelectric composites were developed with 1 dimensional connection (poling direction) for piezoelectric material and 3 dimensional connections for the passive filling material (Figure 1.9), and thereby is denominated as 1-3 composite. Excellent features are exhibited by the piezoelectric 1-3 composite. First, the quasi long bar structure of the piezoelectric posts leads to the release of clamp in the lateral dimension so that the composites exhibit approximately k_{33} performance [17, 18]. Second, characteristic acoustic impedance of the materials decreases greatly due to the decrease of acoustic group velocity and density, which results in a much better acoustic impedance match and significantly increases the acoustic wave propagation from the piezoelectric material to the medium (usually water or organic tissue) and vice versa. Third, the lateral resonant frequency were designed to be at least twice of the thickness resonance, so that the periodic structure suppressed the frequency coupling around or lower than the thickness resonant frequency. Various techniques have been developed to fabricate the 1-3 piezoelectric material, including dice-and-fill [17-20], laser micro-machining [21-24], interdigital bonding [25-28], PZT fiber bundling [29], PZT paste molding [30-33] and deep reactive ion etching [34-37]. Dice-and-fill method is easy to realize but is limited within 20 MHz, beyond which undesirable lateral resonance coupling is inevitable regarding to actual blade thickness available. Interdigital bonding method overcomes the operating frequency limitation but is very cost-ineffective. Fiber bundling method is cost-effective but the random distribution of PZT fibers and low volume fraction of PZT result in relatively low performance. PZT molding can't fabricate very high frequency (< 40 MHz) PZT composite either because

thin posts are too brittle when demolding. Both PZT fiber bundling and PZT molding work on PZT only, which could not benefit from the high k_{33} value of relaxor-PT crystal materials. Deep reactive ion etching works especially well for high frequency 1-3 composite fabrication but is cost-ineffective in low frequency composite fabrication because of too long etching time.

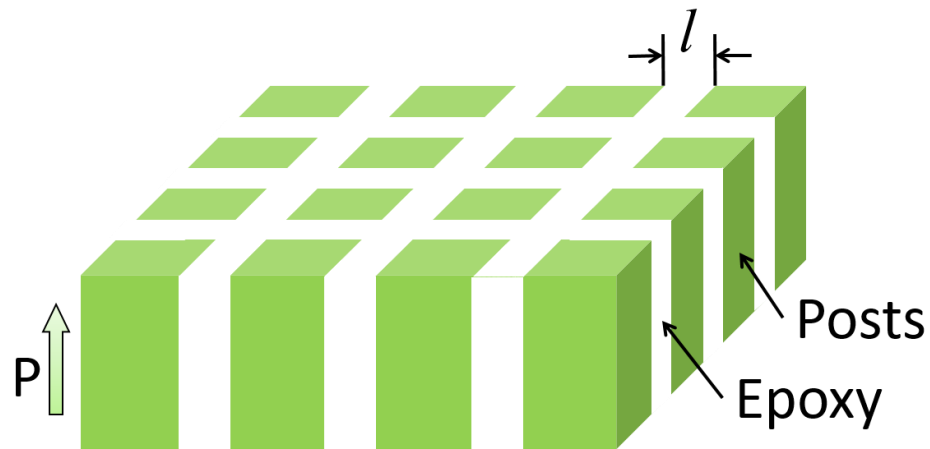


Figure 1.9 Structure of piezoelectric 1-3 composite consisting of active posts and passive filling materials (usually epoxy).

Piezoelectric materials for high power applications

High power ultrasound has been utilized in various medical applications [38]. The major application is high power therapy, delivering high acoustic power to malignant tissue inside body for non-invasive treatment. High power ultrasound transducers are used to generate high intensity focused ultrasound (HIFU) as a non-invasive therapy to cure diseases from tumors, cancers, thrombosis and so on [39]. Other medical applications include drug delivery [40, 41],

acoustic radiation force imaging (ARFI) [42], release of micro-pallet with cells [43], and so on. Besides medical applications, high power ultrasound transducers act as sonar projectors [44] and cleaners [45] as well. In all these applications, ultrasound functions as a power carrier with the purpose of energy delivery. High intensity ultrasound is generated by the transducers, with the companion of high electric field, heating of transducers due to loss, and so on. As a result, temperature properties, Q factor or loss, and coercive field are critical to make sure the transducers are not damaged. According to Table 1.2, materials (groups) satisfying such requirements are hard PZT and high power purposed relaxor-PT crystals.

In the hard PZT group, various acceptors doped PZTs have been developed for high power applications. Typical hard PZTs have Q factors of ~ 1000 and loss $< 1\%$, including PZT-2, PZT-8, PZT-4D, NCE40, NCE41, NCE80, Navy Type I, Navy Type III, and so on. Curie temperatures of these PZTs are $T_C > 250^\circ\text{C}$. Density and sound speed are about 7600 kg/m^3 and 4400 m/s so the characteristic acoustic impedance is about 33 MRayl . Coercive field of hard PZT are about $10 - 150 \text{ kV/cm}$ [46].

Various high power, high temperature, low loss, relaxor-PT based piezoelectric single crystals were developed due to their high piezoelectric performance. PIN-PMN-PT is one of the typical high power crystals with $T_C \sim 200 - 300^\circ\text{C}$, $T_r \sim 95 - 140^\circ\text{C}$, $Q > 1000$, loss $\sim 0.4\%$, coercive field $\sim 9 \text{ kV/cm}$ and a little compromise on the piezoelectric properties with $d_{33} \sim 900 \text{ pC/N}$ and $k_{33} \sim 0.89$ [47]. Mn-PMN-PZ-PT has a little higher piezoelectric performance than PIM-PMN-PT but slightly lower coercive field ($\sim 6.3 \text{ kV/cm}$). Doped PIN-

PMN-PT with Mn could further increase the T_C ($208^\circ C$) and T_{Trt} ($116^\circ C$) with sacrifice of d_{33} (267 pC/N) [48]. In general, relaxor-PT based piezoelectric crystals exhibit higher piezoelectric properties than PZT but are a little more vulnerable in high power conditions.

In transducer design, materials with superior piezoelectric properties are preferable as long as it is robust enough to work without being damaged in applications.

Piezoelectric materials for biomedical imaging applications

Transducers for biomedical imaging are usually excited by low power input and very low duty cycles with short pulses and low pulse repetition frequency (PRF). As a result, low power piezoelectric materials are used in medical imaging applications to benefit from high properties of the materials. Typical low power materials are soft PZT and relaxor-PT crystals, especially PMN-PT single crystals, referring to Table 1.2.

Donor doped soft PZT are developed for high piezoelectricity in the low power applications, including PZT-5A, PZT-5H, NCE55, NCE56, NCE59, Navy Type II, Navy Type VI, and so on. Dielectric loss of these materials are about $1.4 \sim 2.2\%$ and Curie temperature is about $180 - 310^\circ C$. Relatively high loss does not cause high temperature rise with the low voltage, short pulse input. Coercive field of these soft PZT is about $8 - 15 \text{ kV/cm}$ so that the relatively low voltage input does not damage the PZT materials.

Most of the relaxor-PT piezoelectric crystals are suitable for imaging because of their relatively high piezoelectric constants despite their low working temperature. PMN-PT ($\sim 33\%$ of PT) is one of highest performance piezoelectric crystals with $d_{33} \sim 2820 \text{ pC/N}$ and

$k_{33} \sim 0.94$ [13] although with almost the lowest working temperature $T_c \sim 155^\circ\text{C}$ and $T_{rt} \sim 65^\circ\text{C}$ [48]. Working temperatures of most relaxor-PT materials are generally lower than that of soft PZT, but are high enough in most cases, which are human body temperature (37°C) or room temperature (25°C).

Piezoelectric composite materials [18] are superior in biomedical imaging applications because of the high electromechanical coupling coefficients and relatively low acoustic impedances. In imaging applications, major concern of imaging ultrasound transducer is the bandwidth (pulse length) instead of the temperature. Ultrasound imaging basically utilizes pulse-echo method and time-of-flight of ultrasonic pulses reveals the spatial impedance change boundaries. At a given frequency, the fewer cycles there are in one pulse, the higher resolution the imaging is to differentiate targets next to one another. The echo signals are more or less like a single frequency wave convoluted with Hamming window and the fewer cycles there are, the wider the frequency spreads out around the center frequency. Unfortunately, traditional matching layer does not work well in the wide band impedance matching due to the significantly impedance mismatch between PZTs or relaxor-PTs ($Z \geq 32\text{MRayl}$). Bandwidth could be greatly increased if the impedance of the piezoelectric materials decreases. Combining piezoelectric material and polymers alternatively in a periodic manner, piezoelectric composite has much lower acoustic impedance (like 18 MRayl) than bulk PZTs or relaxor-PTs due to the decrease of both material density and sound speed. Besides the broadband, another merit of piezoelectric material is much higher electromechanical coupling factor ($\sim k_{33}$ versus k_t) if the composite material is fabricated in 1-3 connectivity (Figure 1.9).

Relaxor-PTs based 1-3 composite are more promising than soft PZT ones regarding to their superior k_{33} value (Table 1.2).

1.2 Ultrasonic wave

1.2.1 Theory and terminologies

Plane wave

Ultrasonic wave is basically the mechanical vibration with both time and spatial dependency. In most biomedical ultrasonic applications, the wave propagates in fluid or soft tissues so that shear wave diminishes very fast and only longitudinal wave propagates. One medical exception that involved solid medium and shear wave is the transcranial application [49] which is not the topic here. In this research, only longitudinal wave is discussed. Considering a one dimensional (1-D) wave (Figure 1.10), a slice of the medium in the propagation direction is shown at position x to $x+dx$. If the pressure is p at position x and $p + \frac{\partial p}{\partial x} dx$ at $x+dx$, then according to Hooke's Law,

$$\frac{\partial u}{\partial x} = \frac{p}{E}, \quad (1.20)$$

where u is the displacement of the particles in the medium and E is the bulk modulus of the material. According to Newton's Second Law,

$$\frac{\partial p}{\partial x} = \rho \frac{\partial^2 u}{\partial t^2}, \quad (1.21)$$

where ρ is the density of the medium material and t is time. Combination of (1.20) and (1.21) yields 1-D Helmholtz equation:

$$\frac{\partial^2 u}{\partial x^2} - \frac{1}{c^2} \frac{\partial^2 u}{\partial t^2} = 0 , \quad (1.22)$$

where c is the sound speed defined as

$$c^2 = \frac{E}{\rho} . \quad (1.23)$$

General solution of Equation (1.22) is

$$u(x,t) = Ae^{j(\omega t - kx)} + Be^{j(\omega t + kx)} , \quad (1.24)$$

where ω is the angular frequency and k is the wave number defined as $1/\lambda$ (λ is the wavelength). The general solution (1.24) is the plane wave propagation equation consisting both forward (x positive direction) wave and backward (x negative direction) wave with the amplitude of A and B for each wave. The Equation (1.24) is a general form for ultrasonic wave in a certain frequency. There might be more than one frequencies in the medium, in which case the waveform is the superposition of the waves at each frequency.

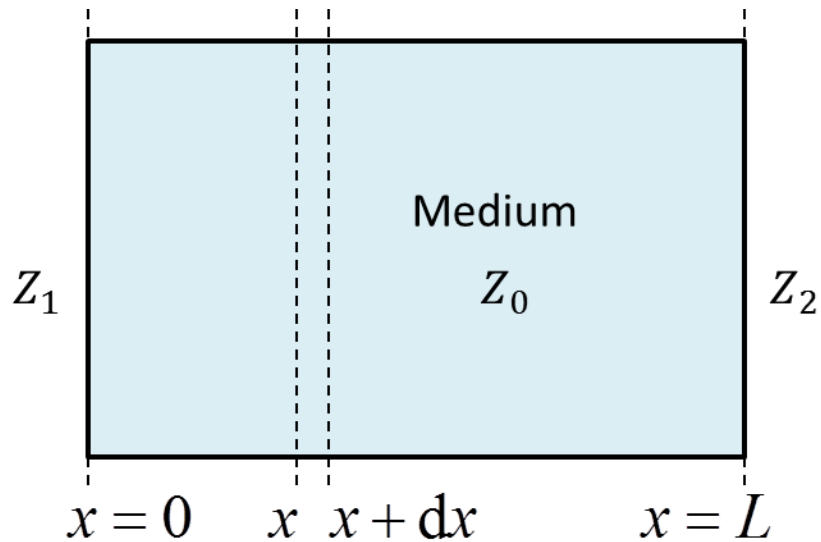


Figure 1.10 Schematic diagram of 1-D wave propagation.

Standing wave

If the boundaries are terminated at $x=0$ and $x=L$ (Figure 1.10), then the wave propagation is specialized according to the boundary conditions. If $Z_1 = Z_2 = Z_0$, indicating that the boundaries are perfectly matched at $x=0$ and $x=L$, then the wave propagates without any reflection, performing the same as the plane wave. On the contrary, if $Z_1 \neq Z_0$ and $Z_2 \neq Z_0$, then the specific medium vibrates as a standing wave. Starting from extreme conditions, the boundaries are considered as free or fixed, with boundary impedances Z_1 and Z_2 equaling to zero or infinity. There are 3 types of boundary conditions at these impedances: free-free, fixed-fixed and fixed-free. Three groups of vibration modes exist at these boundary conditions.

For a free-free boundary condition, both sides of the boundaries are free to move so that there is no stress at either boundary. According to (1.20),

$$\left. \frac{\partial u}{\partial x} \right|_{x=0} = 0 , \quad (1.25)$$

$$\left. \frac{\partial u}{\partial x} \right|_{x=L} = 0 . \quad (1.26)$$

Constrained with the boundary condition, the vibration modes are

$$u_n(x, t) = \tilde{A}_n \cos\left(\frac{n\pi x}{L}\right) e^{j\omega_n t} , (n = 1, 2, 3, \dots) , \quad (1.27)$$

where n donates the n th harmonic vibration mode. Equation (1.27) is the general form of the standing wave in the medium with free-free boundary conditions. The first 3 vibration modes in the group are shown in Figure 1.11. Furthermore, if the boundaries are symmetric ($Z_1 = Z_2$), then center surface ($x = L/2$) of the medium stays stationary if not specifically excited. In that case,

$$u|_{x=L/2} = 0 , \quad (1.28)$$

and the even order harmonics does not show up. Vibration modes in this case are

$$u_n(x, t) = \tilde{A}_n \cos\left(\frac{n\pi x}{L}\right) e^{j\omega_n t} , (n = 1, 3, 5, \dots) . \quad (1.29)$$

This group of vibration modes in Equation (1.29) is very close to active piezoelectric materials in piezoelectric transducers, which has low (not exactly free) impedance boundaries at both

sides and the two boundaries are almost symmetric. In most cases, the piezoelectric plates work at the fundamental frequency.

On the opposite, a fixed-fixed boundary condition indicates the medium is clamped at both boundaries, resulting in no displacement at the boundaries as

$$u|_{x=0} = 0 , \quad (1.30)$$

$$u|_{x=L} = 0 . \quad (1.31)$$

Vibration modes at this boundary condition are

$$u_n(x,t) = \tilde{A}_n \sin\left(\frac{n\pi x}{L}\right) e^{j\omega_n t}, (n = 1, 2, 3, \dots) . \quad (1.32)$$

The first 3 vibration modes are shown in Figure 1.11.

A third boundary condition is the fixed-free boundary condition, with one boundary of zero displacement and the other of zero stress. It is an equivalent issue either to be fixed at $x = 0$ or $x = L$. So in this topic, the fixed boundary is located at $x = 0$ while the free boundary is located at $x = L$. The boundaries are

$$u|_{x=0} = 0 , \quad (1.33)$$

$$\left. \frac{\partial u}{\partial x} \right|_{x=L} = 0 . \quad (1.34)$$

Vibration modes at this boundary conditions are

$$u_n(x,t) = \tilde{A}_n \sin\left(\frac{n\pi x}{2L}\right)e^{j\omega_n t}, (n = 1,3,5,\dots) . \quad (1.35)$$

The first 3 vibration modes are shown in Figure 1.11. The transducer matching layer (~ 4 – 7 MRayl) is close to the fundamental vibration mode with fixed-free boundary condition. The piezoelectric materials are the quasi-fixed boundary because of the high impedance of PZTs or relaxor-PTs (> 32 MRayl). The wave propagation medium out of the transducer, usually water or tissue, is the quasi-free boundary with impedance of 1.5 MRayl. The matching layer bridges the high impedance of piezoelectric materials with the low impedance medium outside of the transducer and enhanced the wave transmission efficiency at a certain frequency range.

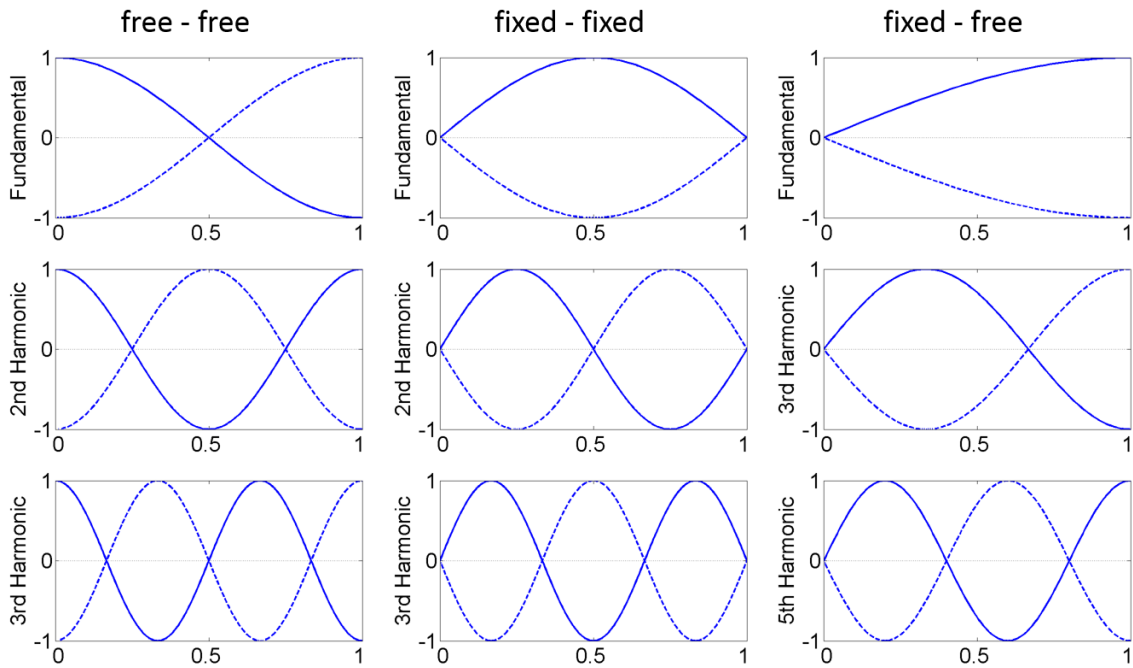


Figure 1.11 Standing wave vibration modes of the free-free, fixed-fixed, and fixed-free boundary conditions.

The theoretical calculations elucidate the basic vibration modes. In actual conditions, however, neither the active piezoelectric material nor the matching layer are exactly in these vibration modes. Matching layer makes the wave propagates towards the medium so that an impulse excitation diminishes with time.

Reflection and scattering

Acoustic energy is partially reflected and partially transmitted at mismatched boundaries (Figure 1.12 a). A matched boundary indicates the fact that the equivalent impedances across the boundary are in complex conjugate with each other ($Z_1 = Z_2^*$, with the star standing for complex conjugate operation). If Z_1 and Z_2 are real values, then $Z_1 = Z_2$. If the boundary is not matched ($Z_1 \neq Z_2^*$), the reflection coefficient R_p and transmission coefficient T_p are given as

$$R_p = \frac{Z_2 - Z_1^*}{Z_2 + Z_1^*}, \quad (1.36)$$

$$T_p = \frac{2Z_2}{Z_2 + Z_1^*}, \quad (1.37)$$

where the subscript $()_p$ stands for the pressure. Traditional ultrasound imaging technique was developed based on the reflection at impedance difference boundaries. An impulse is sent towards the target and the time-of-flight of the echo is used to calculate the distance of the target from the transducer, which is denominated as pulse-echo method. Amplitude of the echo ultrasound envelope reveals the boundary information including the boundary position,

impedance difference and so on. Consequently this 1-D imaging in time (axial space) domain is named as A-mode (amplitude-mode) imaging.

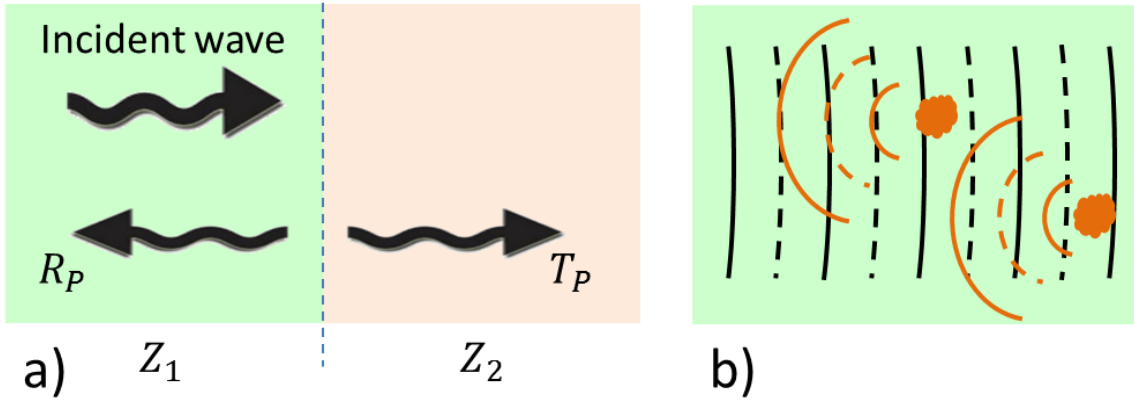


Figure 1.12 a) Reflection and transmission of ultrasonic wave at impedance boundaries. b) Scattering of acoustic wave at particles smaller than the wavelength.

If the reflecting boundary is not infinitely (or sufficiently) large plane but a small particle with similar or smaller dimension compared with the wavelength, then it acts as a scattering point source (Figure 1.12 b), with quasi-sphere wave given as

$$\frac{\partial^2 p}{\partial r^2} + \frac{2}{r} \frac{\partial p}{\partial r} = \frac{1}{c^2} \frac{\partial^2 p}{\partial t^2}, \quad (1.38)$$

$$p = \frac{A}{r} e^{j(\omega t - kr)}, \quad (1.39)$$

where A is the pressure amplitude at the surface of the scatter source and r is the distance to the center of the scatter source. Similar as reflection described in Equation (1.36), a higher

impedance difference between the medium and the particle results in higher scattering amplitude. A larger size of the scattering particle also leads to higher scattering amplitude. The scattering amplitude in the two-dimensional (2-D) space is usually displayed with brightness, and is thus named as B-mode (brightness-mode). B-mode imaging is the classic and the most widely used method in clinical ultrasound imaging.

Attenuation

Calculations above are based on an assumption that the loss is negligible in the wave propagation. As the acoustic wave propagates in a lossy medium, a portion of the mechanical energy is converted into thermal energy and dissipated. For the plane wave, the output pressure amplitude P is

$$P = P_0 e^{-\alpha x} \quad (1.40)$$

where P_0 is the initial input pressure amplitude and α is the frequency dependent attenuation coefficient usually given in dB/cm/MHz. At the back side (opposite side from the wave propagation field) of the transducers, a high lossy material is usually connected to the piezoelectric material so as to absorb the excessive acoustic wave and eliminate the reflection from back of the transducer. Such energy absorbing layer is named as backing layer.

Ultrasound characteristics

Power intensity I describes the acoustic power W per unit area A

$$I = \frac{W}{A} . \quad (1.41)$$

The power intensity is directly related to the acoustic pressure as

$$I = \frac{1}{T} \int_0^T \frac{p^2(t)}{Z} dt . \quad (1.42)$$

High acoustic power intensity could be achieved by focusing acoustic wave to a point by acoustic lens or phase array for a high power therapy or higher resolution imaging.

Mechanical index (MI) is another pressure related parameter to describe the pressure strength, which is defined as the peak negative pressure (PNP) in MPa, divided by the square root of frequency in MHz,

$$MI = \frac{PNP(MPa)}{\sqrt{f(MHz)}} . \quad (1.43)$$

The MI is highly related to bio-tissue nonlinearities because the tissue or microbubbles exhibit highly nonlinear vibrations at high rarefaction pressure. Detailed acoustic-tissue interaction will be discussed in the next sub-section.

In ultrasonic imaging, as mentioned above, the target distance is calculated from the time-of-flight of the echo. A short, distinct echo is ideal for a high resolution, high sensitivity imaging. The pulse length is routinely defined as the time interval out of which the amplitude of the wave envelope is lower than -20 dB. A short pulse length correlates to a wider band in frequency domain. There are many forms of definition of the bandwidth, directly in Hz, in octaves, and in fractional percentage. In ultrasound imaging routine, a fractional bandwidth at -6 dB is used to describe the pass band (half amplitude) divided by the center frequency. The

distinction of the echo from noise is denoted by the signal to noise ratio (SNR), which is also described in dB. A high transmission and high reception transducer tends to produce higher SNR images for a given target. The overall transmission and reception capability of a transducer is combined as the loop sensitivity, which is defined as the echo voltage amplitude versus the transmitting excitation voltage. In short, a broadband, high loop sensitivity transducer is ideal for ultrasonic the imaging.

1.2.2 Interaction between ultrasound and tissue medium

In either biomedical ultrasound imaging or therapy, interactions between ultrasound and tissue are utilized based on certain characteristics. One of the most widely used is the scattering of ultrasound by tissue in B-mode imaging stated above. In this research, more advanced interactions are involved including bio-heating, cavitation and nonlinear vibration of ultrasound agent (usually microbubbles).

Bio-heating

Bio-heating effect makes use of the attenuation as ultrasound propagates in tissue. According to Equation (1.40) to (1.42), the attenuation induced power loss in unit area at position x to position $x + \Delta x$ is

$$\Delta I = I_0 e^{-2\alpha x} (1 - e^{-2\alpha \Delta x}). \quad (1.44)$$

where I_0 is the initial power intensity at reference position $x = 0$. The following conclusions are obtained from Equation (1.44):

- power loss at position x is proportional to the acoustic intensity;
- deeper (larger x) position has lower power loss;
- the intensity vanishes faster with larger attenuation α .

In most cases, characteristics of 1-dimensional plane wave are not ideal for biomedical applications. Typical applications of bio-heating mechanism are ultrasound treatment of tumors, cancers or benign diseases [50], generating heat from ultrasound wave to kill the tumor or cancer cells. Focused ultrasound (FUS) was implemented to solve the problem. Large aperture ultrasound transducer was designed to generate moderate intensity ultrasound at the surface of the transducer and high intensity ultrasound was achieved at the focal point by constructive interference. High intensity at the focal point induced high power loss, the energy of which is transformed into heat for treatment.

Attenuation induced bio-heating is not an efficient mechanism to convert ultrasonic energy into heat because a large portion of the energy continues propagating into deeper tissue. At high intensity with high MI, cavitation effect is induced, which could greatly enhance the heat generation efficiency [51].

Cavitation

Cavitation is the interaction between ultrasound and microbubbles, including bubble grow, vibration (expansion and compression in size), and implosion. According to the microbubble responses, cavitation is classified as two types: inertial cavitation and stable cavitation.

The inertial cavitation happens if the absolute value of acoustic negative pressure is higher than a threshold (high acoustic intensity), when the microbubbles grow in size and then collapse rapidly. The growth of microbubbles generally requires a surface as nuclei, which could be impurities in the liquid, or small undissolved microbubbles within the liquid. Such low pressure microbubbles implode violently when subjected to high pressure ambience, and high temperature (thousands of degrees) and high pressure (kilobars) are generated, which induce a variety of chemical reactions [52]. The extreme condition and shock wave generated by inertial cavitation are destructive and harmful to tissue [53, 54]. Experiment showed that inertial cavitation significantly increased the heating efficiency by re-radiation of the incident ultrasound wave as broadband noise emission, which plays a major role in HIFU treatment [51].

Stable cavitation refers to the microbubble vibration, i.e. alternation of microbubble size due to the external pressure applied on it. It happens if the external pressure (either positive or negative) is not high enough to generate or destroy existing microbubbles. Because microbubbles are more resistant to compression than to expansion, its vibration is highly nonlinear and a variety of frequencies (sub-harmonics, harmonics and super-harmonics, i.e. higher than the third order harmonics) are generated in the backscattering signal [55]. Detection and visualization of signals at these frequencies are sub-harmonic, harmonic or super-harmonic imaging. These techniques eliminated the strong fundamental frequency scattering from normal tissue and visualize the microbubble-enriched regions only, such as microbubble flooded blood vessels. High contrast to tissue ratio was achieved by imaging with

the nonlinearities of microbubbles [56-58]. In the applications with stable cavitation only, acoustic intensity is not high enough to grow microbubbles from nuclei. Existing microbubbles are needed to be added to the system.

The two types of cavitation are classified to describe different microbubble responses, but are not isolated in actual conditions. For example, both types exist in HIFU treatment after microbubbles are generated by inertial cavitation. Ultrasonic cavitation has been a powerful tool for both treatment and diagnosis.

1.3 Medical applications of ultrasound

1.3.1 High intensity focused ultrasound

High intensity focused ultrasound (HIFU) is a non-invasive treatment that delivers energy of acoustic wave to target, generating heat to damage diseased cells selectively at the focal point of the acoustic beam [59]. It can be used in many therapeutic applications such as drug delivery [38], control of bleeding [60], tumor or cancer ablation in prostate, liver, breast, kidney, sarcoma, uterine fibroids, and so on [61]. This therapeutic method was non-invasive, safe, repeatable [62], with demonstrated efficacy, and low-associated morbidity [63]. Major limitations of HIFU therapy were the long treatment time [62], which may last 1 hour for tumor of 3 mm diameter and more than 6 hour for tumors of 10 mm diameter [61] because each focal zone is a small volume with typically ellipsoidal in shape of ~ 1.5 cm in length and 1.5 mm in width [64]. A high efficiency HIFU ablation method would reduce the treatment time with limited power deposition. Another limitation of HIFU treatment is that the lesion position

needs to be in the acoustic window, otherwise, it is hard to heat the target without too much heating on the obstacles. HIFU transducer arrays [65] and time reversal beam focusing method [66] were developed to expand the application of HIFU to targets beneath ribs and skulls. Technological development suggested that HIFU is likely to play an significant role for non-invasive therapy in future [67, 68].

As the treatment is beneath body surface (usually 2 – 9 cm [69]) without incision, real time monitor of the treatment is necessary. Magnetic resonance imaging (MRI) was usually used for the monitoring because it exhibits excellent detecting ability on the temperature inside body [70, 71] although the resolution and frame rate were not very high [72]. Ultrasound imaging was also applied as visualization of the heating effect including B-mode imaging [73], M-mode imaging [74], and ultrasound computed tomography [75]

1.3.2 Imaging ultrasound

Ultrasonic biomedical imaging covers enormous types of imaging techniques including traditional B-mode imaging [76], Doppler imaging [77], acoustic radiation force impulse (ARFI) imaging [42], contrast enhanced imaging [78], photoacoustic imaging [79], acousto-optic imaging [80], harmonic imaging [81], and so on. Among these imaging techniques, ARFI is a special case that requires high intensity (> 2 MPa), quasi-continuous wave (300 – 1200 cycles) to generate radiation force for the imaging. Tissue harmonic imaging and contrast harmonic imaging, either for intravascular environment or not, transmit moderate pressure (~ 1 MPa) and short pulse (1 – 2 cycles) ultrasound wave to excite the non-linearity of tissue or bubble and detect the harmonic signal, so low power piezoelectric materials (soft PZT or PMN-

PT) are good enough for this application. Doppler imaging uses several cycles (~ 10) at low acoustic intensity and detects the frequency shift of the received signal to calculate the movement of the target according to Doppler effect. Other imaging techniques utilizes low intensity, short pulses (~ 1 cycle), which are typically low power requirement of the transducers. In short, biomedical imaging applications (except ARFI) uses ultrasound to deliver information instead of energy so that generally low power ultrasound is needed, and hence high performance piezoelectric materials are ideal despite their low working temperature and high loss.

Based on the sound wave delivering method, the ultrasound applications can be classified as transcutaneous and percutaneous. The transcutaneous ultrasound delivering method is to generated ultrasonic wave outside of the body and deliver the wave through the skin [82]. Advantage of this imaging method was the non-invasive feature and no much limitation on the dimension of the transducers, so that it was the most well developed and widely used for real-time three-dimensional imaging [76]. This transcutaneous imaging mechanism is mainly limited by the penetration depth in applications which high frequency ultrasound was needed for high resolution imaging. In applications such as blood vessel wall imaging and vasa vasorum angiography, percutaneous ultrasound method was usually used, which delivered ultrasonic wave by an intravascular ultrasound (IVUS) transducer inside a catheter [83]. Visualization of the vessel structure could be reconstructed slice by slice by rotating the transducer and pulling it back through the catheter simultaneously [84]. Conventional IVUS imaging was very effective in detecting the coronary vessel wall structures and plaque

morphologies [85], but was not optimal for vasa vasorum imaging [86], details of which would be discussed in Chapter 3.

1.4 Microwave

In the multi-layer ultrasound transducer design, it is complicated to analyze the interactions among the layers and it is hard to find out an intuitive guideline on how to choose the layer parameters, such as thickness, impedance and so on. On the other hand, the electromagnetic wave equations are mathematically identical with acoustic wave, and microwave theory is well-developed on the calculation of multiple elements cascade. Hence, microwave theory can be introduced as a guidance of the multi-layer transducer design.

Microwave theory [87] processes the electromagnetic field in a distributed wave manner instead of lumped elements. Energy is stored and transmitted as a distributed field. Electric energy exists as the electric field in the dielectric material (including vacuum) between electrodes, and magnetic energy exists as the magnetic field induced by alternating current in the electrode and electric displacement in the dielectric materials. Characteristics of the distributed field are highly dependent on the frequency, dimension, boundary conditions, and so on, which are studied as the transmission line theory.

1.4.1 Transmission line

Concept

Transmission line is a section of cable that stores and transmits electromagnetic wave as a distributed field in the dielectric materials. Transmission line effect shows up because the wave

speed is finite and the electromagnetic field takes time to transmit from one end to the other. If the length of the line is significantly shorter than the wavelength, then the variation of electromagnetic field in the electrode and dielectric material is trivial. In that case, the transmission line could be considered as simply a conductor that connects the elements at the two ends. However, if the transmission line is longer or comparable with the wavelength, then the transmission line acts as a waveguide and the waveform in the transmission line is determined by the impedance conditions at the boundaries.

Characteristics

Transmission line is a typical distributed component with varying electromagnetic field characteristics along the line. Both voltage (electric field) and current (change of magnetic field) are propagating in a wave form with sinusoidal variation in both space and time domains. Equivalent (input or output) impedance of the line, defined as $Z = V / I$, also varies along the line in both amplitude and phase in a sinusoidal manner. The schematic diagram of the transmission line is shown in Figure 1.13.

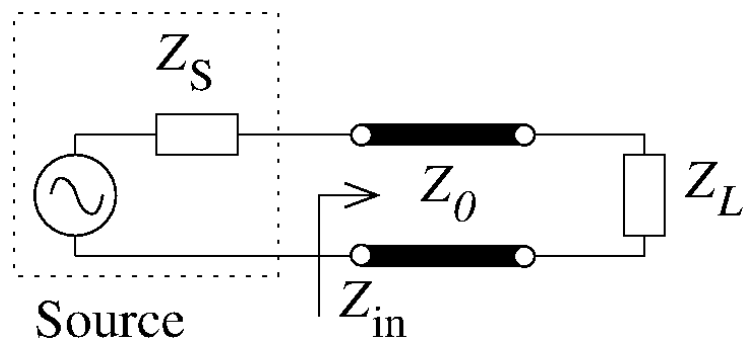


Figure 1.13 Schematic diagram of the transmission line circuit.

The input impedance Z_{in} at the port of the line is

$$Z_{in} = Z_0 \frac{Z_L + Z_0 \tanh \gamma l}{Z_0 + Z_L \tanh \gamma l}, \quad (1.45)$$

where Z_0 is the characteristic impedance of the line, Z_L is the impedance of the load and l is the length of the line. The propagation constant γ is defined as

$$\gamma = \alpha + j\beta \quad (1.46)$$

where α is the attenuation coefficient and β is the phase constant. In many cases, low loss transmission lines are used. If the attenuation α is negligible, then the input impedance reduces to

$$Z_{in} = Z_0 \frac{Z_L + jZ_0 \tan \beta l}{Z_0 + jZ_L \tan \beta l}. \quad (1.47)$$

If the Thevenin's equivalent impedance of the source at the input port of the line is Z_S , then the reflection coefficient at the port is

$$\Gamma = \frac{Z_{in} - Z_S^*}{Z_{in} + Z_S^*}, \quad (1.48)$$

where Z_S^* is the complex conjugate of the source impedance Z_S . If the line is lossless, there is no energy dissipation on the line. As a result, the transmission coefficient T is calculated from the principle of energy conservation

$$T = \sqrt{1 - |\Gamma|^2}. \quad (1.49)$$

Multiple functions can be achieved by using the transmission lines. First, most transmission lines are low loss because the conductance of dielectric material is low and the resistance of electrode is low as well if the frequency is not extremely high. Low energy dissipation happens on the line. Second, impedance at the port can be tuned by adjusting the characteristic impedance and the length of the line, so that the reflection coefficient can be tuned to be matched or mismatched according to specific applications. Third, according to Equation (1.47), if the impedance is matched at the load ($Z_L = Z_0$), then the input impedance Z_{in} is always equal to Z_0 no matter how long the line is. The matched ports can be extended by a long matched transmission line. Because of their outstanding characteristics, transmission lines are widely used in microwave devices as the impedance matching network, and as energy transmission connection from microwave source to amplifier, from amplifier to transmitting antenna, from receiving antenna to signal processing unit, and so on.

Cascade properties

Multiple sections of transmission lines could be connected as a chain in cascade, with the rear sections acting as the load while the precedent acting as the source. Input impedance could be calculated section by section from the very end of the chain, and the reflection coefficient is calculated from the input and output impedance at the adjacent ports. Such calculation could be simplified as matrix multiplication of ABCD parameters. The ABCD parameters are defined as

$$\begin{bmatrix} V_a \\ I_a \end{bmatrix} = \begin{bmatrix} A & B \\ C & D \end{bmatrix} \begin{bmatrix} V_b \\ I_b \end{bmatrix}, \quad (1.50)$$

where V and I are the voltage and current, respectively, at the ports a and b denoted by subscripts $()_a$ and $()_b$. If N components are cascaded in the chain, then the equivalent ABCD parameters of the chain is

$$\begin{bmatrix} A & B \\ C & D \end{bmatrix} = \begin{bmatrix} A_1 & B_1 \\ C_1 & D_1 \end{bmatrix} \begin{bmatrix} A_2 & B_2 \\ C_2 & D_2 \end{bmatrix} \cdots \begin{bmatrix} A_N & B_N \\ C_N & D_N \end{bmatrix}. \quad (1.51)$$

For a section of transmission line, the ABCD parameters are

$$\begin{bmatrix} A & B \\ C & D \end{bmatrix} = \begin{bmatrix} \cosh \gamma l & Z_0 \sinh \gamma l \\ Y_0 \sinh \gamma l & \cosh \gamma l \end{bmatrix}, \quad (1.52)$$

where $Y_0 = 1/Z_0$ and other parameters are defined above. The input impedance of a cascade chain could be calculated directly from the equivalent ABCD parameters.

1.4.2 Smith chart

The reflection coefficient can be plotted in a polar plot that has a radius of one (Figure 1.14). Modulus of the vector in the polar plot elucidate the amplitude of the reflection coefficient and the angle denote the phase. The center point has a perfect matching with no reflection because its magnitude is 0 (green dot in Figure 1.14 a). At the unit circle with magnitude of 1, there is 100% reflection and no transmission (red phasor in Figure 1.14 a). Plotting a reflection coefficient on the polar plot enables convenient interpretation of the properties of a reflection.

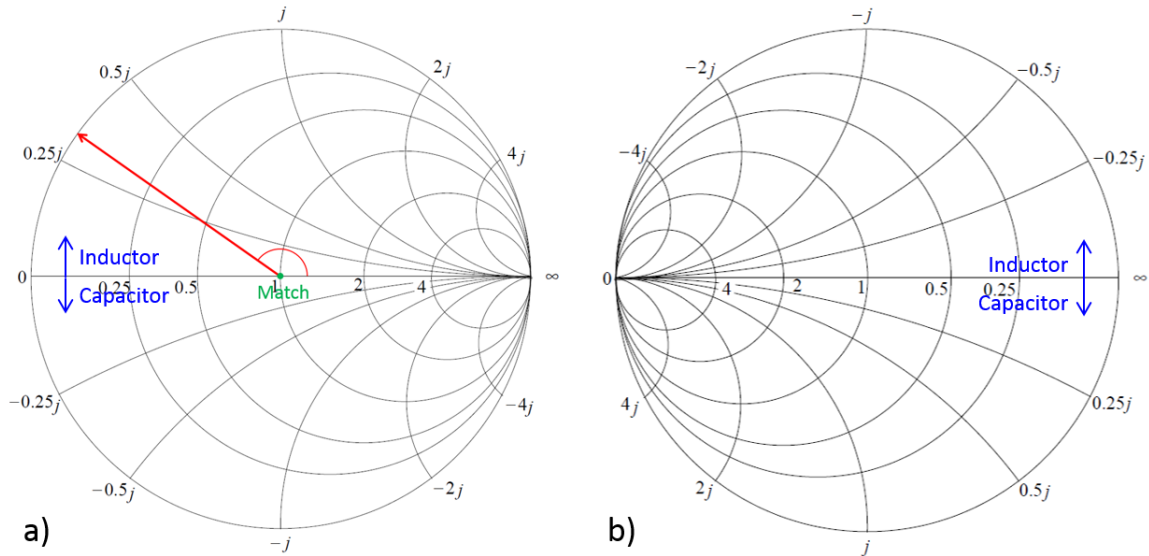


Figure 1.14 Example of a) an impedance Smith chart and b) an admittance Smith chart.

Normalized impedance could be added in the polar plot, which is denominated as Smith chart (Figure 1.14 a). Real values of the impedance (resistance) are labeled on the horizontal axis of the chart while imaginary values (reactance) are labeled on the circles. Constant resistance lines are circles in the Smith chart with values marked on the horizontal axis. Constant reactance lines in the chart are the curves marked with imaginary numbers. The complex values inside the Smith chart are impedances with both resistance and reactance. Normalized admittance could also be added to the Smith chart (Figure 1.14 b), which is used for a shunt elements network.

1.4.3 Impedance matching

A matched network is the network without reflection. If the network is lossless, the maximum power is delivered to the load. In most cases, maximum power delivery is desirable to minimize the power consumption for the same power output, to reduce heat dissipation in the system, and to increase the system stability due to low (if any) reflection from the load.

A matched impedance indicates the fact that the impedances of the source and load (each might include a series of matching networks) are complex conjugate ($Z_S = Z_L^*$). Typically the output Thevenin's equivalent impedance of the source is 50Ω , and the load is matched to 50Ω by the matching network. In order to make maximum power delivery, the network is usually matched with lossless (ideal case) elements such as capacitor, inductor and transmission lines.

The impedance Smith chart is used for serial connected elements in the matching network. A serial connected capacitor decreases the imaginary value of the impedance along the constant resistance curve because there is no change on the real value of the impedance. A serial connected inductor increases the imaginary value of the impedance along the constant curve as well. A transmission line shifts the impedance around a circle (arrows in Figure 1.15 a). The admittance Smith chart is used for shunt connected elements in the matching network. An inductor decreases the imaginary value of the admittance while a capacitor increases the imaginary value of the admittance (blue arrows in Figure 1.14). In short, an inductor shifts the curve upwards while a capacitor shift it downwards for both serial and shunt connections, but

on different curve, constant resistance for shunt connection and constant conductance for shunt connection.

For a lossless transmission line, the impedance or admittance is shifted following a circle but not along the constant resistance or constant conductance (Figure 1.15). If the impedances are normalized to the characteristic impedance, then the center of the circle is at the center of the Smith chart. Otherwise, the center of the circle depends both on the normalized impedance and the impedance of the load. The shifting direction is clockwise with a period of $\beta l = \lambda / 2$. In other words, the input impedance keeps constant after inserting a section of transmission line with half wavelength. Such periodicity could also be easily predicted from Equation (1.47).

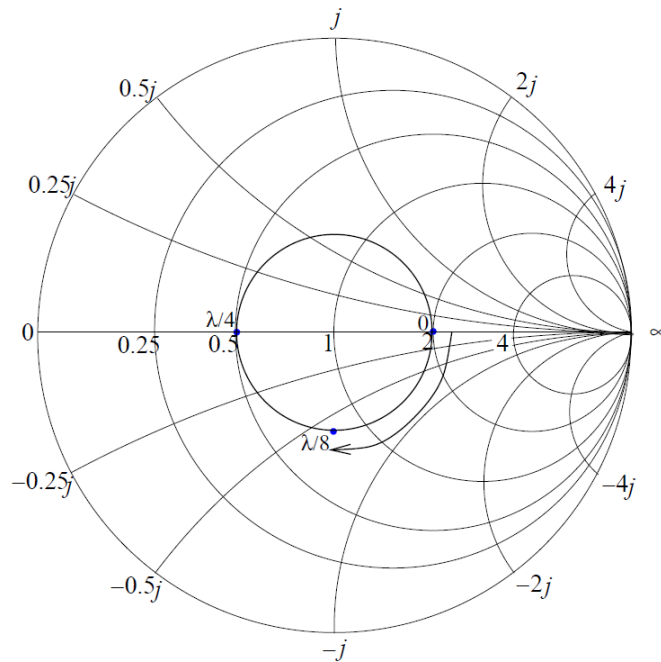


Figure 1.15 Locus of a transmission line in the Smith chart.

Quarter wavelength impedance inverter is often used in impedance matching network. With a quarter wavelength long transmission line, the Equation (1.47) reduces to

$$Z_{in} = \frac{Z_0^2}{Z_L} . \quad (1.53)$$

The input impedance at the quarter wavelength transmission line is reversely proportional to the load impedance. If the Smith chart is normalized to the characteristic impedance of the transmission line ($Z_0 = 1$), then the input impedance is directly the reciprocal value of the load impedance (Locus in Figure 1.15 from length 0 to $\lambda / 4$). One more feature of the inverter is that if Z_L is real, then Z_{in} is real as well.

1.5 Dissertation structure

In this dissertation, dual frequency ultrasound transducers will be described for both therapeutic applications and for diagnosis applications, together with an acoustic filter design used in the transducers for the wave propagation control. The first chapter introduced the background information needed to design the dual frequency transducers. In Chapter 2, a 1.5 MHz / 3 MHz dual frequency ultrasound transducer was designed, prototyped and tested for enhanced high intensity focused ultrasound (HIFU) tissue ablation. In Chapter 3, some intravascular ultrasound dual frequency transducers for contrast enhanced super-harmonic imaging were investigated, including their design, fabrication, characterization, *in vitro* imaging test and parameters optimization. In these transducers, specially designed anti-matching layer(s) is needed to suppress the aliasing echo. Detailed design of the anti-matching

layer(s) was discussed in Chapter 4. Furthermore, the anti-matching layer not only suppressed the high frequency wave, but also enhanced the low frequency wave transmission. Finally, conclusions were given in Chapter 5 on the dual frequency transducers designed for medical applications and the design principles of multi-layer transducers.

Chapter 2.

Dual Frequency High Intensity Focused Ultrasound Transducer

2.1 Background

The first experiment of HIFU was proposed in 1942, by ablating tissue inside with little harm on the surface[7]. Since then, HIFU has become an important tool for noninvasive therapy [67, 69, 70, 88, 89]. In general, HIFU therapy was induced by hyperthermia effect, which was used to clinically manage a broad range of cancer and benign disease [50], including solid tumors [61, 90], breast tumors [75], blood-brain barrier [91, 92] and prostate cancer [63].

In order to increase the ablation efficiency of HIFU treatment, multi-frequency ultrasound has been studied in recent years by a few groups [93-97]. As an example, the dual frequency tissue ablation experiments were carried out by simultaneously irradiating porcine liver regions of interest with confocal ultrasound transducers at 1.563 MHz and 1.573 MHz [93], where the frequency difference is 10 kHz. It was found that dual frequency HIFU induced larger lesions than conventional single-frequency HIFU under the same power density, which was likely a result of the enhanced cavitation.

Cavitation is a controversial effect in HIFU ablation, which is classified as stable and inertial cavitation. Of them inertial cavitation bubbles generate broadband noise, which could re-radiate the incident sound and thus enhance heat generation, the scheme of which makes major contributes to heating enhancement [51]. Research shows that cavitation-induced

heating could generate a few times greater heat deposition than that induced by ultrasound only, largely due to the enhancement of cavitation yield from multi-frequency ultrasound [94-99]. It was also found that a three-beam configuration could further increase cavitation yield (28 kHz, 1 MHz and 1.66 MHz combination) [100]. In quantitative comparison of single and multi-frequency HIFU ablation, temperature rise showed that the ablation efficiency of multi-frequency ultrasound is higher than that of single frequency ultrasound [101]. Treatment with dual frequency exposure showed better effect on elongating life of tumor-bearing-mice [102]. Besides enhanced heating, cavitation also helps monitoring the location of the heat deposition [51].

Multi-frequency ultrasound takes the advantage of cavitation, but, in many cases, increases the complexity and cost of the HIFU system. For example, focal zone of the multiple transducers must overlap one another so as to generate enhanced inertial cavitation. Multiple transducers must be driven by multiple amplifiers and multiple function generators, which is prohibitive in implementing a HIFU array system with a large number of elements [101, 103]. Initial effort of exciting a HIFU transducer with harmonic signals was explored to create high efficiency at low complexity [96, 104]. However, resonance of higher harmonics was weak compared to the base frequency resonance.

In this study, a single aperture, dual frequency HIFU transducer was designed and fabricated with identical focal point for both working frequencies. First, performance of multilayer resonator design was analyzed, and design parameters were optimized with KLM (Krimholtz, Leedom, Mattaei) modeling [105] and field II program[106]. Then, the two-layer, dual

frequency transducer was fabricated and characterized. At last, tissue ablation test was performed using the prototyped transducer and the same driving electronic equipment at single frequency mode and dual frequency mode, respectively, for ablation efficiency comparison.

2.2 Theoretical analysis

2.2.1 Single layer vibration

As is shown in Section 1.2.1, the vibration mode with a free-free boundary condition is defined as Equation (1.29), which is the general case for a single layer piezoelectric transducer (Figure 2.1 a). With a thickness of L , vibration modes that matches the boundary conditions are

$$\lambda_n = \frac{2L}{2n+1}, (n = 1, 3, 5, \dots) , \quad (2.1)$$

and the resonant frequencies are

$$f_n = \frac{nc}{2L}, (n = 1, 3, 5, \dots) . \quad (2.2)$$

The first 3 resonant frequencies are shown in Figure 2.2.

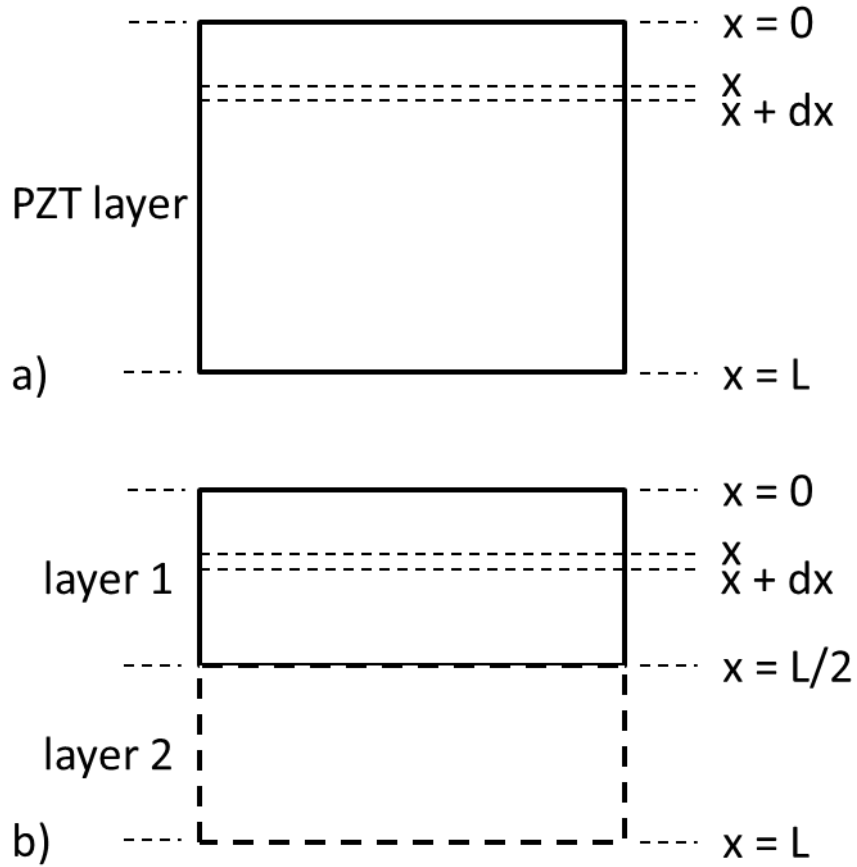


Figure 2.1 Configuration of a) single layer and b) double layer transducers.

With matching layer and backing layer added to the transducer, the front and back surfaces are not necessarily free to move, resulting in a frequency shift in each mode. Transmission line analysis provides a better approximation [107]. However, the ideal case (free-free vibration mode) provides a basic guideline on the transducer design.

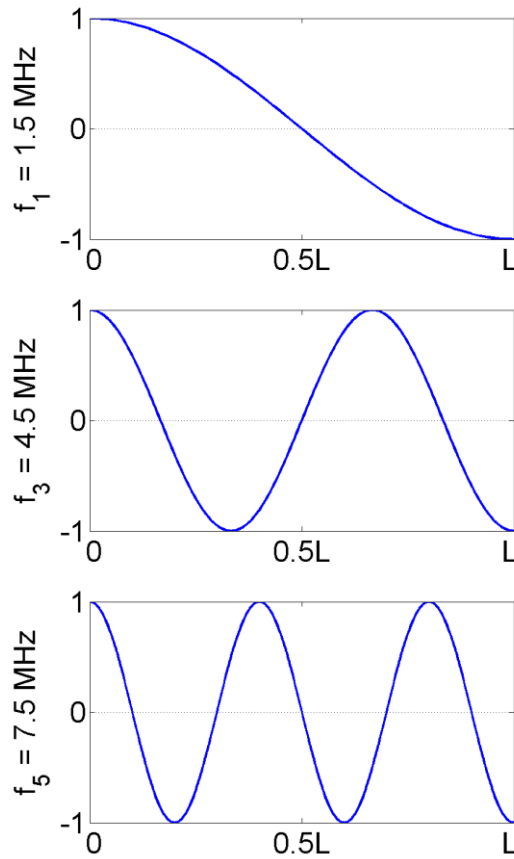


Figure 2.2 Vibration modes of a single layer transducer. Values on Y-axis indicate the relative displacement in each mode. L is the thickness of the active (piezo) material.

For a homogenous piezoelectric plate, the amplitude of higher order of harmonics, such as 3rd and 5th harmonic, are pretty low (< -12 dB for this transducer) for a HIFU transducer because of the narrow bandwidth in most cases. And relative strength of each harmonic is hardly tunable. As a result, transducers with single homogenous piezoelectric layer were not widely used to generate dual or multiple frequencies HIFU ultrasound. The dominant resonance at its fundamental frequency is

$$f_1 = \frac{c}{\lambda} = \frac{c}{2L}, \quad (2.3)$$

the resonance of which is generally used as a single frequency transducer.

2.2.2 Double layer resonator

To design a single aperture dual frequency transducer, the overall piezoelectric material is divided into two identical layers as labeled in Figure 2.1 b). With this configuration, only layer 1 of the transducer is excited while layer 2 of the transducer acts as a backing layer. Because the thickness is halved, twice of the initial frequency is generated. Instead of staying still, the plane at the center of the transducer vibrates, introducing vibration modes of $\omega_n' = \frac{2n\pi c}{L}$, where values with prime indicate the double layer transducer. As is shown in Figure 2.3, the frequencies of each order of harmonic introduced by double layers are twice as the single layer transducer ($\omega_n' = 2\omega_n$). At base frequency with $n = 1$, both ω_n and ω_n' meet the requirements of the boundary condition. As a result, dual frequency ultrasound could be generated with this single aperture transducer.

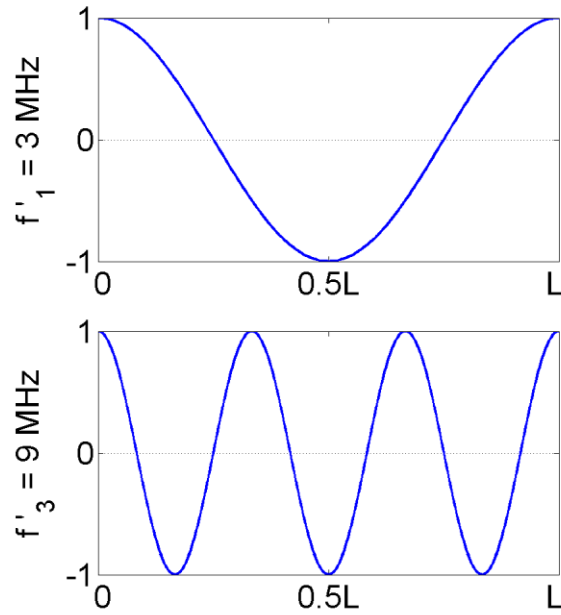


Figure 2.3 Additional vibration modes of a double layer transducer. Values on Y-axis indicate the relative displacement in each mode. L is the total thickness of 2-layer piezo material.

Compared to a single layer transducer with the same overall thickness, a dual layer transducer introduces another group of vibration modes (ω_n'), which is twice the frequency (ω_n) of the single layer transducer. Such new group of vibration modes appear in dual layer transducer because of break of symmetry by one-layer excitation, which overcomes the boundary condition limited by Equation (1.28). With proper design, i.e. thickness of active layers and matching layer, base frequencies at the two groups could be adjusted to be close in amplitude. Besides, amplitude of the two base frequencies is still much larger (> 12 dB) than that of higher order harmonics.

2.3 Dual frequency transducer

2.3.1 Transducer design

Based on the analysis, a dual-layer, dual frequency, single-aperture transducer was designed as shown in Figure 2.4. Two layers of PZT-2 were mechanically bonded together and electrically controlled separately so that the transducer could vibrate at different modes. Mechanically, two PZT-2 layers bonded in series. If the front layer vibrates, the back layer acts as a backing layer; in the other case that the back layer vibrates, the front layer acts as a matching layer. The thickness of each PZT-2 layer is half wavelength of 3 MHz ultrasound wave, so that the resonant frequency for each PZT-2 layer is 3 MHz. Bonded together, the two PZT-2 layers could vibrate as one layer with twice thickness and vibrate at the same mode, yielding 1.5 MHz ultrasound. In this case, the dual frequency transducer could work at 3 MHz mode or 1.5 MHz mode. The polarization of the two PZT-2 layers is opposite. In electrical view, electrodes between the two layers are shorted as fire signal. The front electrode of the front layer and the back electrode of the back layer could be grounded together, or one grounded while the other left non-connected. Thus, choices are available by exciting one layer or both layers. A summary of the vibration modes is listed in Table 2.1.

Table 2.1 Summary of vibration modes of the transducer.

	front layer excitation	both layer excitation
electrical view	1 layer excited	2 layers in parallel connection
mechanical view	active layer with backing	homogeneous active layer
resonant mode(s)	3 MHz & 1.5 MHz	1.5 MHz

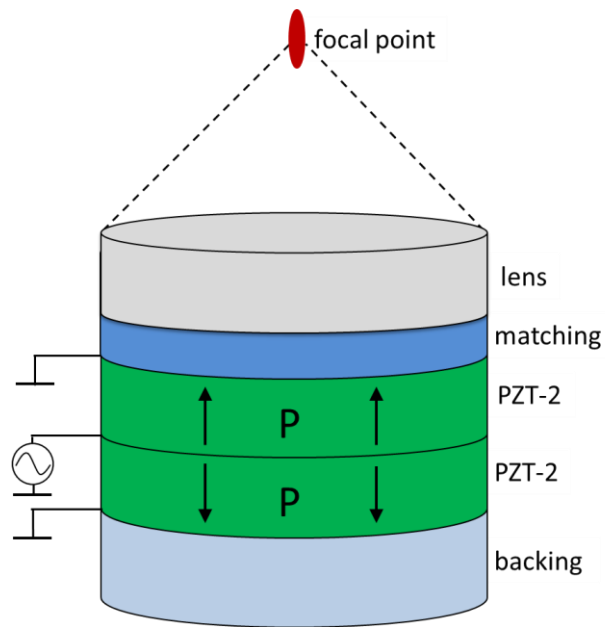


Figure 2.4 Configuration of the dual frequency transducer. Arrows on the transducer indicate the polarization direction.

2.3.2 KLM modeling

The goal of this transducer design was to obtain dual frequency ultrasound with similar acoustic pressures from a single aperture. KLM model was used to estimate the performance of the transducer. In particular, electrical impedance spectrum of single layer and double layer resonators were modeled considering different matching and backing materials.

In the modeling, 1.5 MHz and 3 MHz configurations were simulated separately. For the modeling of the 1.5 MHz single frequency configuration, the two PZT-2 layers were considered as one thick layer. With such assumption, the transmitting electrical impedance should be a quarter of the simulated value because of the mechanical serial, electrical parallel configuration. For the 3 MHz configuration, the front PZT-2 layer was used as the active layer and the back one was considered as the backing layer.

Since there are two frequency modes in the transducer, the quarter wavelength matching layer could match only one frequency. Attenuation is higher in materials at higher frequency, so the matching layer was set to match the 3 MHz transducer to balance the power output of the two frequencies. Based on KLM simulation, thickness of the matching layer was set to be 0.16λ for 3 MHz ultrasound.

2.3.3 Acoustic field simulation

In HIFU applications, targets beneath the skin are exposed to high pressure while keeping the surface of the skin little influenced. The key is to keep the acoustic pressure at skin within a low level and to focus ultrasound at target to achieve a pressure high enough to induce

hyperthermia effect, thus damaging the tumor or cancer cells. As a result, an estimation of the beam profile is desirable.

Field II [106], a MATLAB based toolkit, was used to perform the field simulation. The surface of the transducer is concave because lens was added to the transducer. The focal length of the transducer is 15mm. Concave model was used in the simulation with an aperture radius of 12.7 mm and focal radius of 15 mm. Continuous wave was supplied to the transducer with an effective voltage of 100 V, corresponding to 283 Vpp. Based on KLM modeling, pressure generated by the transducer was 2.85 kPa/V and 1.81 kPa/V for 1.5 MHz and 3 MHz ultrasound respectively. Because the transducer is axial symmetric, emitted field was simulated with Field II on the y-z plane, with z-axis being the axial direction of the transducer. The boundary was set as -15 mm to 15 mm in y direction and 0mm to 40 mm in z direction to well cover the area of interest.

2.3.4 Fabrication

PZT-2, a piezoelectric ceramic material from Shanghai Ceramic Institute (Shanghai, P. R. China), was used as the active material in the transducer. PZT-2 plates with resonant frequency of 3 MHz were prepared, with the thickness of 0.735 mm and diameter of 25.4 mm. More parameters of the materials on the transducer are listed in Table 2.2.

Table 2.2 Parameters of the materials on the transducer

Layers	back support	active	matching
Material	hard air	PZT-2	graphite
Shape of the transducer	round	round	round
Diameter (mm)	25.4	25.4	25.4
Thickness (mm)	NA	0.735	0.172
Sound speed (m/s)	NA	4430	3230
Impedance (MRayl)	0.5	34.1	6.0
Relative dielectric constant	NA	560	NA
Coupling coefficient k_t	NA	0.52	NA
Mechanical quality factor	NA	1000	NA
Dielectric loss	NA	0.002	NA

Two pieces of such PZT-2 ceramic plates were bonded together, forming the dual frequency transducer. The two PZT ceramics were bonded by epoxy with pressure applied on the ceramics. It was verified that the thickness of the bonding layer was less than 5 μm . Compared with the thickness of the PZT layers (735 μm), such bonding layer was considered as negligible for the vibration. In the wave forwarding direction, a block of graphite, 7.825 mm in thickness, was bonded to the surface of the PZT-2 ceramic. The graphite block was then machined to

form a 15 mm radius curvature and 7 mm in depth of the curvature. In the backing direction, very lossy microbubble filled epoxy, known as hard air, with an acoustic impedance of 0.5 MRayl was bonded to the PZT-2 back surface to support the piezoelectric layers. Aluminum was used to house the transducer.

Outside surfaces of both plates could be connected to ground while the center electrode between the two plates was connected to hot wire as is shown in Figure 2.4. In this case, the two PZT-2 plates could either be fired together or individually via two BNC cables.

2.3.5 Transducer characterization

Pulse-echo experiment was performed to verify the transducer performance. The transducer was positioned in a tank with degassed water. A steel block was put 15 mm away from the transducer to act as the target. Electrical pulse generated by Olympus 5077PR Square Wave Pulser/Receiver (Panametrics Inc., Waltham, Massachusetts, USA) was used to excite the transducer at 100V. Reflected impulse was first conditioned by the pulser/receiver and then measured and stored by the Agilent DSO7104B Digital Storage Oscilloscope (Agilent Technologies Inc., Santa Clara, California, USA). The obtained impulse response was then used for determination of sensitivity and bandwidth.

Beam profile and high pressure at focal point were measured with a high power hydrophone (Onda HNA-0400, Onda Co., Sunnyvale, California, USA). In beam profile plotting, low input voltage of 56 Vpp was used to make sure of the safety of the hydrophone considering the long time exposure (almost an hour). The input of the transducer was set as bursts of 10 Hz RPF

with 5-cycle sine wave in each burst. The transducer was held in a stable fixture and hydrophone moved in the emission field to scan the pressure around the focal point. Motion of the hydrophone was controlled by a 3-dimensional stage powered by step motors in each dimension. High pressure at the focal was measured with increased voltage. Excitation type was the same as above, i.e. bursts of 10Hz RPF with 5-cycle sine wave in each burst. Hydrophone position was adjusted automatically and then fixed at the focal point with increasing voltage through the measurement. In the beam profile measurement, either long time exposure or very high pressure exposure happened to the hydrophone. As a result, low RPF (10 Hz) and burst with 5-cycle sine wave was used to excite the transducer.

2.4 Tissue ablation

For hyperthermia ablation comparison between single frequency and dual frequency ultrasound, acoustic power transmitted into tissue should be remained constant. For example, if 6 W was used in tissue ablation, then input power of all frequency combinations was adjusted so that the output acoustic power is 6 W. Power output of the transducer versus the input voltage was calibrated with an ultrasound power meter (Model UPM-DT-1AV, Ohmic Instruments Co., Easton, Maryland, USA). A single channel arbitrary function generator AFG3101 (Tektronix Inc., Beaverton, Oregon, USA) was used to provide waveforms needed, which was amplified by an RF power amplifier Model 3100L (Electronic Navigation Industries Inc., Rochester, New York, USA). Continuous sine waves with different voltages were supplied to the transducer and power was measured by the ultrasound power meter. The

amplification of the RF power amplifier is fixed, so voltage of continuous wave was adjusted by the function generator. With the monitor of the ultrasound power meter, voltage needed for each ultrasound type to generate 6 W was recorded, and used later in tissue ablation for comparison.

Tissue ablation tests with the dual frequency transducer using single-frequency and multi-frequency HIFU was carried out for ablation efficiency comparison. Packaged pork loin tissue was brought to room temperature and left in open air for 30 minutes before being used for experiments. The tissue was cut to obtain a clean, flat surface from a bulk piece, and then mounted into a 50-mm depth and 150-mm diameter plastic container. Thin steel needles were used to hold the tissue in the designed position relative to the container. The axial ultrasound beam was perpendicular to the tissue surface and focused at 5 mm certain depth into the tissue sample. A depth of 5 mm was chosen to avoid significant heat dissipation into water. Temperature was measured to numerically indicate the tissue ablation efficiency. A needle thermocouple probe (Omega HYP0, Stamford, Connecticut, USA) with diameter of 0.2 mm was positioned inside tissue at the focal zone to measure the local tissue temperature. A needle thermocouple was chosen to minimize acoustic field interference in tissue. This T-type (Copper-Constantan) thermocouple probe is enclosed in a long hypodermic needle, and also has a fast response with a continuous temperature rating below 200 °C. The thermocouple signal was acquired via data acquisition system (USB-6361, National Instrument Corp., Austin, Texas, USA) for signal recording and processing.

The porcine tissue sample and HIFU transducers were aligned as described. Ultrasound transducers and data acquisition system for temperature recording were triggered at the same time. Each measurement consisted of a 45 seconds ultrasound exposure at 5 mm below the tissue surface. Signals from thermocouple were simultaneously sampled at a rate of 100 samples per second. The output acoustic power of 6 W was introduced for both single and dual frequency modes to compare the temperature rises. Each test under the same condition was repeated three times to obtain the average value. Dual frequency signal was generated by a function generator (Tektronix AFG3101, Beaverton, Oregon, USA). The ratios of the amplitudes of each frequency component were 1:1, 1:3, 1:5 and 1:10 (1.5 MHz: 3 MHz), and waveforms are shown in Figure 2.5. Relative magnitude of the two frequency components could be easily switched from the input waveform.

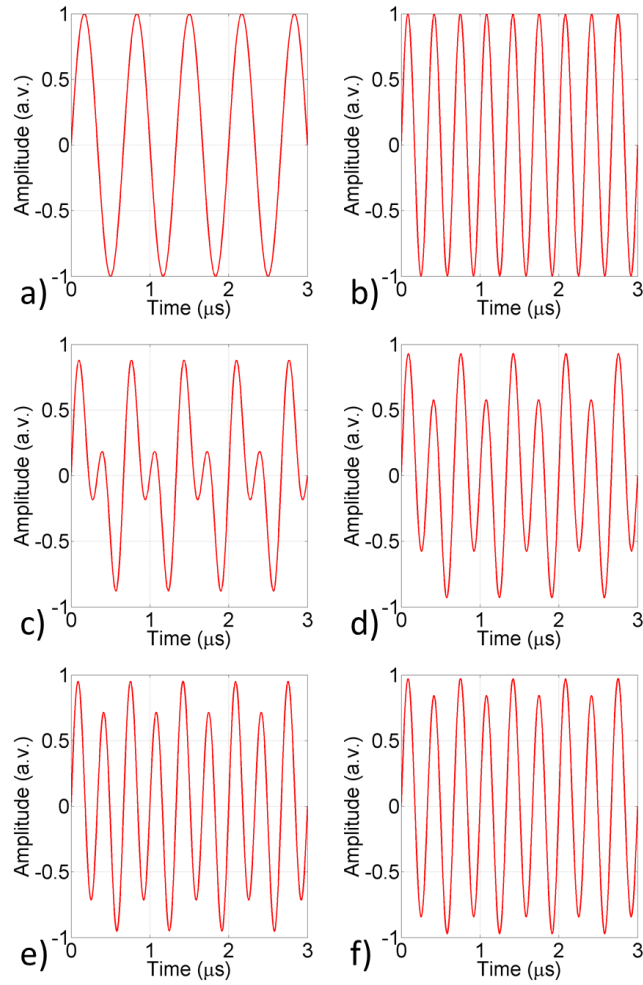


Figure 2.5 Signal waveforms generated by the function generator. a) 1.5 MHz signal. b) 3 MHz signal. (c-f) dual frequency signals. The rate of amplitudes between 1.5 MHz and 3 MHz is c) 1:1, d) 1:3, e) 1:5 and f) 1:10 respectively.

2.5 Results and discussion

2.5.1 Transducer prototype

The final transducer fabricated is shown in Figure 2.6. Electrical connection is led by two BNC cables. Center wires of both cables are connected together to the middle layer of the transducer. Shielding wire of the two cables are connected to the front and back surfaces of the transducer. To excite one layer of the transducer, only one of the cables is connected to power amplifier. To excite both layers, the two cables are connected both to power amplifier via a T-shape signal splitter.

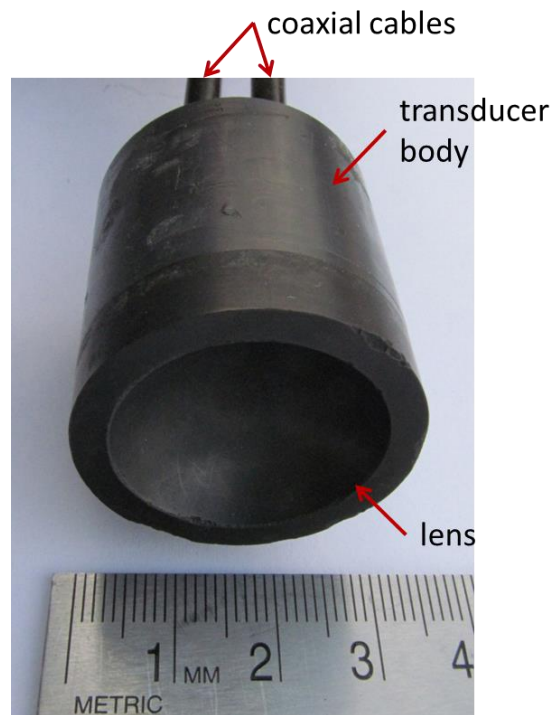


Figure 2.6 Photograph of the fabricated dual frequency transducer.

2.5.2 Electrical characteristics

Electrical impedance and phase spectrum were modeled separately for 1.5 MHz and 3 MHz and the results are shown in Figure 2.7. In the modeling result of the 1.5 MHz transducer, one resonance is found at 1.5 MHz. Large aperture of the transducer makes the electrical impedance low. With thin matching layer and very light (0.5 MRayl) backing layer, the phase at resonance is close to 60° . For the 3 MHz modeling, as predicted, there are two resonant frequencies at 1.5 MHz and 3 MHz respectively, which means the transducer works at two different vibration modes.

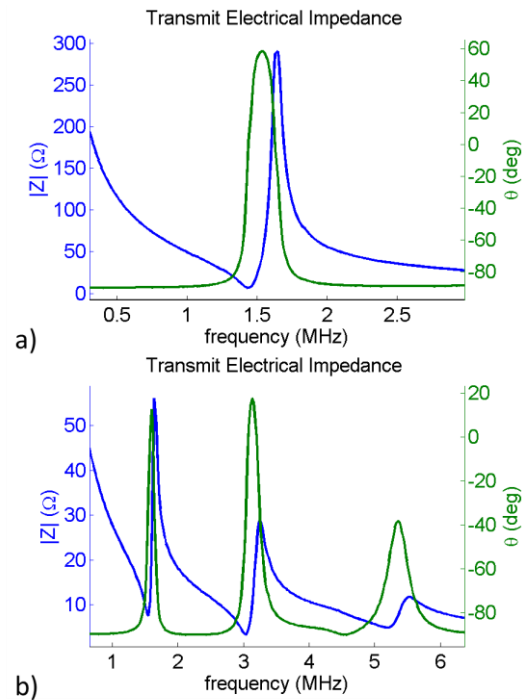


Figure 2.7 Impedance and phase of the transducer with a) both layer excitation and b) front layer excitation.

Transmitting response was simulated for each frequency with 10-cycle sine wave burst excitation. Driven with the two frequency components, the transducer was expected to generate ultrasound with both frequencies. Based on the modeling, 1.81 kPa/V and 2.85 kPa/V were expected for 1.5 MHz and 3 MHz ultrasound at the surface of the transducer. Detailed transmitting response is shown in Figure 2.8.

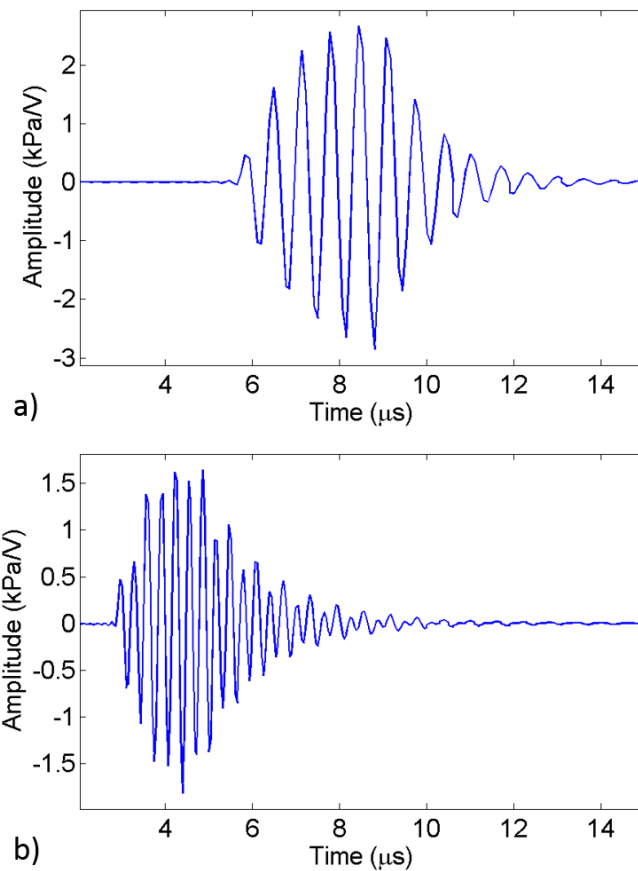


Figure 2.8 Acoustic pressure output with 5-cycle burst input at a) 1.5 MHz and b) 3 MHz.

2.5.3 Pulse-echo test

Pulse-echo test was carried out in water tank, with 100 V supplied to the transducer as excitation. A steel block 15 mm away from and facing to the transducer acted as the reflection target. Echo signal of impulse is shown in Figure 2.9 a). Ringing of the echo signal is a little bit long because of the light backing and little matching in the transducer. FFT spectrum in Figure 2.9 b) clearly shows two strong resonant frequencies at about 1.5 MHz (f_1) and 3 MHz (f_1') with almost identical amplitudes. This directly proved the capability of the transducer on generating 1.5 MHz and 3 MHz ultrasound, and agrees well with the simulation results. Relative to the base band frequency ($f_1 = 1.5MHz$), high order of harmonics of the transducer at 4.5 MHz (f_3) and 7.5 MHz (f_5) are very low, with an amplitude of -12.61 dB and -49.29 dB respectively.

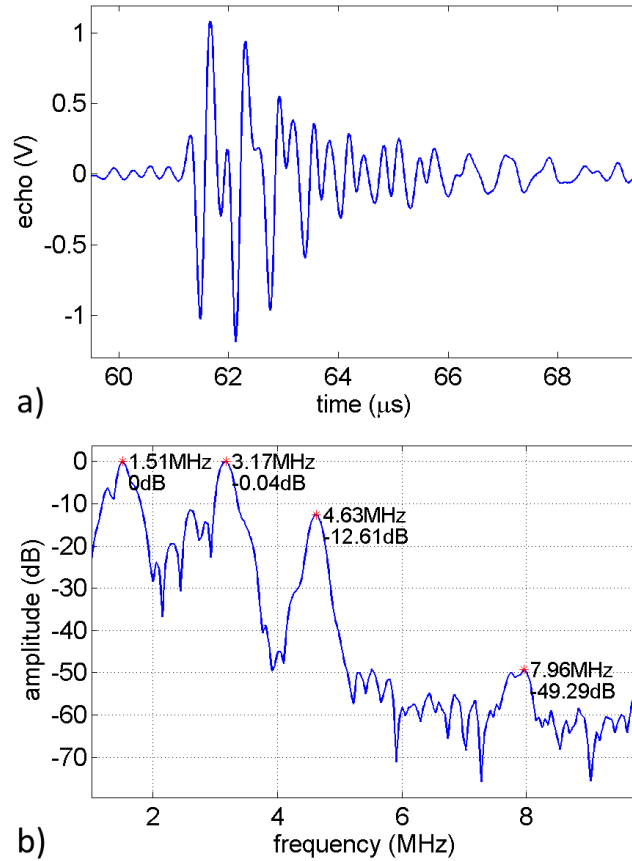


Figure 2.9 a) Reflected waveform and b) FFT of the waveform in pulse-echo test.

2.5.4 Beam profile

Beam profile of the acoustic field was simulated with Field II and measured with high power hydrophone. Simulation results are shown in a), c) and e) in Figure 2.10. Because of stronger focusing, the 3 MHz ultrasound shows smaller focal zone than the 1.5 MHz ultrasound. The pressure of 3 MHz ultrasound at focal point is 8.39 MPa compared to 6.64 MPa for 1.5 MHz ultrasound, corresponding to a power density of 2.35 kW/cm² for 3 MHz ultrasound beam and

1.47 kW/cm² for 1.5 MHz ultrasound beam, respectively. With the same voltage input, the pressure of the dual frequency ultrasound is 8.30 MPa and the power intensity is 1.48 kW/cm². Such power density is high enough to cause cavitation and hyperthermia effect, and thus resulting in lesion in bio-tissue [67].

Profile of pressure distribution around the focal point was mapped with hydrophone at 56 V_{pp} inputs. Result of the scanned field around focal point is shown in b), d) and f) in Figure 2.10. As listed in Table 2.3, the beam width and focal depth are much larger than that in the simulation. One of the main reasons might be the inaccurate location of the focal point. The focal zone is very sharp (-3 dB beam width of 0.35 mm for 3 MHz ultrasound) while the resolution of mechanical scanning of the water tank system is 0.5 mm. As a result, it is unlikely to measure the very peak value and the beam thus seems less focused. Profile of pressure distribution was measured at low pressure with low driving voltage. If driven by high voltage as used in HIFU application, more nonlinear effect is expected and the beam profile differs slightly [108].

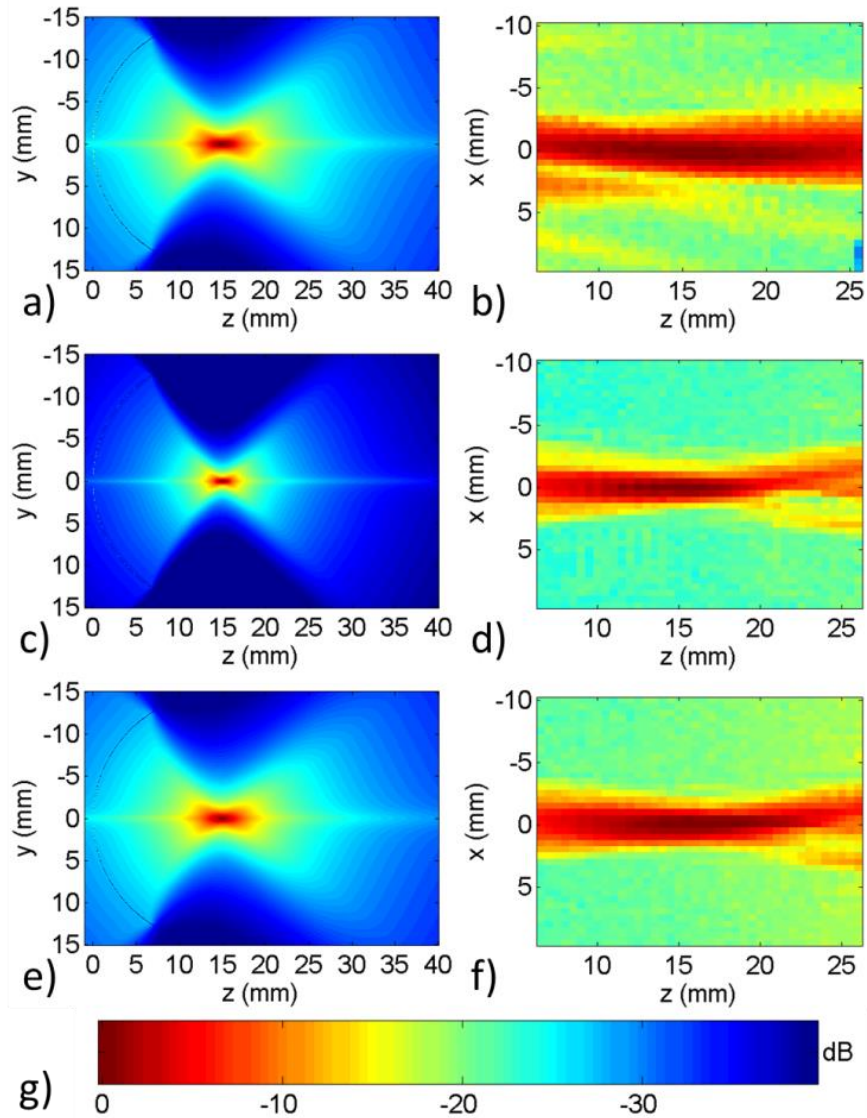


Figure 2.10 Ultrasound beam profile with frequency of a) & b) 1.5 MHz, c) & d) 3 MHz and e) & f) dual frequency. Figures a), c) and e) are from simulation while b), d) and f) are from hydrophone measurement. g) Color bar is shared by all the figures.

A collection of the beam profile parameters is shown in Table 2.3. Note that the wave of dual frequency ultrasound is not sinusoidal wave, and the power density is calculated by

integration instead of $\frac{P^2}{2Z}$, where P is the pressure magnitude and Z is the impedance of medium.

Table 2.3 Beam profile of the acoustic field. Beam width and depth are referred to -3dB value.

	frequency	1.5 MHz	3 MHz	dual
from simulation	focal length (mm)	15	15	15
	peak pressure (MPa)	6.64	8.39	8.30
	peak power density (kW/cm ²)	1.47	2.35	1.48
	beam width (mm)	0.65	0.35	0.45
	focal depth (mm)	2.15	1.1	1.65
from measurement	focal length (mm)	16.5	15	16.5
	peak pressure (MPa)	2.81	3.64	3.29
	peak power density (kW/cm ²)	0.263	0.442	0.233
	beam width (mm)	2	1.5	1.5
	focal depth (mm)	16.5	9	12.5

Acoustic pressure generated by the transducer at different voltages and frequencies was measured using the high power hydrophone and the results are shown in Figure 2.11. Compared to the simulation, the pressure measured from the hydrophone is lower. Several possible factors may cause this. One factor might be the low scanning resolution as mentioned above, which will lead to inaccurate position of focal point. Another reason may be the imperfectness of the transducer lens, causing the less focused effect as shown in the beam profile.

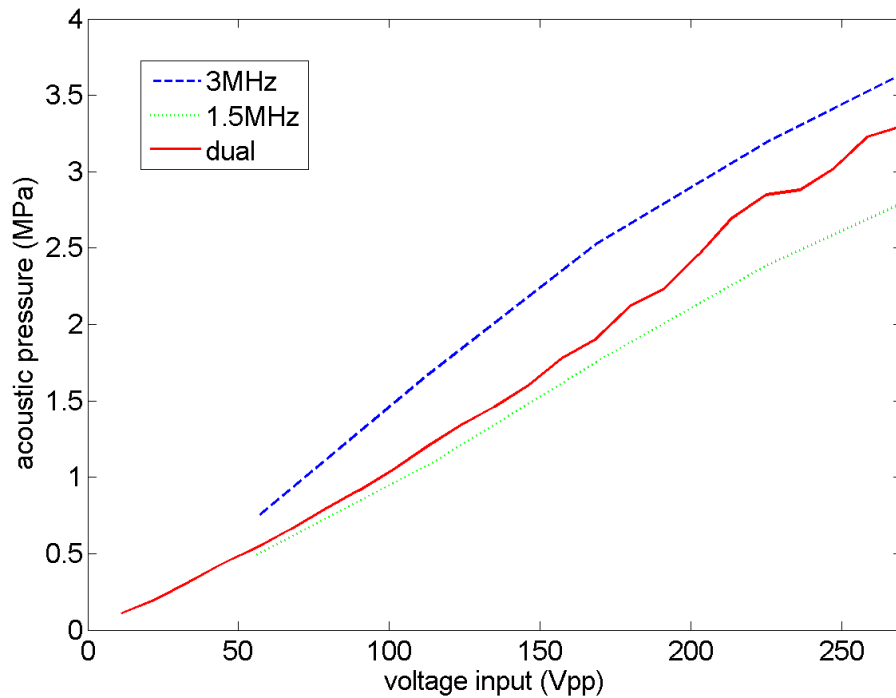


Figure 2.11 Acoustic pressure generated by the transducer with different frequency configurations. In this case, the dual frequency means 1.5 MHz and 3 MHz with 1:1 amplitude ratio.

2.5.5 Tissue ablation

To make tissue ablation comparison among single frequencies and dual frequency modes, acoustic power calibration of the transducer at 1.5 MHz, 3 MHz and dual frequency (1.5 MHz + 3 MHz) was performed to ensure that temperature rise of tissue ablation was compared under the same emitted ultrasound power. Ohmic Ultrasound Power Meter UPM-DT-1AV (Ohmic Instruments, St. Charles, Missouri, USA) was used for the acoustic power measurements. Input voltage was adjusted to generate a given power output. Voltage inputs for an output of 6 W at single frequencies and dual frequency are listed in Table 2.4. In case of dual frequency power measurements, input voltage signal ratio from the function generator of 1.5 MHz to 3 MHz was varied from 1:1 to 1:10 (shown in Figure 2.5) and the required input voltages applied to the transducer were obtained (Table 4).

Table 2.4 Voltage to be applied to the transducer to generate 6 W acoustic power.

Function generator signal	Transducer voltage
1.5 MHz	130 V
3 MHz	111 V
1.5 MHz + 3 MHz (1:1)	148 V
1.5 MHz + 3 MHz (1:3)	128 V
1.5 MHz + 3 MHz (1:5)	121 V
1.5 MHz + 3 MHz (1:10)	114 V

Under the acoustic power of 6 W at different frequencies, the temperature measurement results are shown in Figure 2.12. Measurement of each curve were repeated at least 3 time with the same setup and the temperature rise was very consistent with an error less than 0.2 °C. For porcine tissue ablation, highest temperature rise was found with dual frequency ablation with amplitude ratio of 1:10 (1.5 MHz : 3 MHz in amplitude). However, with dual frequency input, the acoustic pressure distribution is between the two single frequency experiments (Figure 2.11), which means that the peak pressure at dual frequency is lower than that of single frequency 3 MHz ultrasound and higher than that of single frequency 1.5 MHz ultrasound. Therefore, this finding cannot be explained by the linear bio-heating theory where tissue temperature rise increases with acoustic pressure in tissue [64].

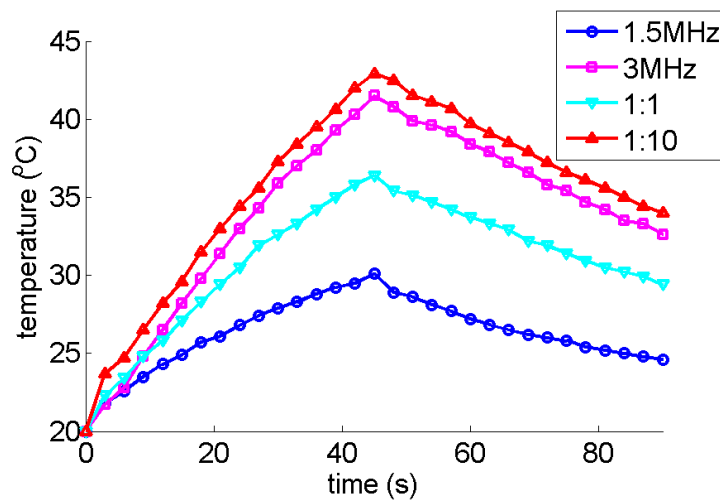


Figure 2.12 Porcine tissue ablation tests using single-frequency ultrasound and dual frequency ultrasound with different frequency components under the same power (6 W). In the figure, single frequency ablations are shown with 1.5 MHz and 3 MHz for corresponding frequency. For dual frequency ablations, relative amplitude ratios of 1.5 MHz and 3 MHz are shown as 1:1 and 1:10.

The measured results are similar to previous observations on multi-frequency ablation using different frequencies and tissue materials [93], and larger lesion size was induced by dual frequency ultrasound than that by single frequency ultrasound. Dual frequency ultrasound can generate higher temperatures under the same exposure condition may be attributed to the cavitation yield at different frequencies, even when frequency difference is greater than 500 kHz. The frequency differences in multi-frequency mode may result in a low-frequency homogeneous acoustic wave, which will enhance the cavitation effect, according to Iernetti and Feng [109, 110]. A combination of two different frequencies may even result in the formation of constructive and destructive interference patterns that composed of waves with a wide range of different frequencies and pressure amplitudes. Cavitation is a random frequency dependent phenomenon, and thus the generation of waves with different frequencies increases the chance of more efficient energy dissipation during cavitation.

2.6 Summary

To achieve high efficiency HIFU ablation without introducing complexity to system or application, a single aperture, dual frequency HIFU transducer was designed, fabricated and characterized. Pulse-echo experiment shows that the amplitudes of two frequency components are almost equally strong, leading to the advantage that acoustic power output could be easily tuned from function generator input. Preliminary experiments on tissue ablation showed that higher tissue ablation efficiency can be expected from dual frequency ablation compared to single frequency ones. With proper combination of the two frequency components in the

function generator output (e.g. 1:10 of 1.5 MHz: 3 MHz in amplitude) and the same acoustic power output from the transducer, temperature rise measured was consistently more than that induced by single frequency ultrasound. Dual frequency induced temperature rise was 5% higher than that generated by single frequency 3 MHz ultrasound even with less focusing and more than 100% higher than that generated by single frequency 1.5 MHz ultrasound partially because of better focusing. This finding suggests that that dual frequency HIFU can be an effective approach for more efficient tissue ablation.

Chapter 3.

Dual Frequency Intravascular Super-Harmonic Imaging Transducer

3.1 Background

It is well known that atherosclerotic cardiovascular disease is a leading cause of death worldwide, and one which often manifests without warning [111]. According to the 2014 update of Heart Disease and Stroke Statistics by the American Heart Association [112], there are more than 2000 deaths every day in United States on average, which is 1 death in every 40 seconds. For up to 75% of acute coronary syndromes, the underlying pathological mechanism is hypothesized to be atherosclerotic plaque rupture [111]. Unfortunately, a high percentage of vulnerable plaques are also angiographically occult, and these are responsible for a high proportion of ensuing cardiac events resulting in either fatalities or requiring further interventional treatment [113, 114]. For this reason, detection and characterization of plaques which are rupture prone is one of the most active areas of research in cardiology and biomedical imaging [115]. The vasa vasorum is a network of microvessels which supports larger vessels such as the aorta, and increased density of the vasa vasorum has been associated with a plaque advancing from a stable state to a rupture prone state [116, 117]. Additionally, intraplaque hemorrhage occurring from thin-walled, immature microvessels has been present in plaques in many cases of sudden coronary death [118]. Evidence suggests that vasa vasorum proliferation

and associated angiogenesis and inflammation is associated with plaque instability and rupture [118-121]. As our ability to predict the instability of atherosclerotic lesions remains a substantial challenge, there is an unmet need for new imaging methods to identify, detect, and differentiate these pathologies [122].

The new technology of ultrasound molecular imaging utilizes contrast agents displaying targeting ligands to identify areas of inflammation and angiogenesis associated with disease progression (targets that cannot be identified by B-mode ultrasound) [123-125]. Prior data suggests that ultrasound molecular imaging will provide a unique opportunity for plaque biomarker evaluation (such as inflammatory or angiogenic markers) and for identification of vulnerable plaques [126]. Additionally, a new high-frequency contrast imaging technique, acoustic angiography [4], takes advantage of exciting microbubbles near resonance and detecting their high-frequency, broadband harmonics with sufficient bandwidth separation to achieve both high resolution and high contrast-to-noise ratio (CNR). Data has shown that acoustic angiography enables detailed visualization and analysis of microvascular structure [4, 127], and will likely be applicable to vasa vasorum imaging. Thus, we hypothesize that there is a role for contrast enhanced ultrasound imaging in the assessment of atherosclerosis.

Feinstein has illustrated the potential of contrast enhanced transcutaneous ultrasound imaging on the carotid artery [128], but the potential of transcutaneous ultrasound has limitations with resolution and motion artifacts [129], especially if the target is the deeper coronary arteries. This may present an opportunity for intravascular ultrasound (IVUS) [84], which has been widely utilized for the characterization of coronary vessel walls [83],

morphology of plaques [130], and so on. However, conventional IVUS transducers are not optimized for contrast imaging [131], and, therefore, are ineffective for vasa vasorum imaging. This absence of technology may be due to the fact that nonlinear detection strategies for contrast imaging are most effective near the resonant frequency of microbubble contrast agents, which is typically between 1-10 MHz [132]. Thus, conventional contrast imaging strategies are not very effective with high frequency ultrasound (35-50 MHz) that is typically used with IVUS. To overcome this challenge, Goertz and collaborators have been evaluating both subharmonic and harmonic contrast IVUS imaging, with the goal of vasa vasorum imaging [114, 133]. Their research showed a contrast-to-tissue ratio (CTR) of 28 dB in subharmonic imaging with a fundamental frequency of 30 MHz [114] and 25 dB in second harmonic imaging with a fundamental frequency of 20 MHz [133].

We hypothesize that resolution and contrast to tissue ratios can be further improved over subharmonic or harmonic contrast IVUS imaging by excitation of microbubbles near resonance and detecting their backscatter at a bandwidth substantially higher than that of the transmission, previously called “super-harmonic,” “ultra-broadband,” or “transient” imaging. In prior work, de Jong [134], Bouakaz et al [135], and Kruse et al [136] demonstrated that substantial improvements in CTR could be achieved by detecting the high frequency energy produced by microbubbles excited at lower frequencies. Bouakaz et al utilized a dual frequency transducer to illustrate that the CTR of the 4th and 5th harmonic could be 15 and 7 dB higher than that of the 2nd harmonic, respectively [135]. Kruse et al also utilized a dual frequency transducer arrangement, and demonstrated that substantial scattered energy from

microbubbles excited near 2 MHz could be detected at a frequency as high as 45 MHz. More recently, Gessner et al [4, 127, 137] utilized mechanically-scanned dual frequency transducers (transmit at 2 or 4 MHz, and receive at 30 MHz) on the Visualsonics Vevo770 to perform high frequency 3-D contrast imaging of *in vivo* microvasculature and achieved resolution on the order of 100 microns with a CTR high enough so that microvessels could be readily segmented from the images and their morphology analyzed.

Despite the promising CTR and vessel imaging capability of this imaging approach, there is a substantial challenge for “ultra-broadband” contrast enhanced intravascular ultrasound (CE-IVUS), which is likely why it is yet relatively undeveloped. The primary limitation is the large frequency span, which is outside of the current bandwidth of commercially available single frequency transducers. Such difficulty could be surmounted by using multiple confocal transducers as described by Gessner [137], however, such transcutaneous exposure method is almost impossible to be used for coronary vasa vasorum imaging due to penetration depth limitation and existence of ribs at the chest. Furthermore, it is hardly acceptable to decrease the frequency for a larger penetration depth because high resolution is needed for the vasa vasorum (diameter of 161 μm for the first order and 68 μm for the second order) [138] imaging, which requires frequency usually > 20 MHz. Intravascular ultrasound (IVUS) imaging may be a solution to this challenge of penetration depth, and has been widely utilized for the characterization of coronary vessel walls [83], morphology of plaques [130], and so on. However, conventional IVUS transducers are not optimized for contrast imaging, and,

therefore, are ineffective for vasa vasorum imaging. Up to date, there is no commercial transducers that could be used for IVUS super-harmonic vasa vasorum imaging.

In this study, small aperture, dual frequency, IVUS transducers are introduced [139, 140], which provide sufficient bandwidth separation for high CTR, high-resolution CE-IVUS imaging. Design, fabrication, characterization and super-harmonic imaging capabilities were demonstrated. The imaging performance of the transducers were improved by changing the transmitting frequency and materials. High resolution (70 μm), high CTR (23 dB) images of microbubbles could be generated by the dual frequency transducers, indicating the potential imaging capability of second order vasa vasorum.

3.2 Dual frequency IVUS transducer

3.2.1 Transducer design

There are several alternative structures of the dual frequency transducer design (Figure 3.1). One structure is to put the high frequency element and the low frequency element side by side, which is named as interleaved structure (Figure 3.1 a) [141, 142]. Advantage of this structure is the low crosstalk between the high frequency and the low frequency elements. However, this structure has misaligned beam profile between the two frequencies and the transmitting pressure was too low in the sensitive region of the high frequency beam ($x = -0.2, y = 0$ in Figure 3.2). If the elements are stacked in layers (Figure 3.1 b), then the transmitting and receiving beam would have the best overlap because of the identical aperture. However, it is impossible to make the electrical impedance match for both elements. The low frequency

element is thicker than the high frequency element, so that the capacitance is lower.

Consequently, the impedance ($Z = \frac{1}{j\omega C}$) of the low frequency element is significantly higher

than the high frequency element due to low ω and low C . Furthermore, the natural focus point (near-field and far-field transition) of the two beams are also significantly different if the

aperture of the two elements are the same. Based on these concerns, the structure of the transducer was designed as stacked layers with different apertures between the two active elements (Figure 3.1 c).

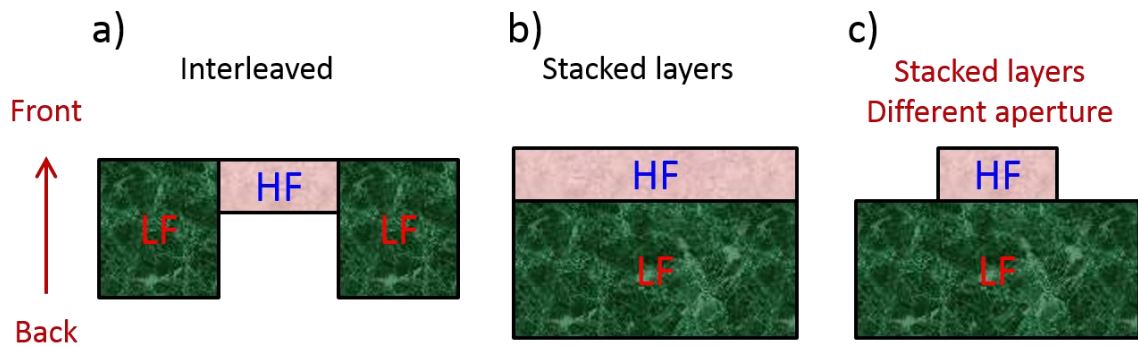


Figure 3.1 Structural dual frequency transducer design alternatives.

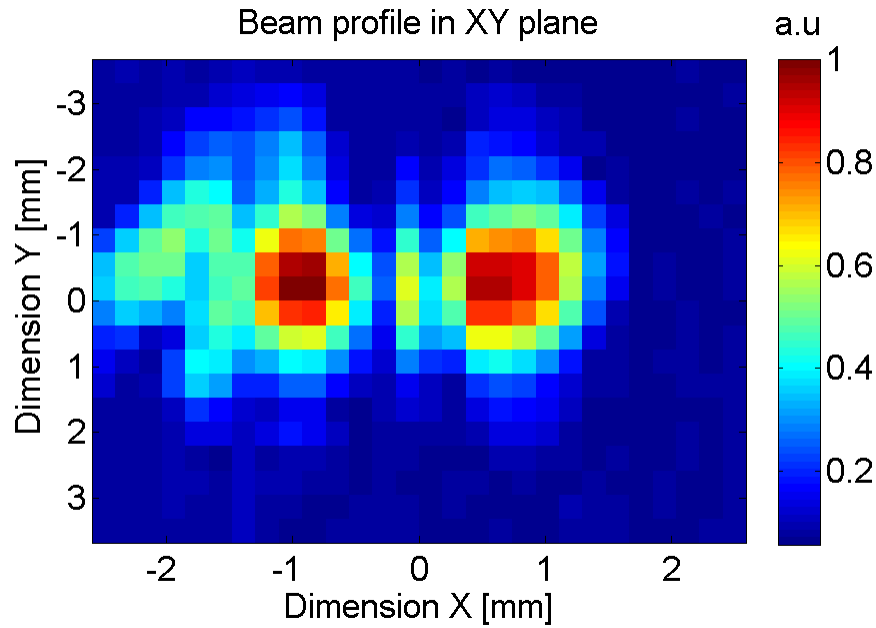


Figure 3.2 Beam profile of the low frequency transmitter in the interleaved structure transducer.

With details included, the dual frequency transducer was designed as a dual layer transduction structure, composed of a low frequency transmitting layer and a high frequency receiving layer (Figure 3.3) [140]. The transmission layer was placed behind the receiving layer (with respect to a forward traveling sound wave) since low frequency transmitted acoustic waves could propagate through the smaller, high frequency element. The placement of the receiving layer counted in the matching network of the low frequency transmission element, which showed positive effect that amplifies the low frequency propagation wave. The selection of 6.5 MHz as the transmitting layer's center frequency was because it was both close to the contrast agents' resonant frequency and since the piezoelectric material for this element was readily available. The high frequency receiving layer was positioned in the front of the

transducer to achieve an optimal receiving performance of the high frequency element. If the two active layers are directly bonded together, then the high frequency receiving signal would continue propagation after being detected by the receiving element, the reflection of which at back side of the transducer would cause aliasing echoes that show up after the real signal. Such aliasing echoes could either cause fake imaging signal (if each echo is considered as signal) or reduce the resolution (if the series of echoes are considered as one signal). An acoustic filter with a quarter wavelength of 30 MHz was placed between the two piezoelectric layers to enhance the low frequency transmitting wave penetration, while reflecting the high frequency receiving wave to suppress the aliasing echo [143]. Detailed analysis of the acoustic filter will be described in Chapter 4. Transducer dimensions were optimized using a KLM model [105] to validate the thickness of layers, length, and width of each component for ideal thickness mode excitation. The aperture of the high frequency (0.5 mm x 0.6 mm) receiving layer was designed to be similar to that of commercial IVUS transducers [144], and thus significantly smaller than that of the transmission layer (3 mm x 0.6 mm). The relatively large aperture of the low frequency component was designed to obtain reasonably low electrical impedance at low frequencies for higher acoustic pressure transmission. The modeling of the 30 MHz element considered the existence of the 6.5 MHz element at Side B (back side) as backing according to the structure of the design in Figure 3.3 [86].

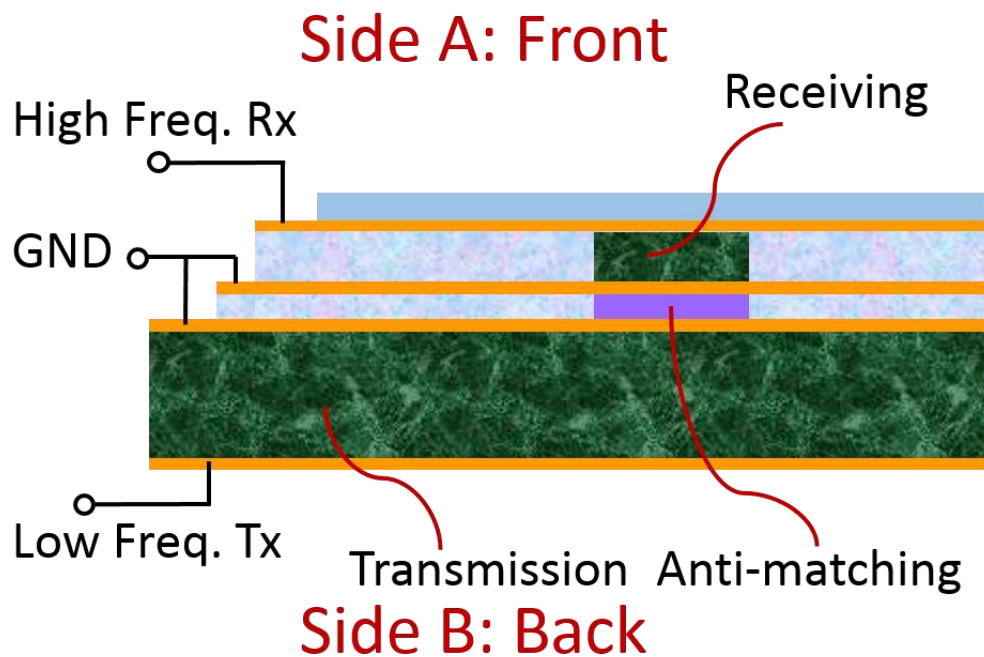


Figure 3.3 Side view of the dual frequency IVUS transducer design.

High efficiency is essential for the transmission in the space limited intravascular environment. First, in order to excite the nonlinearities of microbubbles, the super-harmonic imaging requires relatively higher peak negative pressure (PNP, > 0.6 MPa) than B-mode imaging. High performance (d_{33} , k_t) piezoelectric materials are critical. Second, high dielectric constant material is preferable due to the small aperture of the IVUS transducers. Third, the transducers work in low power, low temperature conditions so that high power piezoelectric materials are not necessary. According to the material properties listed in Table 3.1, magnesium niobate-lead titanate (PMN-PT) was selected to meet the requirements. The design of the transducer used lead PMN-PT instead of polyvinylidene fluoride (PVDF) for the

receiving layer since the sensitivity could be higher due to the following [145]: (1) Compared to PVDF, PMN-PT has a much higher piezoelectric and electromechanical coupling coefficient and (2) the dielectric constant of PMN-PT is 400 ~ 700 times higher than that of PVDF, making it easier to match the electrical impedance to the receiving system. Material properties and final optimized parameters for modeling and fabrication are summarized in Table 3.2.

Table 3.1 Typical parameters of some candidate piezoelectric materials

Parameters	PZT-5H	PMN-PT single crystal	PMN-PT 1-3 composite	PVDF
Dielectric ϵ_r	1800	4000 - 6000	~ 3000	9
d_{33} (pC/N)	640	2000	2000	-30
k_t	0.5	0.6	> 0.7	0.15
Sound speed (m/s)	4400	4400	3950	1400
Impedance (MRayl)	34	35	18	2.5
Curie temperature (°C)	350	160	160	135

Table 3.2. Fabrication parameters of the dual frequency transducer.

Parameters	6.5 MHz layer	30 MHz layer
Active material	PMN-PT	PMN-PT
Thickness (μm)	300	65
Width (mm)	0.6	0.6
Length (mm)	3	0.5
Sound speed (m/s)	4400	4400
Impedance (MRayl)	35	35
Matching material	$\text{Al}_2\text{O}_3/\text{epoxy}$	Parylene
Thickness (μm)	80	15
Sound speed (m/s)	2800	2770
Impedance (MRayl)	5.5	3.16
Attenuation (dB/cm/MHz)	4.3	0.1
Backing material	Ag/epoxy	Ag/epoxy (anti-matching)
Thickness (μm)	200	15
Sound speed (m/s)	1900	1900
Impedance (MRayl)	5.15	5.15
Attenuation (dB/cm/MHz)	8	8

3.2.2 Fabrication

In the fabrication of the dual frequency transducer, a 5 x 5 mm piezoelectric acoustic stack was first assembled and then diced into 0.6 mm wide slices as individual transducers. The assembly process started with a 5 x 5 mm PMN-PT plate which was lapped to 300 μm ($f = 6.5$ MHz) in thickness and then coated with Ti/Au (Ti: 10 nm and Au: 100 nm, E-Beam, Jefferson Hills, Pennsylvania, USA) on both surfaces (Figure 3.4-1). A second piece of PMN-PT (0.5 x 5 x 0.3 mm) was then bonded on the first PMN-PT layer using conductive silver epoxy to form the high frequency receiving element and anti-matching layer [146]. Polystyrene microspheres (Polysciences Inc., Warrington, Pennsylvania, USA) having a nominal diameter of 10 μm was added (about 1% in volume) to the silver epoxy so that the thickness of bonding layer was controlled to be 13 - 15 μm in order to function as a anti-matching layer previously mentioned (Figure 3.4-2). After the silver epoxy cured, a composite layer of Al_2O_3 powder (1 μm grain size, Logitech Limited, Glasgow, UK) and Epo-tek 301 (Epoxy Technology Inc., Billerica, Massachusetts, USA) was mixed 1:1 by weight and centrifuged at 10000 RPM (5590 g) for 10 minutes (Microfuge Lite, Beckman Coulter Inc., Brea, California, USA). The prepared composite was then cast onto the front of the 5 x 5 mm PMN-PT layer beside the 0.5 mm width slice. A small margin (0.5 mm) at one edge was left as an electrical connection site for later wiring. After the Al_2O_3 /epoxy composite cured, it was then lapped until the bonded composite layer was 80 μm thick, making the thickness of the top PMN-PT layer 65 μm ($f = 30$ MHz) on top of the 15 μm anti-matching layer (Figure 3.4-3). Another Ti/Au layer (Ti: 10 nm and Au: 100 nm) was then deposited onto the top surface to form the top electrodes. The final stack

was then diced into 0.6 mm wide slices to form individual dual frequency transducers (Figure 3.4-4). Each slice was bonded to the tip of a 20 gauge hypodermic needle (Fisher Scientific International Inc., Hampton, New Hampshire, USA) and then coated with a layer of parylene film (15 μm). The parylene film served two purposes: (1) to act as a matching layer of the 30 MHz, high frequency element and (2) to provide electrical isolation in the form of a passivation layer for the entire transducer. Finally, the transducer was poled with a DC electrical field of 10 kV/cm for 15 minutes in silicone oil at room temperature.

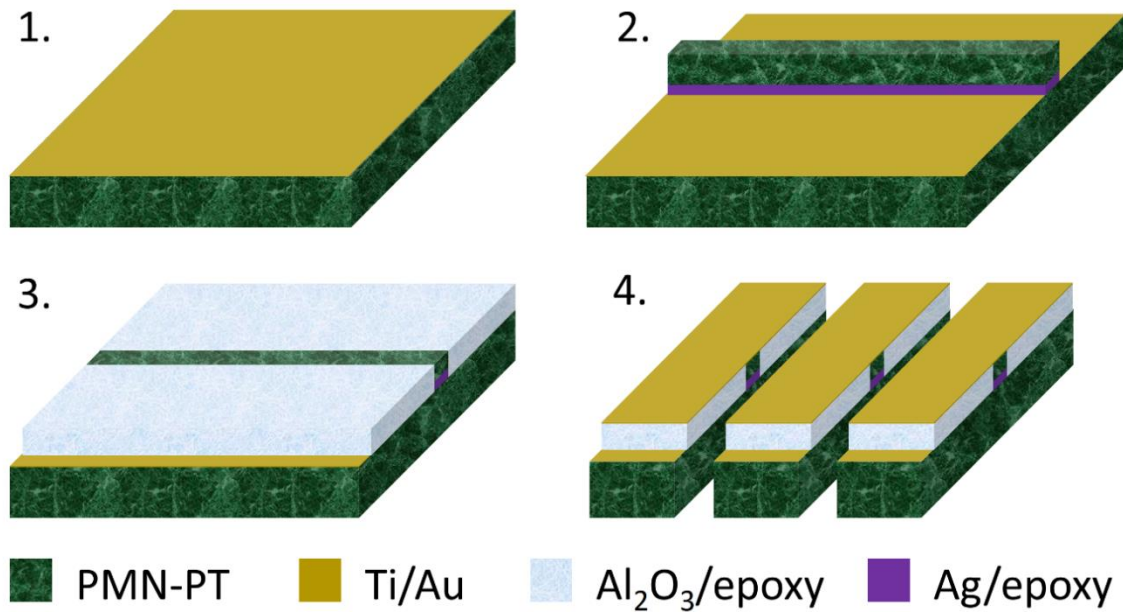


Figure 3.4 Fabrication process diagram of the dual frequency transducer.

After the transducers were poled, electrical characteristics such as capacitance, loss, and input electrical impedance were characterized using an Agilent 4294A Precision Impedance Analyzer (Agilent Technologies, Inc., Santa Clara, CA, USA). Capacitance and loss were measured at 1 kHz and the input electrical impedance was measured near the resonant frequency of each element, individually.

3.2.3 Acoustic characterization

The main design consideration for the low frequency (6.5 MHz) transmission element was peak negative pressure (PNP) and the pulse length. Large PNP (e.g. >1 MPa) is desirable to produce detectable nonlinear oscillations of microbubble contrast agents. Less pulse length with fewer number of negative peaks leads to higher resolution because each high pressure negative induces nonlinearities in the bubble, generating super-harmonic signal and decreasing the axial resolution. The pressure output of the small aperture transducer was measured using a calibrated needle hydrophone (HNA-0400, Onda Co., Sunnyvale, California, USA) positioned axially at 3 mm away from the transducer. This distance was kept constant (3 mm) between pressure measurements and subsequent microbubble tests in order to estimate pressure levels applied to the contrast agents. The excitation pulse used was a sinusoidal burst (1-5 cycles) at 6.5 MHz generated by the arbitrary function generator (AFG3101, Tektronix Inc., Beaverton, Oregon, USA) and amplified by 55 dB with a radio frequency amplifier (Model 3200L, Electronic Navigation Industries Inc., Rochester, New York, USA). The amplitude of the transmission signal was adjusted from 50 to 350 mV (peak to peak) prior to amplification. Pressure output of the transducer was recorded using an in-house LabVIEW (National

Instruments Co., Austin, Texas, USA) data acquisition system. Pulse length was defined as the -6 dB amplitude relative to the largest negative peak pressure, because pressure with amplitude less than -6 dB was considered too low to generate super-harmonic signals on microbubbles.

Sensitivity and pulse length are important characteristics of the receiving element for high CTR high resolution imaging. Receiving elements were characterized using the pulse-echo method. The transducer was excited by a customized pulser/receiver system [147] using a 20 V 1-cycle impulse. A steel block was placed in front of the transducer as the reflection target. Envelope of the echo was calculated as the absolute value of the Hilbert transformation on the time domain signal. Sensitivity of the transducer was defined as the amplitude of the envelope divided by the 20 V amplitude input. Axial resolution of the transducer was also calculated from the envelope with amplitude higher than a threshold (-6 dB or -20 dB).

3.3 Imaging tests

3.3.1 Microbubble response test

To validate the contrast response of the transducer, microbubbles were excited by the low frequency element and the nonlinear responses from microbubbles were detected using the high frequency element. Relative positions of the transducer and the tube were carefully adjusted in a water bath using a 3-axis precision rectilinear stage. In the alignment process, an acoustically transparent 200 μm diameter micro-tube was filled with air to provide a strong echo to indicate alignment in the lateral dimension of the 30 MHz element. Time of arrival of the echo was used to calculate the distance between the transducer and the tube in order to

position it axially 3 mm away from the transducer. Polydisperse lipid shelled microbubbles (Figure 3.5) were formulated as described previously [148] and pumped through the aligned micro-tube at a concentration of 4.8×10^8 MBs/mL at a velocity between 1.8-4.4 cm/s to maximize the signal response. The tube was slightly angled ($\sim 10^\circ$) with respect to the front surface of the transducer to reduce specular reflections from the wall of the tube.

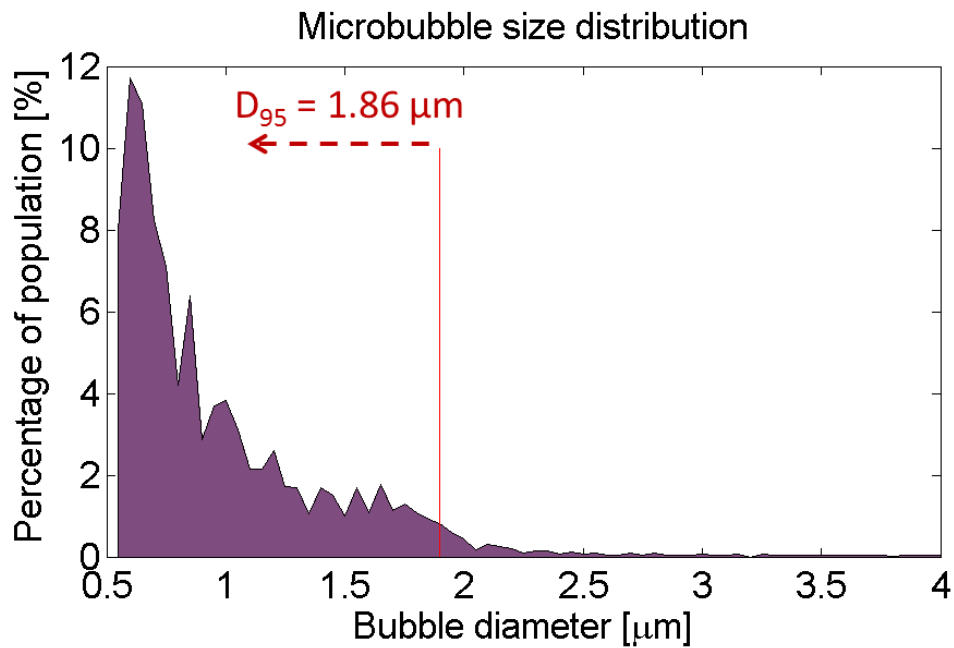


Figure 3.5 Microbubble size distribution.

Once the transducer was aligned and positioned for the contrast imaging, the excitation pulse sequence was adjusted for optimal imaging quality. A sinusoidal burst was used to excite the transmitting element with pulse lengths between 1 to 5 cycles and voltage variations from

50 to 350 mV_{pp} in 50 mV_{pp} increments. For each combination of testing parameters, 100 A-lines of microbubble echoes were received and recorded by the high frequency element for offline analysis. The contrast imaging data was evaluated using both time domain amplitude analysis and short-time Fourier transform.

3.3.2 Fundamental imaging

Fundamental imaging at 30 MHz and dual frequency super-harmonic contrast imaging were tested with the transducer in tissue-mimicking phantoms immersed in water (Figure 3.6). Typical phantoms had a speed of sound similar to tissue (1496 m/s), relatively high attenuation (0.9 dB/cm at 3MHz), and had fully developed speckle. A hole was drilled through the phantom by a thin wall steel tube (5.5 mm OD, 0.4 mm wall thickness) to simulate a vessel. After drilling, the dual frequency probe was placed in the center of the lumen and rotated to make an IVUS image. The rotation was controlled using a microcontroller that stepped the transducer at 0.9° angular increments for one revolution and provided a trigger for the excitation pulse. An acoustically transparent micro-tube with 200 μm diameter was placed through the phantom, running parallel to the channel to mimic the vasa vasorum. Diluted microbubbles were pumped through the tube (4.4 cm/s) while imaging. A 0.6 mm diameter steel rod was placed in the phantom opposite of the microbubble tube to provide a strong reflection target for comparison. Both the microbubble tube and the steel rod were embedded at ~ 4 mm radially in the phantom to test if the system could detect contrast in a scattering and attenuating medium, which is typical of tissue.

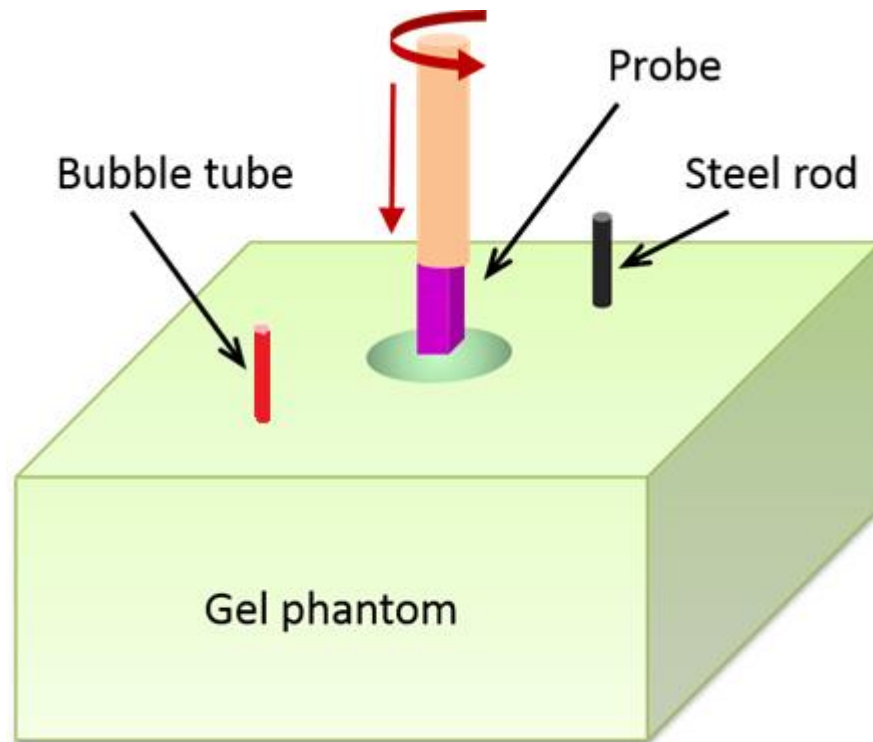


Figure 3.6 Experimental setup for the imaging.

The 30 MHz high frequency element was used for the fundamental imaging. In other words, both acoustic excitation and signal reception were performed using the 30 MHz element. A pulser/receiver supplied the transducer with a 1 μ J excitation pulse at every step and the reflected signal was recorded by the LabVIEW data acquisition system described previously.

3.3.3 Super-harmonic imaging

In super-harmonic imaging, the setup is similar as that for fundamental imaging except that the existence of the steel rod. For super-harmonic imaging, a 2-cycle sinusoidal burst generated by AFG3101 was amplified by the 3200L RF amplifier to excite the 6.5 MHz transducer while

the 30 MHz element was used for receiving. A synchronized 3-dimensional (3D) motion stage and a stepper motor (400 steps/rev) produced the mechanical scan for 3-D imaging. The 6.5 MHz element was excited by 1-cycle or 2 cycle burst using the imaging system, and the 30 MHz element received the high frequency super-harmonic signals. The signal was digitally band pass filtered with a frequency window of 25 MHz to 35 MHz corresponding to the receive element's bandwidth. Envelope of the wave was defined as the absolute value of Hilbert transform from the filtered signal. Contrast to tissue ratio (CRT) was defined as the amplitude of the envelope for contrast signal to the amplitude of the noise.

3.4 Preliminary results

3.4.1 Prototype and housing

The dual frequency transducer prototypes were housed on the tip of a 20 gauge hypodermic needles (Figure 3.7 a) for demonstration. The back surface (Side B in Figure 3.3) of the transducer was bonded to the needle with conductive epoxy, allowing the needle to function as an electrode leading to the back side of the 6.5 MHz transducer. Co-axial wires (25 gauge) were attached to the top electrode and common electrode between the two PMN-PT layers and then threaded through the needle.

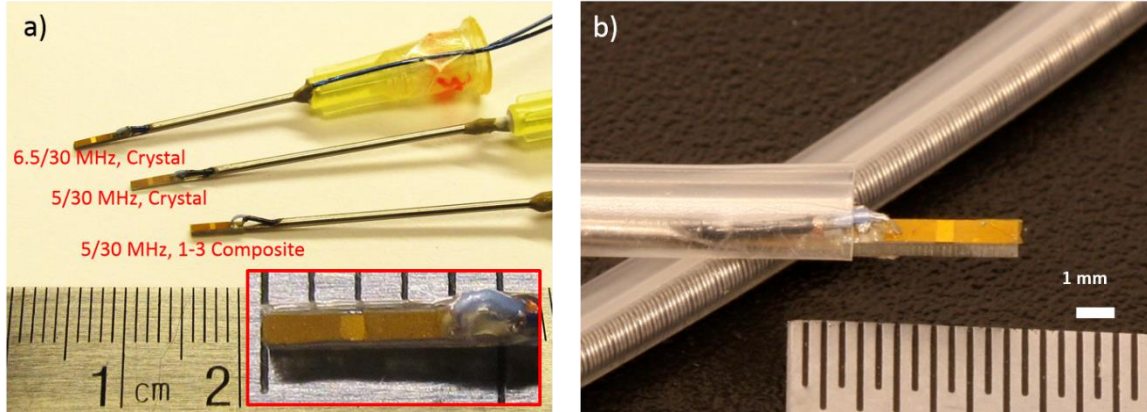


Figure 3.7 Prototype transducers a) housed on the tip of a 20 gauge hypodermic needle or b) integrated in a commercial catheter.

Eventually the transducers would be housed inside catheters used for IVUS imaging. The viability was demonstrated by housing the transducer into a commercial catheter (Figure 3.7 b) from Boston Scientific (Natick, Massachusetts, USA). Obviously the transducers are small enough to fit inside the IVUS catheters.

3.4.2 Electrical characterization

The capacitance and loss at 1 kHz (measured with an Agilent 4294A Precision Impedance Analyzer) showed good agreement to predicted values. Capacitance values of the transducers were 344 pF for the 6.5 MHz transmission element and 131 pF (including a 2 pF parasitic capacitance from Al_2O_3 /epoxy layer) for the 30 MHz receiving element. This data was in agreement with theoretical calculations using a relative dielectric constant of 4000 (HC Materials, Inc.). Loss of the transducer was 1.1% for transmission and 2.7% for reception, similar to the properties of PMN-32%PT.

The measured input electrical impedance at the resonant frequency (Figure 3.8 b, d) matched well with the results of the KLM modeling (Figure 3.8 a, c). In order to obtain a strong resonance for high pressure output in the transmission element, the backing layer of the transmission element was designed with reasonable absorption for compromise of achieving sufficient pressure output while minimizing ringing. In both the modeling and measured results, a strong resonance occurred at 6.5 MHz (Figure 3.8 a, b). The center frequency of the receiving element was designed to be 30 MHz (Figure 3.8 c, d) and the measured results agreed very well with simulations.

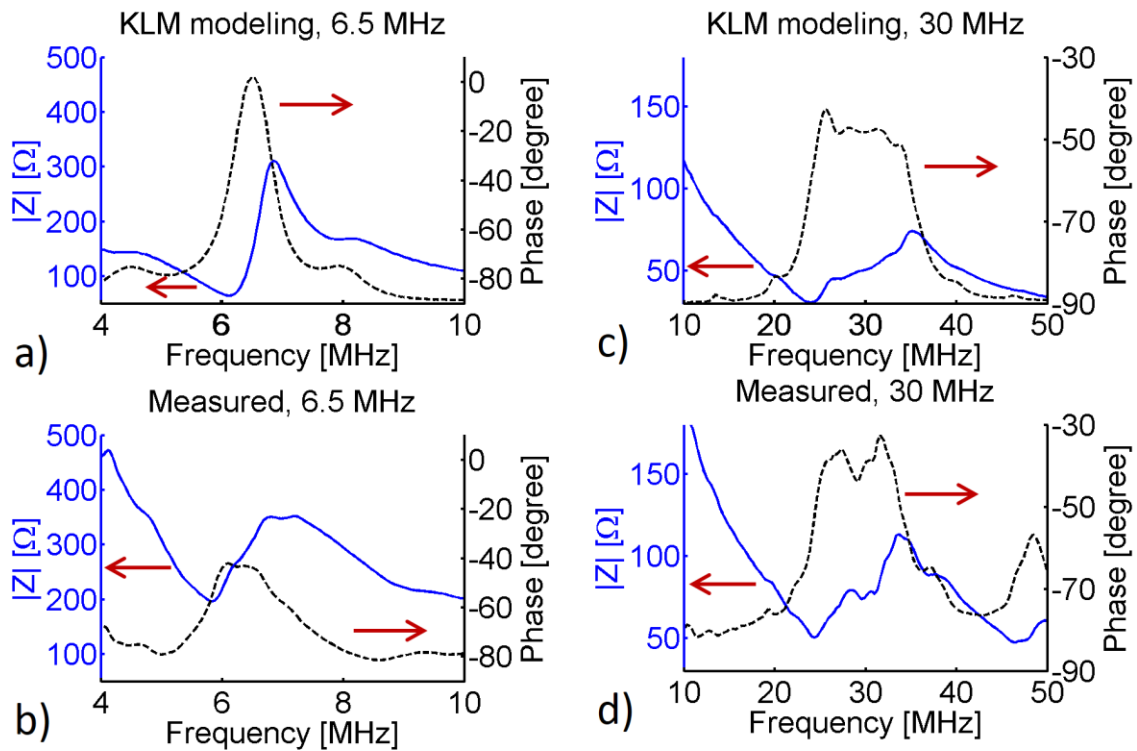


Figure 3.8 Electrical impedance of the a), b) 6.5 MHz element and c), d) 30 MHz from a), c) KLM modeling and b), d) measurement from impedance analyzer.

3.4.3 Acoustic characterization

The peak negative pressure of the 6.5 MHz element was recorded with different excitation voltages. Measurements were recorded at the contrast imaging area in order to verify that this would be the pressure applied in the region of the microbubbles. As shown in Figure 3.9, the response of the low frequency transducer was nearly linear at excitation voltages lower than 70 V, having an average transmitting sensitivity of 14.5 kPa/V. Nonlinearities showed up when the input was higher than 70 V. At about 100 V, more than 1.2 MPa rarefractional pressure (MI: 0.48) was generated, which was sufficient to produce a high-frequency, broadband response from microbubbles imaged in tissue in prior studies [127, 149].

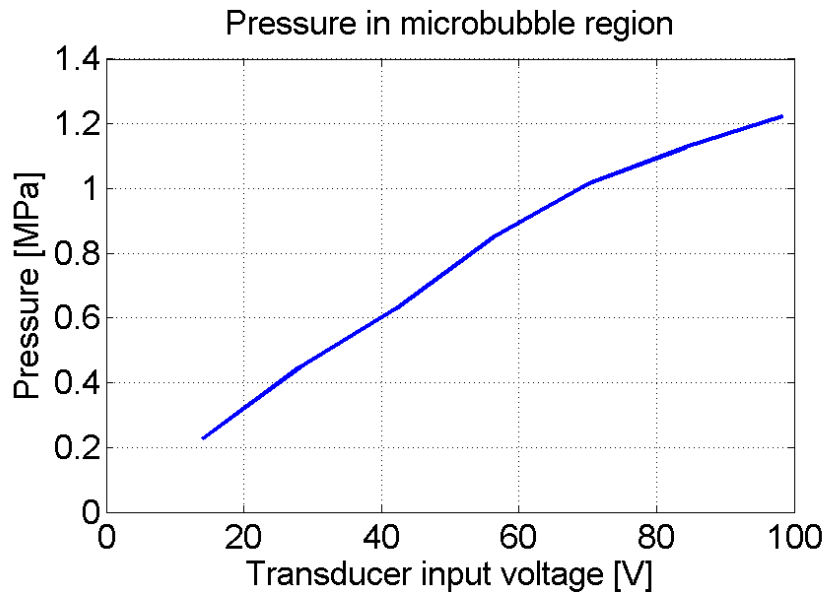


Figure 3.9 Peak rarefractional pressure at the contrast imaging area, 3 mm away from the center of the transducer, using a 5-cycle burst excitation on the low frequency (6.5 MHz) element at varied voltages.

Beam profiles of the transmitter were scanned with the hydrophone (HNA-0400, Onda Co., Sunnyvale, California, USA) and motion stage controlled by LabVIEW (National Instruments Co., Austin, Texas, USA). With the stacked layers design with different transmitter/receiver apertures, the output pressure (Figure 3.10) at the center of the beam ($x = -1, y = 0$) was almost as high as that at the side ($x = -2$ to $x = 1, y = 0$). The high pressure beam covers the center region of the transducer so that super-harmonic signal could be detected by the receiver.

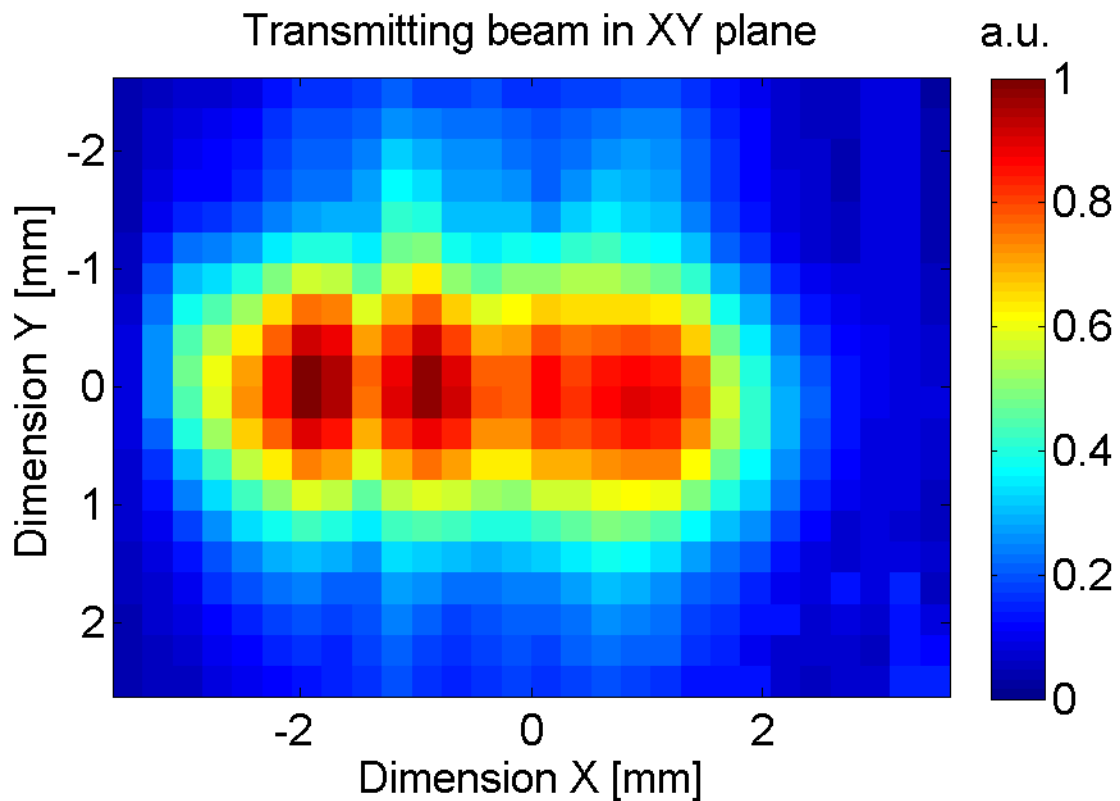


Figure 3.10 Bema profile of the transmitter with strong pressure at the middle.

Pulse-echo experiments illustrated the broad bandwidth of the receiving element (Figure 3.11 b). The pulse length of the echo signal was about 119 ns (at -20 dB for the envelope), corresponding to an spatial axial length of 89 μm in tissue, which means that the high frequency transducer can be used in pulse-echo mode for high resolution fundamental imaging. The -6 dB fractional bandwidth of the receiving element was measured to be 46%, covering a frequency span of 22.9 – 36.6 MHz, providing good reception of the high-frequency, broadband (4th to 7th order harmonics) microbubble response. Because of the anti-matching layer, the high frequency element behaves as if there was little backing for it. As such, the bandwidth predicted by the modeling result was broad (Figure 3.11 a) and is seen in the measured bandwidth (Figure 3.11 b). According the measurement result, the loop sensitivity of the high frequency receiving element is -27 dB.

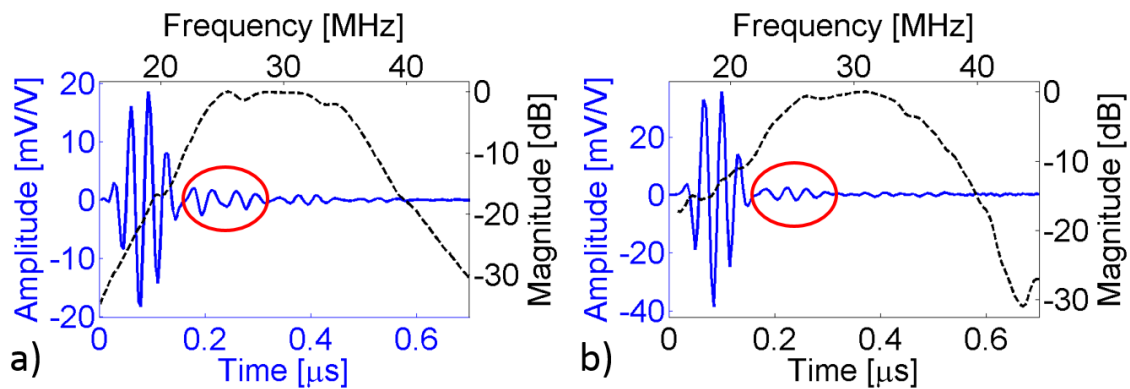


Figure 3.11 Pulse-echo response and its FFT spectrum of 30 MHz element in a) modeling and b) measurement. The aliasing echoes are marked by the red ellipses.

The transmit frequency spectrum was measured by hydrophone using a 2-cycle burst excitation, and the receive bandwidth was measured from the pulse-echo experiment driven with a 1 μ J impulse. The -20 dB frequency response of the transmit element was 4.0 – 8.9 MHz. The frequency response of the transmitting and receiving elements were well separated (5.6 MHz stop band at -20 dB) (Figure 3.12), which is ideal for detecting microbubble broadband frequency content and achieving high contrast to tissue ratios.

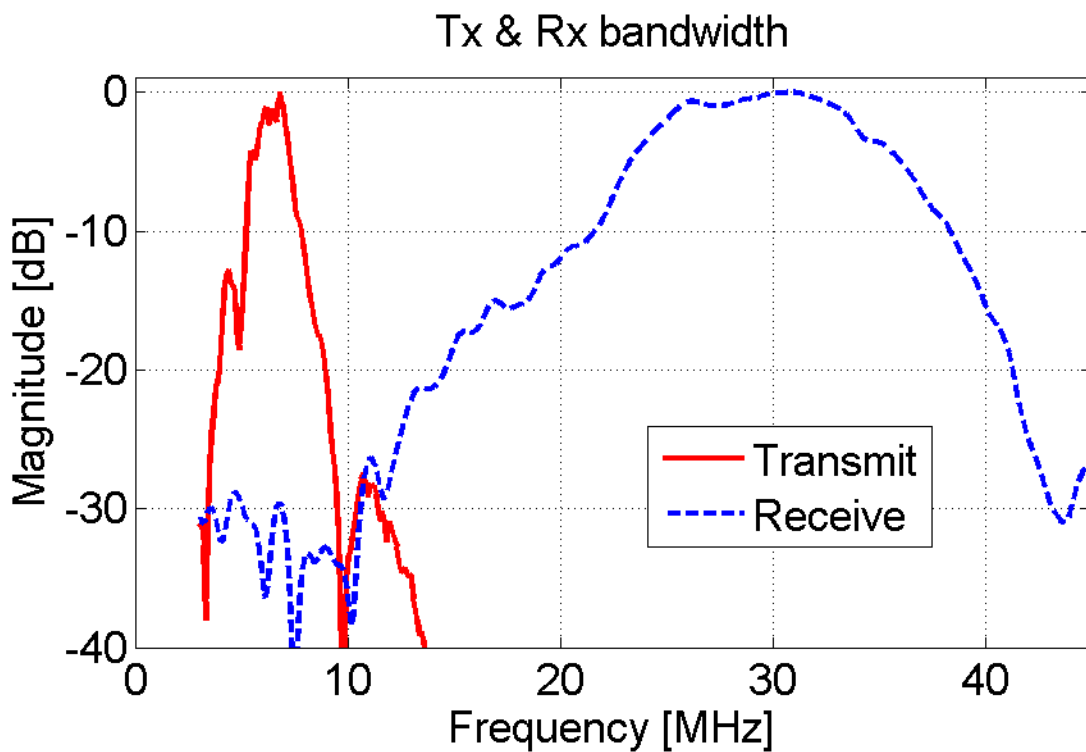


Figure 3.12 Transmission (2-cycle burst) and receiving (pulse-echo) bandwidth separation.

3.4.4 Microbubble response

Microbubble response was clearly detected with the dual frequency transducer. In the time domain amplitude analysis, a root-mean-square (RMS) value through the 100 lines of data was taken as the amplitude of the microbubble response. The received data was first high pass filtered at 10 MHz to thoroughly remove residual tissue/phantom responses at the fundamental or low harmonic frequencies. Residual stationary signals from the tube wall were filtered using a clutter filter, leaving only the transient high frequency signal from microbubbles. RMS values of the microbubble response with different excitations were shown in Figure 3.13. As shown in the figure, the background noise was about 0.5 mV, the source of which primarily comes from the noise of the amplifier. With 1-cycle burst excitation, the peak negative pressure was low ($PNP < 0.65$ MPa) at all voltage inputs (14 V – 98 V), resulting in low (6 dB) SNR (Figure 3.13 a). With 2 or more cycles in each burst, microbubble response could be more than 1.5 mV at 70 V excitation ($PNP \geq 0.8$ MPa), and the SNR was larger than 10 dB (Figure 3.13 b and c). Because of the small Q-factor of the receiving element, each negative peak of the transmission wave was clearly discernible temporally (Figure 3.13 c). At 2 or more cycles in each burst, 42 V input excitation was high enough to excite the nonlinear microbubble response (however, at a low SNR of 4 dB), corresponding to a rarefractional pressure of 0.65 MPa. The microbubble response was just slightly higher at 98 V input compared to 70 V input, and we hypothesize that increasing the pressure too high may decrease the CTR due to relatively high nonlinear response in tissue. No signal was detected at low level voltage excitation (14 V) and the response was always within the noise. In summary, the SNR increased rapidly with

increasing driving voltage and then leveled off (e.g. < 70 V). If the input voltage was higher than 70 V, the signal increase of the microbubble response was less significant. Gessner et al also observed a similar plateau for nonlinear microbubble response as a function of pressure when excited at 2 MHz [150]. The excitation voltage may be further optimized for *in vivo* conditions.

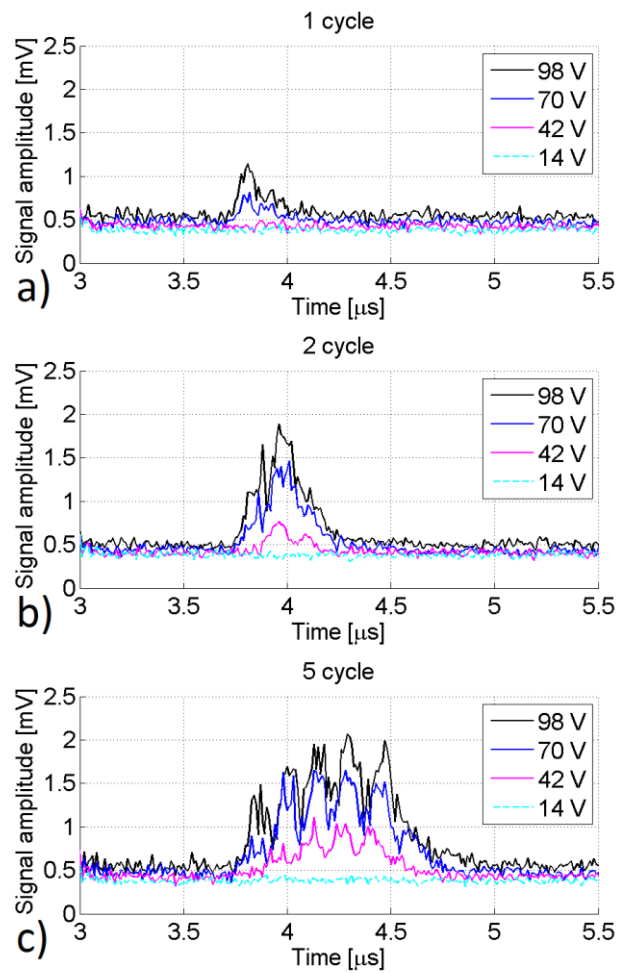


Figure 3.13 Amplitude of nonlinear microbubble response with sinusoidal bursts of a) 1-cycle, b) 2-cycle and c) 5-cycles at different voltage excitations.

The spectra of the received signals were analyzed to investigate the microbubble response in frequency space. Spectra of all the 100 measurements were calculated using the short-time Fourier transform and the spectrum for a given test condition was analyzed. As shown in Figure 3.14, frequencies lower than 20 MHz were intrinsically suppressed by the transducer's receiving sensitivity so low frequency harmonics of the fundamental do not greatly contribute to the image formation in dual frequency imaging. Input voltage was kept at 70 V while number of cycles in the burst varied (Figure 3.14). Fewer number of cycles produced higher axial resolution, however, a 1-cycle burst suffered from low SNR because the peak negative pressure was too low to induce sufficient microbubble harmonics. With a 2-cycle burst at 70 V input, microbubble response was detected while minimizing loss of axial resolution (about 200 μm). The frequency content of the noise was less than -12 dB relative to the peak frequency content of the microbubble signal (Figure 3.14 b).

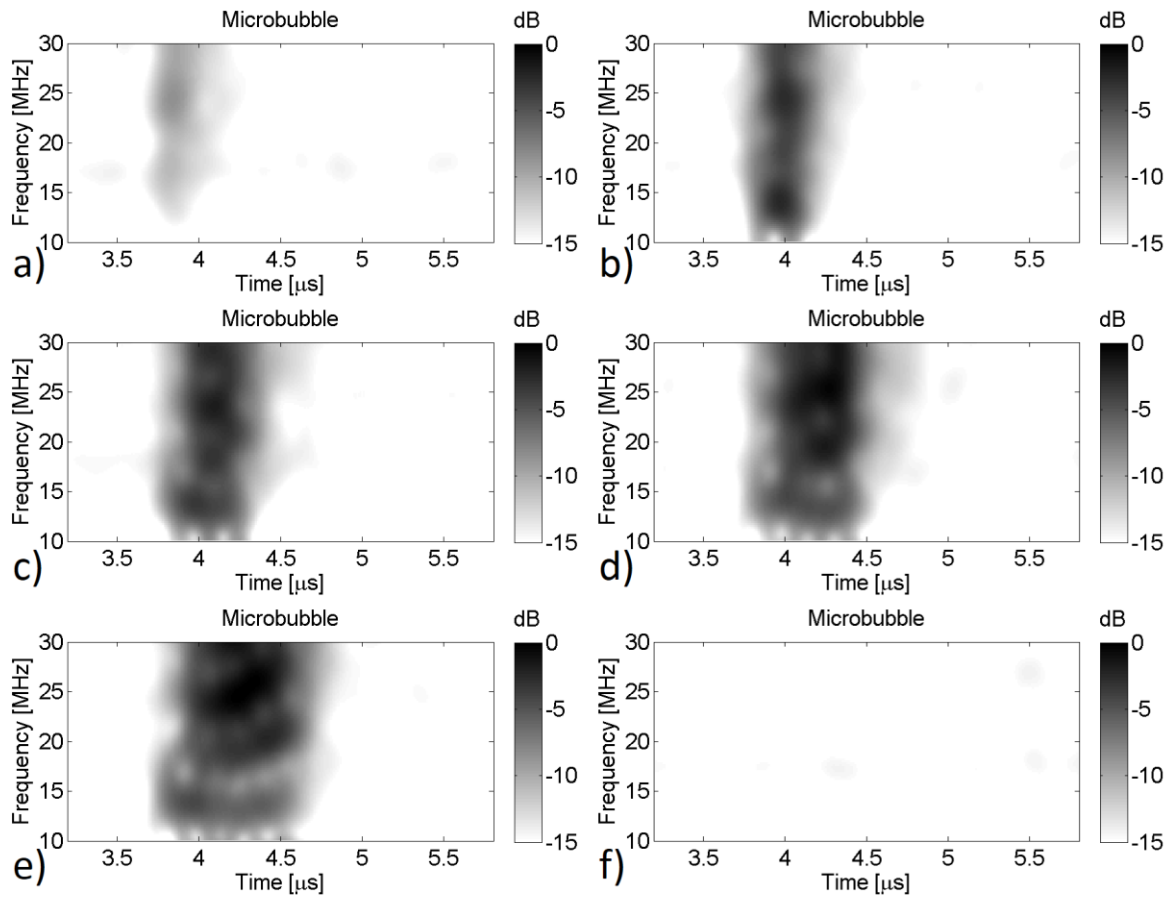


Figure 3.14 Spectrum of microbubble responses at 70 V with a burst of a) 1-cycle, b) 2-cycles, c) 3-cycles, d) 4-cycles, e) 5-cycles. The spectrum of a water filled tube at 70 V with a burst of f) 5-cycles shown for comparison.

The presence of the microbubble signal was verified by rinsing the tube with pure water. The high frequency response observed when imaging microbubbles vanished instantly when the microbubbles were cleared (Figure 3.14 f).

3.4.5 Fundamental imaging

Fundamental imaging mode was performed using the 30 MHz element in pulse-echo mode. An impulse with 1 μJ energy was used to produce acoustic waves and the reflected signal was recorded by a LabVIEW data acquisition system at 100 MHz sampling rate. The envelope was detected and the magnitude was scan converted to polar system as shown in Figure 3.15. In fundamental imaging mode, the reflection from the 0.6 mm steel rod was nearly 20 dB stronger than that from the 200 micron tube containing microbubbles.

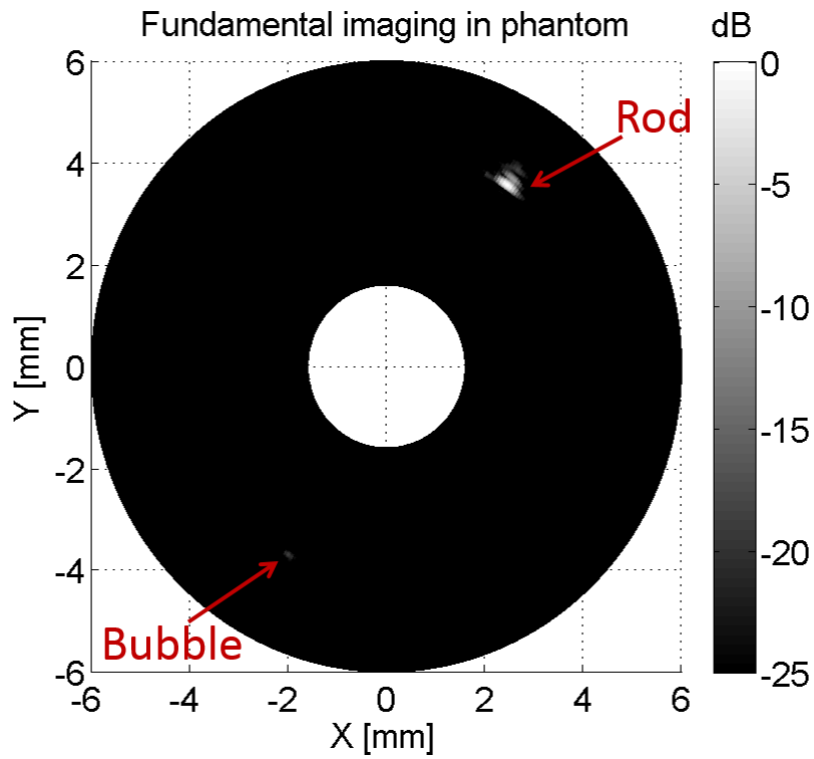


Figure 3.15 Fundamental imaging at 30 MHz.

3.4.6 Super-harmonic imaging

In the super-harmonic imaging mode, microbubbles were excited using the low frequency element and backscatter was received using the 30 MHz element. The transmission input was a 6.5 MHz 2-cycle sinusoidal burst at 84 V. The received signal was high pass filtered at 10 MHz before being digitized.

The data was filtered digitally and reconstructed to create an image offline in MATLAB. First, each line in the scan was band pass filtered with a 60th order finite impulse response filter with corner frequencies of 25 and 35 MHz, which is also the sensitivity range of the transducer. The frequency content in this bandwidth covers the majority of the 4th and 5th harmonics of the transmission frequency. After filtering, the wave package was detected from the signal and the magnitude was scan converted to polar coordinate as shown in Figure 3.16.

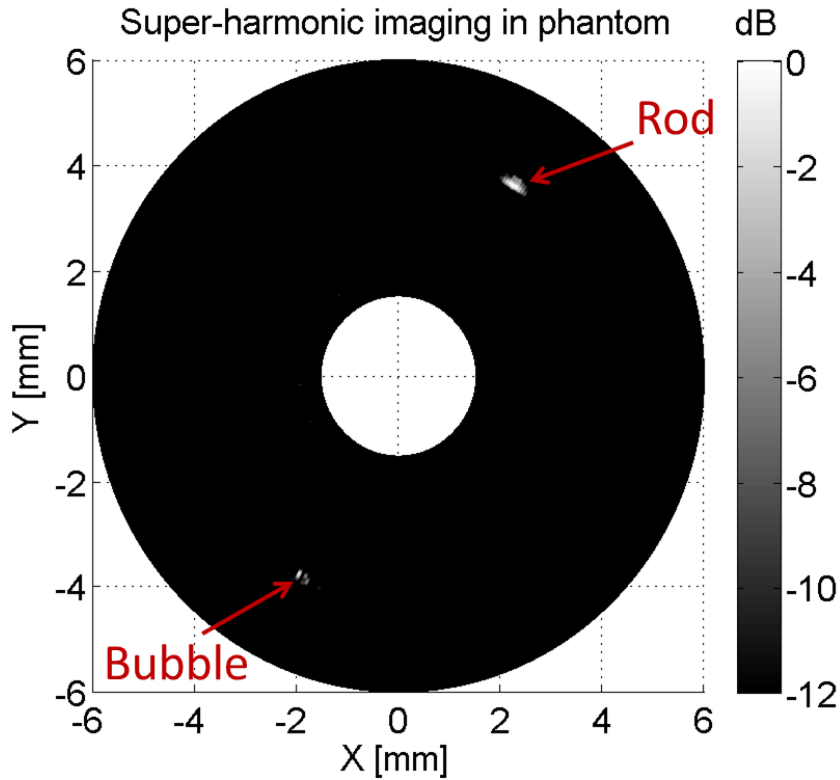


Figure 3.16 Super-harmonic imaging of the microbubble tube and a steel rod.

The microbubble filled tube was clearly detected with a CTR of 12 dB. There was some nonlinear response on the rod signified by its presence in the image even after filtering, but the signal magnitude was strongly decreased in comparison to the fundamental mode image. In dual frequency imaging, the microbubble response was almost the same magnitude as the reflection from the steel rod. Both axial and lateral resolutions were high enough to clearly resolve the 200 μm microbubble tube. The diameter of the steel rod can also be clearly visualized to be 0.6 mm in lateral direction but not easily seen in the axial direction. Because the sound speed in steel is about 4 times of that in water, the reflection from the back surface

of the steel rod seems very close to the reflection from the front surface, introducing a high distortion in the axial resolution on the rod.

3.5 Performance optimization

3.5.1 Optimization approaches

Low frequency transmitter is subjected to the main limitation of the performance and has more room for the performance optimization. First, as shown in previous research [135], imaging with reasonably higher order of harmonics tended to generate higher CTR. However, the receiving frequency is the major limitation of the penetration depth, which could not be increased without sacrificing the penetration depth. The way to increase the CTR would be realized by decreasing the transmitting frequency [151]. Second, for this dual frequency super-harmonic imaging transducer, the wavelength of the low frequency wave is several (4 – 6) times longer than the high frequency wave. As a result, decreasing the pulse length of the low frequency element is much more efficient to increase the axial resolution. Based on these consideration, the first step of performance optimization was focused on the transmitting frequency and the pulse length of the low frequency transmitters. Of course, the high frequency sensitivity and pulse length are also important features of the dual frequency transducers. These minor optimizations are left for future work on this project.

First, the frequency of the transmitter was decreased from 6.5 MHz to 5 MHz. Because the transmitter was much larger than the receiver, the intravascular environment dominantly limited the transmitter. As a result, the aperture size of the transducer remained constant as

when decreasing the transmitter frequency. In this case, the width-to-thickness ratio would be less than 2 in the 5 MHz transmitter, so that the lateral mode would be coupled in the thickness mode vibration, leading to a decreased pressure output. The lateral mode vibration could be suppressed by microstructures like 1-3 composites. So in this frequency optimization, constant pressure was used to compare the CTR between 5 MHz and 6.5 MHz transmitters.

Second, pulse length was decreased by replacing the PMN-PT single crystal by PMN-PT 1-3 composite. As an imaging transducer, a short pulse length is preferable, which determines the axial imaging resolution. PMN-PT 1-3 composite possesses high coupling factor (k_t is close to $k_{33} \sim 0.9$) and relatively low acoustic impedance ($\sim 18 \text{ MRayl}$), which is preferred for a short impulse response and high resolution imaging. However, the pressure output efficiency of PMN-PT 1-3 composite is affected by two controversial effects: the ultrasonic wave generation and propagation efficiencies. Low fraction ($\sim 50\%$) of active material leads to low wave generation efficiency while low impedance of the composite materials causes high wave propagation efficiency. As stated above, the lateral mode could be suppressed in the 1-3 composite. The resonant frequency of these 1-3 composite transmitters was 5 MHz.

Fabrication and characterization process of these 5 MHz transmitter transducers were very similar to that of the 6.5 MHz transmitter transducers. These transducers were characterized to obtain the transmitting pressure output and the contrast imaging result. In the imaging, the setup (Figure 3.17) was similar to that in the preliminary experiment, except that the steel rod

was not included because the receiver was designed to be identical and it was not necessary to compare the B-mode imaging.

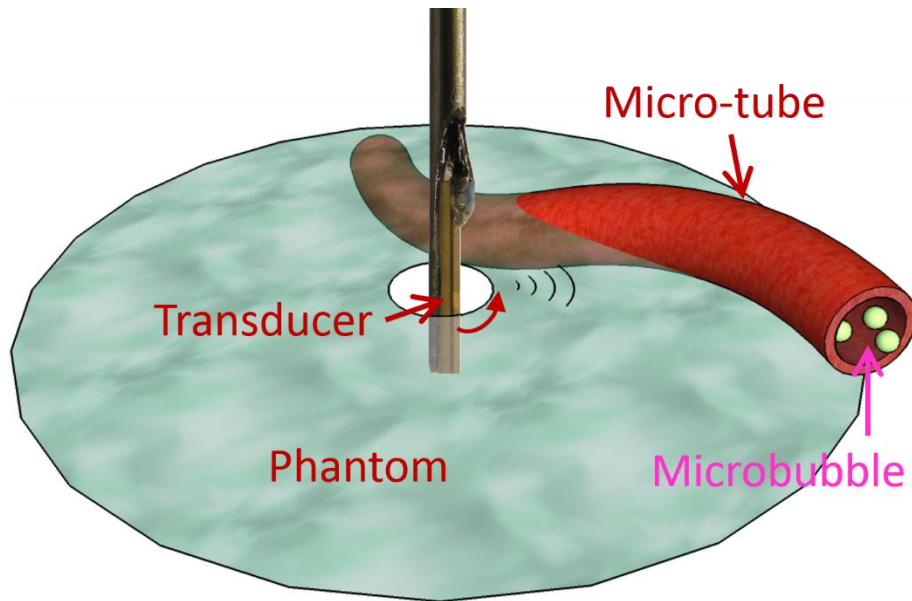


Figure 3.17 Setup of vasa vasorum imaging in vitro. Phantom was used to mimic the coronary vessel wall and an acoustically transparent micro-tube was used to mimic the vasa vasorum.

3.5.2 Transmission output

Transmission characteristics of the transducers were verified by hydrophone with one- or two-cycle bursts excitations. Pressure measurement results were normalized to unit voltage (1 V) applied on the samples, which are shown in Figure 3.18.

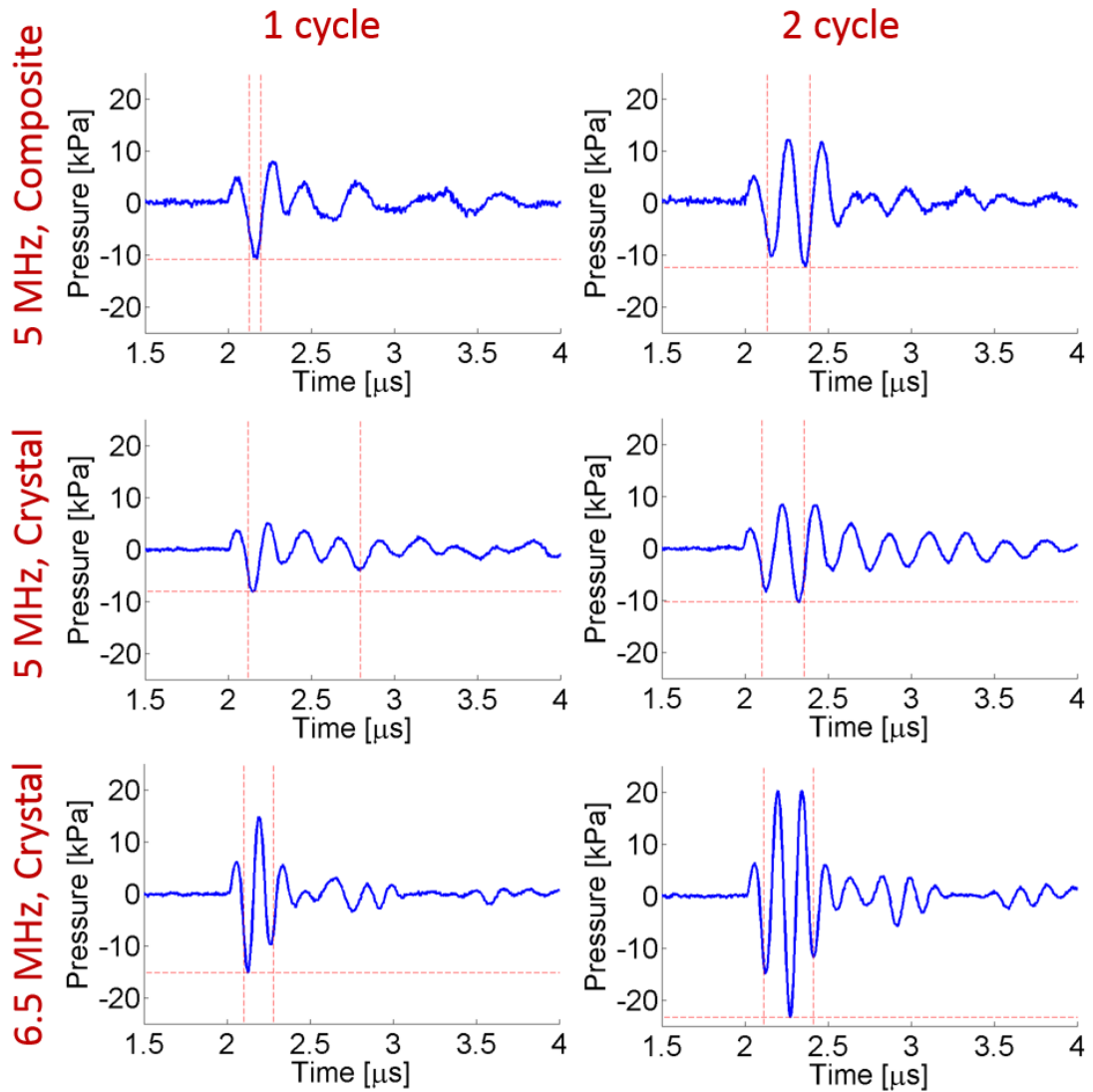


Figure 3.18 Transmission sensitivity of the prototype transducers with the transducers shown at the left and the excitations shown at the top. All the values are normalized to unit voltage as kPa/V.

Normalized pressure value of each transducer in each test condition is marked by the dash horizontal line in Figure 3.18. Because the width-to-thickness ratio (W/T) of the 5 MHz single crystal material is lower than 2 (0.6 mm over 0.39 mm), it vibrated in a coupled mode and

hence the pressure output is relatively low. The 6.5 MHz transducer, with W/T of 2 (0.6 mm over 0.3 mm), vibrated mainly in the thickness mode [152] and generated the highest pressure in these three groups. The 5 MHz 1-3 composite transducer is also mainly in the thickness mode because lateral mode is highly suppressed by the periodic structure within this frequency range. However, the pressure of the 5 MHz 1-3 composite transducer was still relatively low compared to the 6.5 MHz single crystal transducer, mainly due to the low volume ratio of active material. As a result, pressure output of the 6.5 MHz single crystal transducers is the highest among the groups.

Relatively high acoustic pressures induced detectable super-harmonics from microbubbles while low pressures did not. As a result, the pulse length (marked as vertical dashed line in Figure 3.18) was defined as real-time signal with -6 dB negative pressure value. Because of mode coupling, very long pulse showed up from the 5 MHz single crystal transducers when driven by a broadband, 1-cycle excitation. Such low frequency components were insignificant when excited by a 2-cycle burst. On the contrary, the 5 MHz 1-3 composite transducer, with little low frequency components coupled, generated clean 5 MHz ultrasound wave at both 1-cycle and 2-cycle excitations. Because of the relatively low impedance of the 1-3 composite material, a very short pulse (1 peak) was achieved with the 1-cycle excitation. With an aspect ratio of 2, the 6.5 MHz single crystal transducers had almost no low frequency components either, which vibrate in the 6.5 MHz thickness mode dominantly. However, the pulse length of this group of transducers was still long because of the high acoustic impedance mismatch

(2 peaks in 1-cycle excitation and 3 peaks in 2-cycle). Therefore, according to the pulse length in the pressure output, the 5 MHz 1-3 composite transducers were preferable.

The tradeoff between the high pressure from the 6.5 MHz crystal transducers and the short pulse from the 5 MHz composite transducers may be determined for imaging. First, with 1-cycle excitation, the pressure output from the composite material was about 70% of the 6.5 MHz crystal, which was not dramatically low. Within 100 V excitation, the composite could generate about 1 MPa pressure, which was sufficient for the contrast super-harmonic imaging. Second, a short pulse length (single negative peak) is highly desirable for a high resolution imaging, which is, however, hardly achievable by the 6.5 MHz single crystal transmitter. Taking the two considerations into account, the 5 MHz composite transmission transducers were believed to be suitable for a high contrast, high resolution imaging.

3.5.3 Imaging results

Transmitter frequency comparison

Contrast imaging using the prototyped transducers were validated and compared for their CTR and resolution. The comparison of CTR was made between the two frequencies with 2-cycle excitations. With the similar PNP (~ 1 MPa), the 5 MHz transducer generated higher CTR (23 dB, Figure 3.19 b) image than the 6.5 MHz transducer (15 dB, Figure 3.19 a). There are three possible reasons behind this phenomenon. The primary reason is that the high order harmonics from tissue are much lower than that from microbubbles. The second reason is that lower frequency ultrasonic wave relates to higher mechanical index (MI) that would induce

more significant nonlinear vibrations on microbubbles. Another possible reason is that the 5 MHz ultrasound is closer to microbubble resonance (< 4 MHz) [153] than the 6.5 MHz one, so that the 5 MHz ultrasound is likely to induce stronger vibration on the microbubbles. Because of these reasons, the 5 MHz transmitter is more effective than 6.5 MHz one in superharmonic contrast imaging for a 30 MHz receiver.

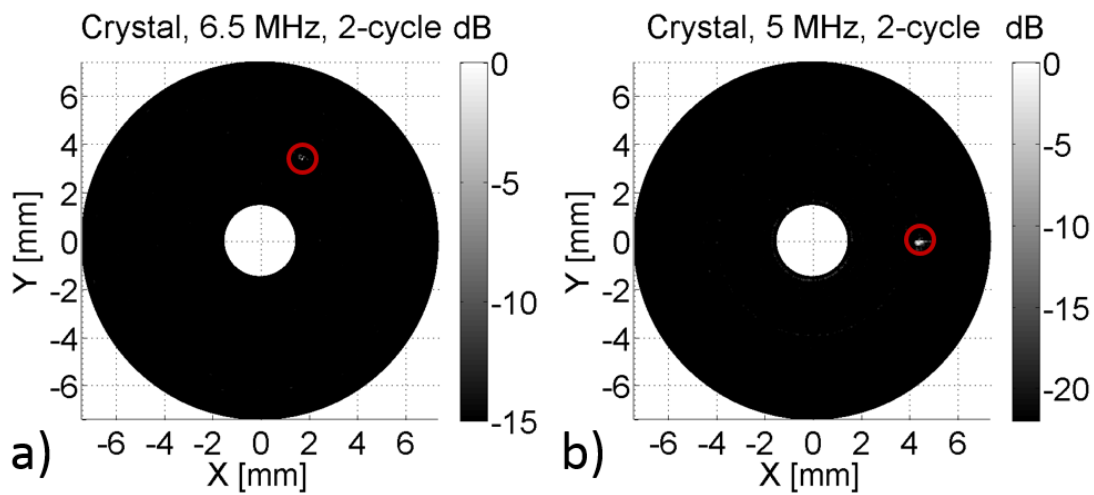


Figure 3.19 Comparison of contrast imaging with the a) 6.5 MHz and b) 5 MHz transmitters, both of which were made of PMN-PT single crystals are excited by 2-cycle bursts.

Transmitter material comparison

With 2-cycle excitations, the pulse lengths of the contrast signals were long (Figure 3.19). Pulse length of the 6.5 MHz single crystal transmitter was ~ 200 μm because of multiple negative peaks existed in the transmission. The 5 MHz single crystal ultrasound has longer

pulse length than the 6.5 MHz one because of longer wavelength and more cycles of reverberation due to lateral mode coupling. As a result, the 5 MHz single crystal transducer generated the lowest resolution imaging among the three groups.

Fewer number of cycles (1-cycle) excitation generated shorter pulse length with a compromise on the CTR. However, because of intrinsic limitation of the single crystal material, the two peaks in the negative pressure generated by the 6.5 MHz transmitter with 1-cycle excitation (Figure 3.18) resulted in the resolution of $> 150 \mu\text{m}$ (Figure 3.20 a). In comparison, the 1-3 composite transmission transducer under 1-cycle excitation generated very short pulse (single peak). The image generated with the 5 MHz 1-3 composite transmitter with 1-cycle excitation is shown in Figure 3.20 b). The $200 \mu\text{m}$ tube was clearly detected with a CTR of 12 dB. Pulse length of each bubble response is equivalent to a $70 \mu\text{m}$ spatial distance, indicating an axial resolving capability of $70 \mu\text{m}$. It's worthy being pointed out that in these contrast imaging, the micro-tube was randomly distributed in the phantom with arbitrarily angle relative to the transducer orientation. As a result, the lateral dimension of the imaging results did not indicate the lateral resolution.

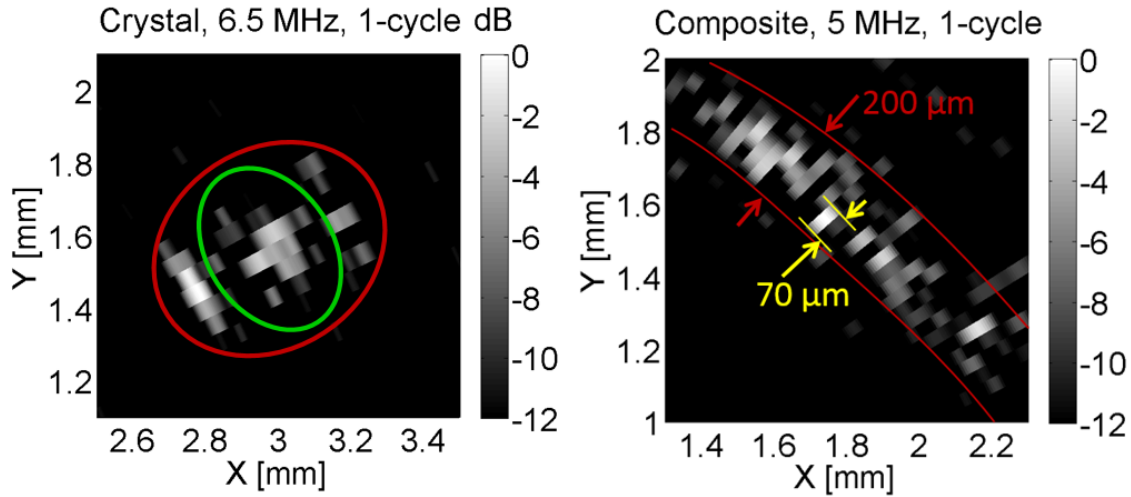


Figure 3.20 Comparison of contrast imaging with the 5 MHz transmitters made of PMN-PT single crystal and PMN-PT 1-3 composite. Both were excited by 1-cycle burst.

3.6 Summary

In this research, a dual frequency IVUS transducer was designed, fabricated and characterized, and its contrast imaging and fundamental imaging capability were evaluated. The measured transducer performance matched the modeling results very well for both transmission and receiving components.

In the transducer design, two key features were proposed. First, the aperture of the receiving element was significantly smaller than the transmission element, which yields both mechanical and electrical benefits. In mechanics, the large aperture transmitter delivered more acoustic excitation energy, while the small aperture of the receiver reduced the distance of the near-field within 1.5 mm so that the valid imaging depth could as close as 1.5 mm. In electrical

consideration, the capacitance per unit area of the low frequency element is lower than that of the high frequency element due to larger thickness, the different apertures made electrical impedance the two elements closer to 50Ω to match the input/output impedance of commercial machines. Second, the acoustic filter layer placed intermediately between the two active layers enabled the low frequency transmit wave to pass through, but the high frequency receive wave to be reflected which aided in decoupling signal content. Thickness of the anti-matching layer was controlled by mixing a 1% microsphere (10 μm diameter) solution into the silver epoxy. The addition of the microspheres had little effect on the acoustic or electrical properties of the silver epoxy. Finally, a layer of parylene coating acted both as shielding and as the matching layer of the high frequency receiver. Such design and fabrication processes were demonstrated successful in prototyping dual frequency transducers for both fundamental mode imaging and contrast specific imaging.

The feasibility of ultra-broadband contrast enhanced intravascular ultrasound imaging was evaluated *in vitro*, using a prototype of dual frequency small aperture transducer (T6.5/R30). Peak negative pressures higher than 1.2 MPa were generated at 3 mm away axially from the low frequency element (0.6 x 3 mm) of the transducer, which was proved to be sufficient for contrast imaging. Sensitivity of the receiving element (0.6 x 0.5 mm) provided the capability of detecting the broadband high-frequency response of microbubbles. Initial imaging of a 200 μm tube filled with microbubbles showed reasonably high SNR (> 12 dB). The small aperture dual frequency transducer design presented demonstrates the first of its kind for contrast enhanced high-frequency ultra-broadband intravascular imaging.

Both fundamental mode and dual frequency super-harmonic imaging were tested *in vitro* using a tissue mimicking gelatin based phantom. The 30 MHz pulse-echo fundamental imaging showed a very high SNR (>25 dB) with a reasonable resolution (200 μm). While microbubble backscatter was very weak in the fundamental mode, dual frequency super-harmonic imaging generated reasonable CTR (12 dB) and good resolution (200 μm) in resolving the microbubble filled tube. The steel rod used in the experiments was an extremely exaggerated target with a reflection coefficient of 0.94 in water, thus the strength of the echo was large enough such that weak high frequency components of transmission were detectable. Due to the viscoelastic behavior of tissue, we would not expect to detect tissue harmonics in the high-frequency bandwidth at the transmission acoustic pressure levels ($\text{MI} < 0.48$ at 6.5 MHz) used in these experiments. Contrast agent detection in high fidelity is necessary for microbubble imaging strategies involved with both molecular imaging and vasa vasorum localization. Small aperture transducers with high CTR and high resolution capable of detecting contrast agents would promote the transition of advanced contrast imaging methods to intravascular ultrasound applications.

With the concept of the dual frequency transducer design demonstrated by the preliminary results (6.5 MHz single crystal transmitter), further optimization of the performance were elucidated. With similar peak negative pressure, the 5 MHz transducers generated higher CTR (23 dB) imaging results than that with the 6.5 MHz transmitter (15 dB). However, it is not preferable to simply reduce the transmission frequency by increasing the thickness of the PMN-PT single crystals because of vibration modes coupling. Replacing the single crystal

material by the 1-3 composite, the low frequency components disappeared, and a short pulse with single negative pressure peak was generated. With 1-cycle excitation, the 5 MHz 1-3 composite transducers showed reasonable CTR (12 dB) and very short pulse length (70 μm). Such high resolution indicated the ability of detecting the second order vasa vasorum ($67.99 \pm 2.72 \mu\text{m}$) [138].

In conclusion, the dual frequency intravascular transducers developed in this research demonstrated their capability of intravascular acoustic angiography, indicating a promising future for effective evaluation of the plaque vulnerability and diagnosis of atherosclerosis cardiovascular diseases.

Chapter 4.

Acoustic Filter Layer Design with Microwave Analysis

If the dual frequency transducer was designed with stacked layers as illustrated in Chapter 3, then one major concern would be the acoustic interference between the two elements. Such an interference might be taken as advantages or disadvantages. Unfortunately, if the two active layers were bonded together directly, then the interference between the two would be disadvantages for the dual frequency intravascular ultrasound transducer. An acoustic filter (AF) design was then applied to the structure, sandwiching an intermediate layer between the low frequency and the high frequency active elements, to solve the problem in this dual frequency transducer structure. For the high frequency receiving wave, the acoustic filter acted as an anti-matching layer, reflecting most high frequency incoming energy of the wave due to impedance mismatch between the high frequency active layer and the anti-matching layer. For the low frequency transmitting wave, the same acoustic filter acted as a passive amplifier that enhances the low frequency wave propagation. The anti-matching layer and passive amplifier can be achieved with the same acoustic filter layer that performs differently for different waves. In this chapter, the microwave equivalence methods needed for the acoustic filter are first introduced, and then the anti-matching and passive amplification effects of the acoustic filter are discussed separately.

4.1 Microwave analysis of piezoelectric transducers

4.1.1 Electrical-mechanical equivalence

Both microwave and mechanical wave share the same wave propagation properties although they are in different field. Equation (1.24) applies for the propagating wave in both domains and Equation (1.27) applies for the standing wave for both as well. Reflection and refraction properties are also the same for both types of waves. Consequently, the two waves could be studied together and the theories and methods could be shared [154].

Mass-spring-damper model in mechanical vibration is equivalent to the lumped element RLC (resistor-inductor-capacitor) circuit in electrical vibration (Figure 1.5). Equivalences of the parameters are shown in Equation (1.16). Lumped element analysis is usually used for conceptual design of transducers, but is not widely used for detailed parameters of the transducers.

Continuous variations of strain and stress are the principal features of piezoelectric transducers, which is typically equivalent to distributed circuit like transmission line for electromechanical wave. Electromechanical wave equations are

$$\left(\nabla^2 - \frac{1}{c^2} \frac{\partial^2}{\partial t^2} \right) E = 0 , \quad (4.1)$$

$$\left(\nabla^2 - \frac{1}{c^2} \frac{\partial^2}{\partial t^2} \right) B = 0 , \quad (4.2)$$

where E and B are the electric field and magnetic field, respectively, and c is the wave speed in the medium defined as $c = 1/\sqrt{\mu\varepsilon}$ (μ and ε are the magnetic permeability and dielectric constant in the medium.). Such wave equations are mathematically identical to mechanical wave (1.22) if they are in the same dimension. Electromagnetic wave reflection coefficient shown in (1.48) is also identical as mechanical wave shown in (1.36). As a result, the cascade transmission line theories could be applied to the ultrasound wave propagation in multiple layers.

A typical multi-layer wave propagation problem is a thin intermediate layer placed between two infinitely large media (Figure 4.1 a), and the equivalent circuit is a short section of transmission line connecting two infinitely long lines (Figure 4.1 b). If Z_{01} and Z_{03} are long, then $Z_1 = Z_{01}$ and $Z_3 = Z_{03}$. Neglecting the loss, the input impedance Z_{in} is calculated from (1.47)

$$Z_{in} = Z_{02} \frac{Z_{03} + jZ_{02} \tan kl}{Z_{02} + jZ_{03} \tan kl}, \quad (4.3)$$

where k is the wave number in Z_{02} which equals to β if there is no loss, and l is the length of Z_{02} . From Equation (1.48), the reflection coefficient is

$$\begin{aligned}
\Gamma &= \frac{Z_{in} - Z_{01}^*}{Z_{in} + Z_{01}^*} \\
&= \frac{Z_{02}(Z_{03} - Z_{01}) + j(Z_{02}^2 - Z_{01}Z_{03}) \tan kl}{Z_{02}(Z_{03} + Z_{01}) + j(Z_{02}^2 + Z_{01}Z_{03}) \tan kl} \quad , \\
&= \frac{\sqrt{Z_{02}^2(Z_{03} - Z_{01})^2 + (Z_{02}^2 - Z_{01}Z_{03})^2 \tan^2 kl}}{\sqrt{Z_{02}^2(Z_{03} + Z_{01})^2 + (Z_{02}^2 + Z_{01}Z_{03})^2 \tan^2 kl}} e^{j(\phi_1 - \phi_2)}
\end{aligned} \tag{4.4}$$

where ϕ_1 and ϕ_2 are the phase angle of the numerator and denominator of Γ . Transmission coefficient T (amplitude) through the intermediate transmission line is

$$\begin{aligned}
T^2 &= 1 - |\Gamma|^2 \\
&= \frac{4Z_{01}Z_{03}}{(Z_{01} + Z_{03})^2 \cos^2 kl + \left(Z_{02} + \frac{Z_{01}Z_{03}}{Z_{02}}\right)^2 \sin^2 kl} \quad ,
\end{aligned} \tag{4.5}$$

which is mathematically identical to the acoustic transmission coefficient (intensity) through an intermediate layer [155]

$$T_I = \frac{4}{2 + (Z_{03}/Z_{01} + Z_{01}/Z_{03}) \cos^2 kl + (Z_{02}^2/Z_{01}Z_{03} + Z_{01}Z_{03}/Z_{02}^2) \sin^2 kl} \quad . \tag{4.6}$$

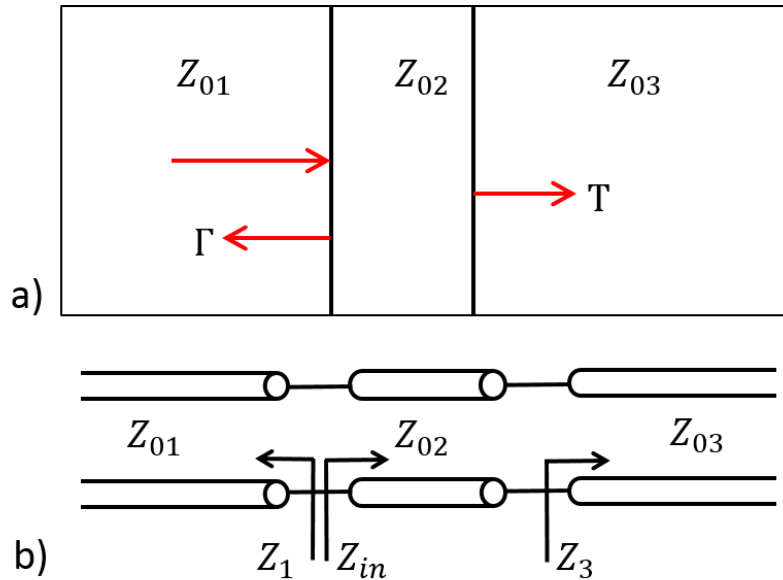


Figure 4.1 Schematic diagram of transmission and reflection in a 3-layer structure.

For a multi-layer vibration system, the cascade calculation from microwave (Section 1.4.1) provides a simple and detailed method to estimate the input impedance and reflection coefficient. If the loss of the multi-layer system is negligible, then the transmission coefficient could be calculated from Equation (1.49). If the loss of the system needs to be taken into account, then there is no analytical calculation of the transmission coefficient, in which case, a software simulation (AWR Microwave Office, AWR corp., EI Segundo, CA) could be used instead.

4.1.2 Quarter wavelength impedance inverter

Quarter wavelength layer in ultrasound system also acts as an impedance inverter as the transmission lines with Equation (1.53). Characteristic acoustic impedances of materials are

real values, so that the impedance inverter transforms one real impedance to another. Such impedance inverter could be applied for different purposes, either making the impedance better matched or mismatched. A brief introduction of the matching layer and anti-matching layer is presented with the quarter wavelength inverter. Detailed design and applications anti-matching layer will be discussed in the next sections.

Matching layer

A matching layer shifts the mismatched impedance to a matched impedance. In ultrasound transducer design, the matching layer applies the same concept of Equation (1.53). In a Smith chart, the matching procedure is to shorten the phasor of the reflection coefficient from the edge of the Smith chart to the center. A demonstrative example of the matching effect is shown from A to B in Figure 4.2 with normalized impedance $Z_0 = 0.2$ and $Z_L = 0.04$. As the input impedance changes from 0.04 to 1, the reflection coefficient changes from -0.923 to 0, with the minus sign denoting the phase of the reflection. It can be observed that the matching layer can be used to decrease the reflection and to enhance the transmission efficiency.

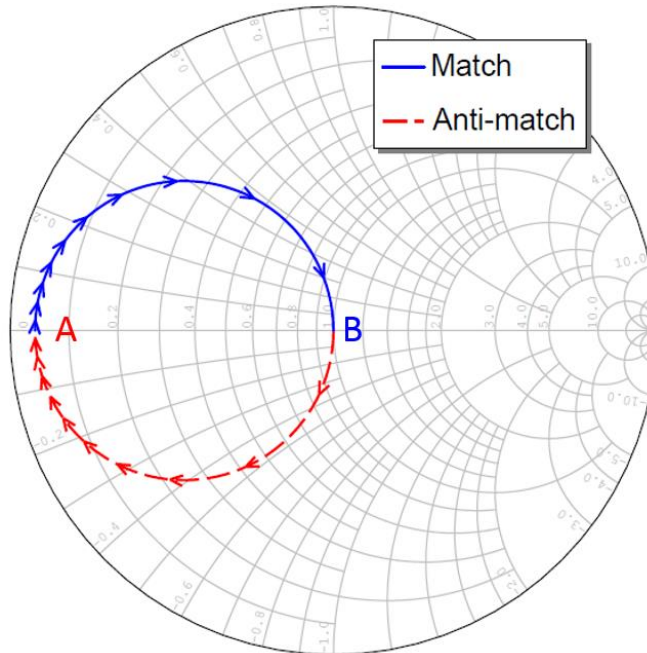


Figure 4.2 Demonstration of matching (blue solid line) and anti-matching (red dash line) effect of the quarter wavelength impedance inverter.

Anti-matching layer

The impedance inverter could be used in the reversed way as well. If a wave propagation is desired to be prohibited, the impedance inverter could be utilized as anti-matching layer, shifting the matched impedance to a mismatch. In the Smith chart, the anti-matching procedure is to elongate the phasor of the reflection coefficient from the center of the chart to the edge. A demonstration of the anti-matching effect is shown from B to A in Figure 4.2 with normalized impedance $Z_0 = 0.2$ and $Z_L = 1$. As the input impedance changes from 1 to 0.04,

the reflection coefficient changes from 0 to -0.923. Anti-matching layer increased the reflection and suppressed the transmission efficiency.

4.2 Anti-matching layer for high frequency receiving wave

4.2.1 Requirement of an anti-matching layer

As mentioned Chapter 3, the acoustic interference or additional echo signal reflected from back side of the dual frequency super-harmonic transducer would cause aliasing in imaging without proper isolation between the two active elements. If the two elements were bonded together (Figure 4.3 a), then the received high frequency ultrasound wave would go through the low frequency element, and be reflected at the back side of the low frequency component, which would excite the high frequency receiving element again and generate extra pulses in the receiving element (Green dash line in Figure 4.3 b). The signal reflected from the back side of the low frequency element is an aliasing that could not be differentiated from real target, leading to imaging artifacts. Hence, the aliasing signal must be removed or suppressed to a level which is significantly lower than the real target signal.

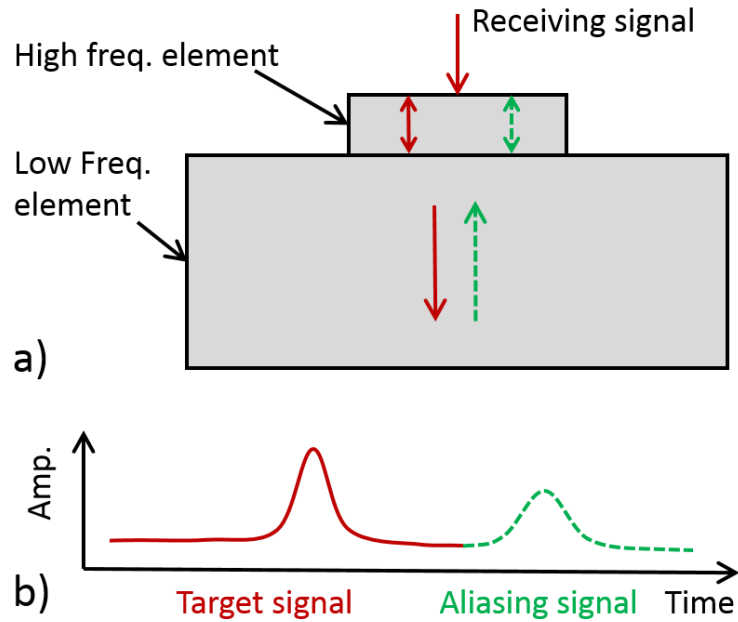


Figure 4.3 Aliasing echo generation. a) Schematic diagram; b) signal detected by the receiver.

Traditional method of removing the aliasing signal was to use high absorptive material to attenuate the signal transmitted backwards, which does not work well in intravascular dual frequency transducer application except that the two frequencies are significantly different ($f_H > 14f_L$, Section 4.3). First, there are barely such high absorptive materials that can eliminate the signal within tens of microns (a couple of wavelengths) according to the space allowed in the transducer. Second, high absorptive material with large thickness attenuates the low frequency transmission ultrasound as well. High attenuation on the low frequency transmission is not acceptable for the non-focused small-aperture transducer, which needs to generate high enough pressure for microbubble nonlinear vibrations. Taking these concerns

into account, the aliasing echo should not be removed using the absorption method if the two frequencies are not significantly (> 10 times) different.

Reflection can be used to suppress the wave propagation backwards by changing the acoustic impedance matching conditions at the boundary. With two active layers bonded together (Figure 4.3 a), the impedance of them are well matched (PZT, PMN-PT ...) or perfectly matched (for same material of the two layers). A lot of energy is transmitted backwards and hence, the aliasing echo showed up (Figure 4.3 b). If an intermediate layer was inserted between the two active layers, then the boundary condition can be changed, which could possibly reflect most of the energy directly without propagating to the low frequency element. Impedance of the intermediate layer should be different from the active layers as much as possible. Low impedance material, with an impedance much lower than piezoelectric materials, was chosen in this application because such materials are much more easily available. With a thickness of a quarter wavelength, the resultant impedance at the interface can be much lower than that of piezoelectric materials, so that most energy is reflected and least energy propagated. The suppression happens again when the tiny back reflected wave is also strongly reflected. As a result, there is very little aliasing echo from back side of the transducer. Such an intermediate layer changes the equivalent impedance at the boundary from well matched to mismatched. As a result, this particular intermediate layer is denominated as anti-matching layer.

4.2.2 Mechanism analysis

The mechanism of the anti-matching layer is rooted in the acoustic wave propagation theory.

The acoustic intensity transmission coefficient T_I is given by

$$T_I = \frac{4Z_H Z_L}{(Z_H + Z_L)^2 \cos^2 kl + (Z_{AM} + \frac{Z_H Z_L}{Z_{AM}})^2 \sin^2 kl} \quad (4.7)$$

where Z_H , Z_L and Z_{AM} are the characteristic acoustic impedance of the high frequency element, the low frequency element and the anti-matching material, respectively; k is the wave number and l is the thickness of the anti-matching layer. Minimum transmission happens when l equals to the quarter wavelength ($\frac{2n+1}{4}\lambda$, $n = 0, 1, 2, \dots$) and the equation reduces to

$$T_I = \frac{4Z_H Z_L Z_{AM}^2}{(Z_{AM}^2 + Z_H Z_L)^2} \quad (4.8)$$

Usually the two active elements are made of the same materials. In that case, the equation is further reduced to

$$T_I = \frac{4Z_H^2 Z_{AM}^2}{(Z_{AM}^2 + Z_L^2)^2} \quad (4.9)$$

This transmission coefficient is very low for a low impedance of anti-matching Z_{AM} . The equivalent impedance Z_e at the interface is

$$Z_e = \frac{Z_{AM}^2}{Z_L} \quad (4.10)$$

This equation indicates that this layer acts as an impedance inverter, which is the same form as that for a matching layer. However, in this case, the high impedance of Z_L resulted in a very low Z_e and, therefore, the very low acoustic intensity transmission coefficient T_I .

Compared to the matching layer design, the mechanism and equations of anti-matching layer design are similar. However, very different values lead to significantly different effects. In matching layer design, the impedance of the medium (or load) Z_L is much lower than Z_H , the active material. With a mediate impedance Z_{AM} , the equivalent impedance is changed to very high value to match Z_H . On the other hand, for anti-matching design, Z_L is very high, which makes the Z_e very low so that impedance is mismatched and wave cannot propagate.

The effect of the matching and anti-matching could also be understood from the boundary conditions (Figure 1.11). For matching layers between a high impedance material and a low impedance material, boundary condition of the matching layer is almost fixed-free, so that resonance occurs with a quarter wavelength thickness. Contrarily for the anti-matching layer, it is almost fixed-fixed boundary condition and no vibration mode exists within a quarter wavelength layer. In other words, the anti-matching layer could hardly vibrate, so that wave could not propagate through this layer.

4.2.3 Microwave analysis

As is briefly shown in Section 4.1, the anti-matching layers could be analyzed as transmission line networks because the mechanical wave and the electromagnetic wave share identical mathematic equations. Specifically, the dual frequency ultrasound transducer (Figure 4.4 a) designed in Chapter 3 could be considered as the equivalent circuit (Figure 4.4 b).

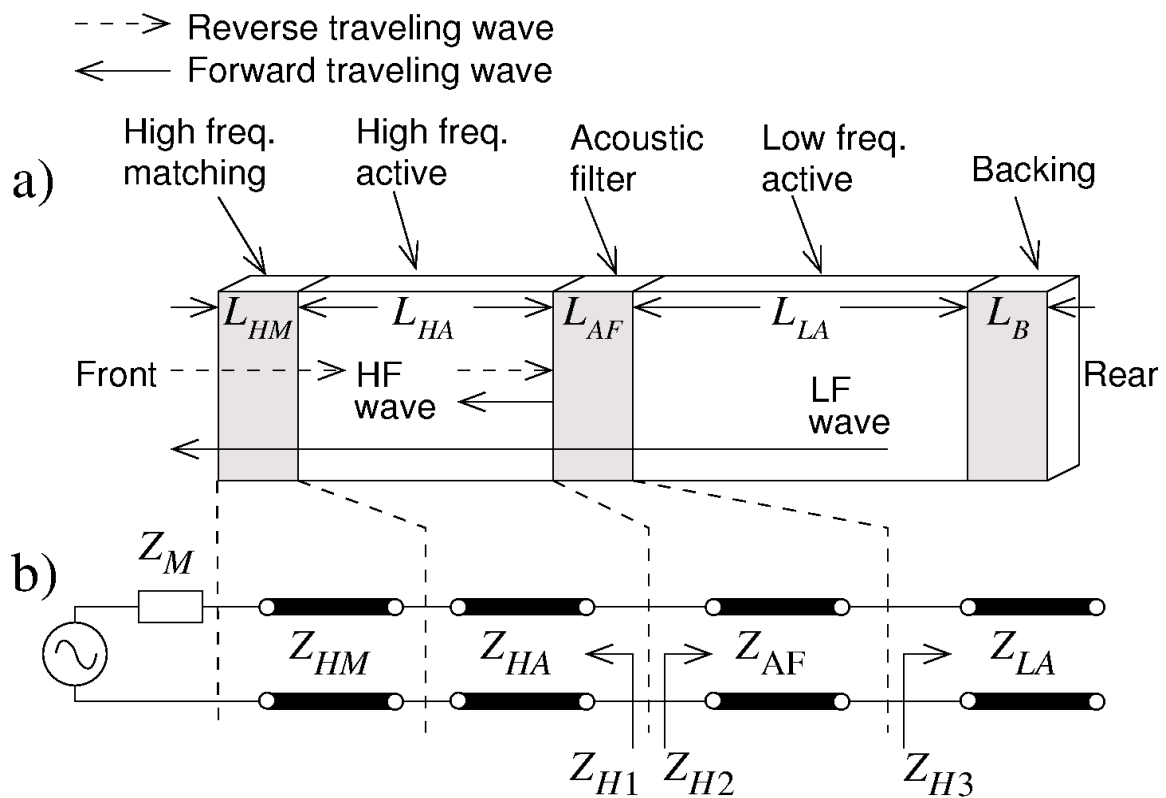


Figure 4.4 Anti-matching (acoustic filter) design for the high frequency receiving wave. a) Structure of the dual frequency transducer; b) equivalent circuit for the high frequency wave propagation.

The anti-matching layer for the high frequency element could be designed based on wave reflection (Type I) or wave absorption (Type II) in the stop band. For Type I transducer design, an anti-matching layer shifts the perfectly matched impedance (if $Z_{HA} = Z_{LA}$) into a great mismatch between Z_{H1} and Z_{H2} . As shown in Figure 4.4 b), the incident high frequency wave through the matching layer of the high frequency element is equivalent to a voltage (stress) source with Z_{HA} Thevenin impedance. As a result, the output impedance at high frequency element is $Z_{H1} = Z_{HA}$. Pulse length of the high frequency wave was spatially shorter than the twice of the low frequency element thickness. If the short pulse entered the low frequency element, the pulse would terminate before the reflected wave arrived at the input interface again. Then the reflected wave from back side of the low frequency element could not interfere with the incident wave at the input boundary of the low frequency element. In this case, $Z_{H3} = Z_{LA}$ and the input impedance Z_{H2} at the front surface of the anti-matching layer is

$$Z_{H2} = Z_{AF} \frac{Z_{LA} \cosh(\gamma_{HF} l) + Z_{AF} \sinh(\gamma_{HF} l)}{Z_{AF} \cosh(\gamma_{HF} l) + Z_{LA} \sinh(\gamma_{HF} l)}, \quad (4.11)$$

where γ is the propagation constant and l is the thickness of the anti-matching layer. The propagation constant is defined as $\gamma_{HF} = \alpha_{HF} + j\beta_{HF}$ where α_{HF} is the attenuation coefficient and β_{HF} is the phase constant. The anti-matching layer is thin compared to the low frequency

wavelength, as a result, the loss is negligible $\alpha_{HF}l \approx 0$ if the attenuation is not very high, and $\gamma_{HF}l$ reduces to $j\beta_{HF}l$ so that the input impedance at Z_{H2} reduces Equation (4.3)

$$Z_{H2} = Z_{AF} \frac{Z_{LA} + jZ_{AF} \tan(\beta l)}{Z_{AF} + jZ_{LA} \tan(\beta l)}, \quad (4.12)$$

where the phase constant β is equal to the wave number k in this lossless case. As derived in Section 4.1, the intensity transmission coefficients T_I are identical in both mechanical and electromagnetic calculations.

The AWR software (AWR corp., EI Segundo, CA) was used to simulate the performance of the reflection coefficient and the transmission coefficient. Different characteristic impedances were assigned to the anti-matching layer to show the corresponding reflection coefficient. The simulation circuit with lossless transmission line is shown in Figure 4.5. Similarly for the transmission line simulation with loss, the value “Loss” in each transmission line was assigned with multiple times of value defined in “loss_AF”. In order to make the simulation more close to the acoustic wave, the dielectric constant in the transmission line was specially calculated to make the value at the frequency equal the relative length of the transmission line. Impedances of the components and ports were set according to the acoustic impedances.

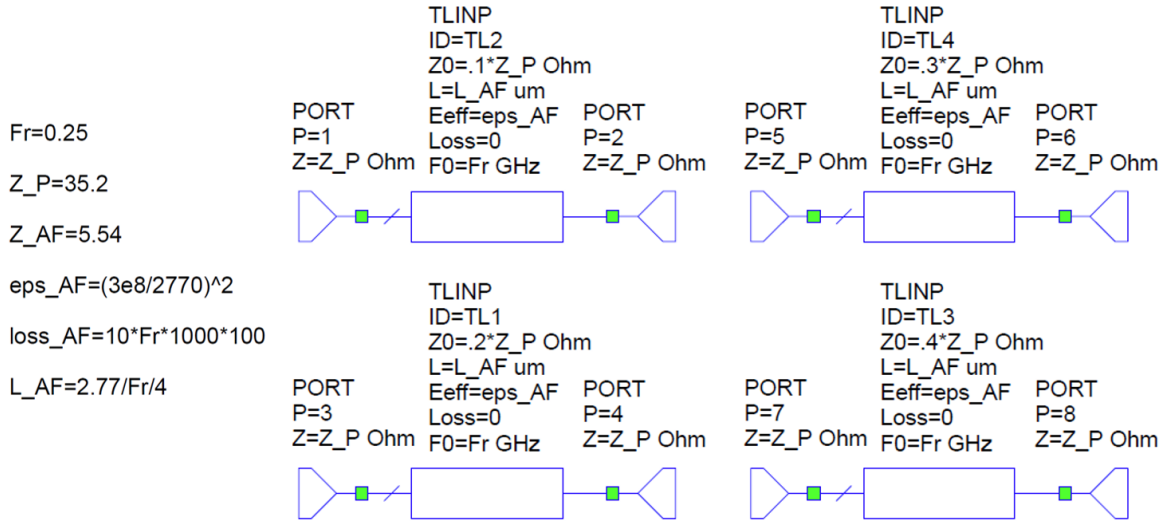


Figure 4.5 Simulation circuit of the anti-matching layer with different characteristic impedances.

Insertion loss (IL) was used to indicate the performance of the anti-matching layer, which mainly depends on Z_{AF} and $\gamma_{HF}l$. Starting with $Z_{P1} = Z_{P2}$, the lossless anti-matching layer, acting as a section of transmission line connected between Z_{P1} and Z_{P2} (Figure 4.4 b), shifts from ideal match condition Z_{H3} (center) to free-moving boundary condition Z_{H2} (left side close to the edge). The lower Z_{AF} is accompanied with the lower Z_{H2} (see loci of the Smith chart in Figure 4.6). At $\lambda_{HF} / 4$, reflection coefficient becomes maximum in amplitude and 0 in phase, so that insertion loss becomes maximum (Figure 4.7). An insertion loss of 10 dB and 20 dB are achievable using a lossless anti-matching layer with a relative impedance $Z_{rel} = Z_{AF} / \sqrt{Z_{P1}Z_{P2}}$ of 0.15 and 0.05, respectively. The AWR software simulation result proved that the loss is negligible (< 1 dB) on insertion loss at $\lambda_{HF} / 4$ if the attenuation is within

30 dB/cm/MHz (Type I in Figure 4.8). On the contrary, as the thickness of acoustic filter layer increases to $>1.2\lambda_{HF}$ with 30 dB/cm/MHz attenuation, the insertion loss is dominated by the loss and converges to a backing layer (Type II in Figure 4.8).

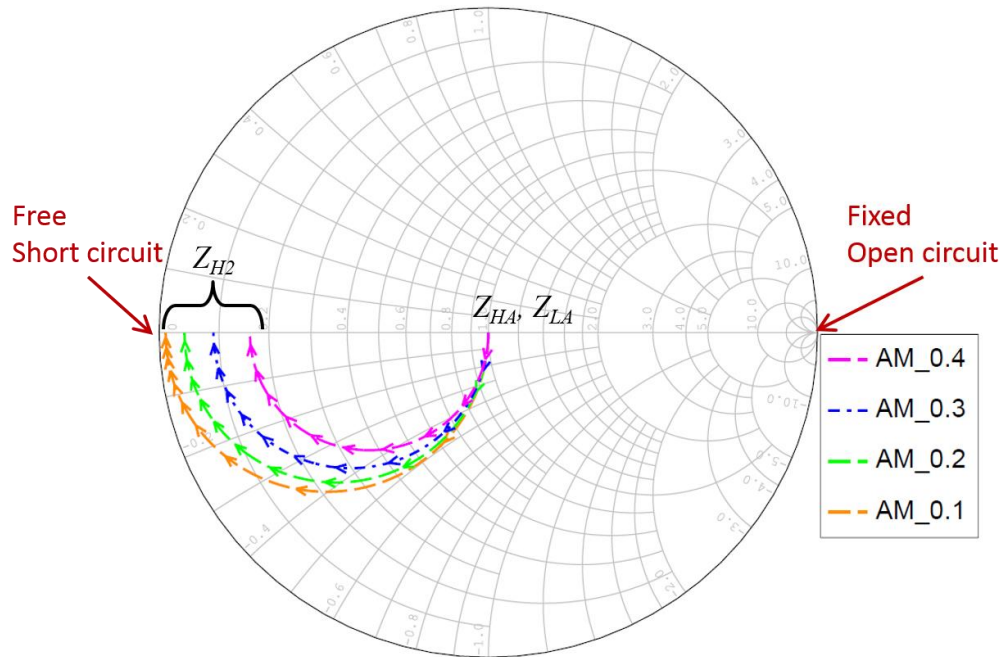


Figure 4.6 Loci of the quarter wavelength anti-matching layer. The numbers in the legend followed by “AM” indicate the relative impedance of the anti-matching layer.

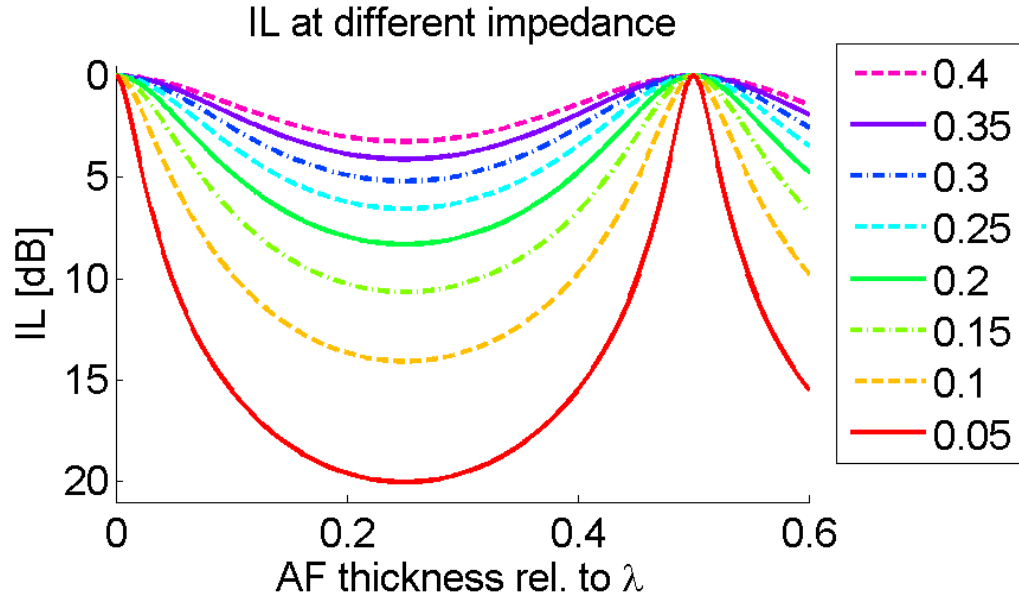


Figure 4.7 Insertion loss of the anti-matching layer dependent on the relative impedance Z_{AF}/Z_{LA} (values labeled in legend) and thickness L_{AF} (x-axis).

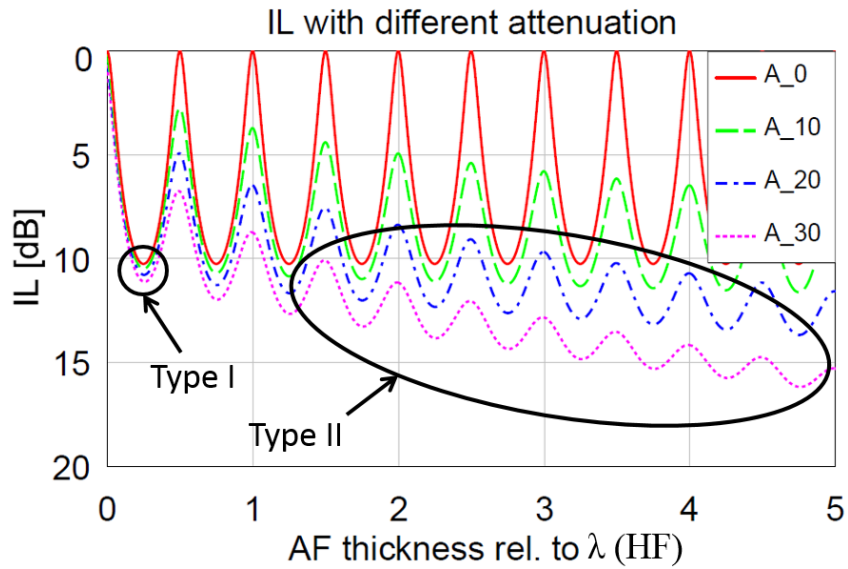


Figure 4.8 Insertion loss of the anti-matching layer with attenuation (in dB/cm/MHz) labeled as legend numbers followed by "A". Relative impedance of the passive amplifier is 0.157 (from actual case).

The anti-matching layer design was validated by comparing the experimental results of piezoelectric transducer prototypes with the theoretical calculation. Anti-matching performance of the Type II transducer is very straightforward and widely accepted [156, 157]. The performance in Type I was verified by transducer prototypes. In the verification, $f_{HF} = 30\text{MHz}$ and $f_{LF} = 3.5\text{MHz}$. The impedances are $Z_{P1} = Z_{P2} = 35.2\text{MRayl}$ and $Z_{AF} = 5.53\text{MRayl}$. The thicknesses for anti-matching verification are $L_{AF} = 0.25\lambda_{HF}$ and $L_{HF} = 0.5\lambda_{HF}$.

The anti-matching effect is revealed by the amplitude of aliasing echo reflected from rear side of the low frequency element. Without the anti-matching layer, the received ultrasound wave would continue propagating from the high frequency element to the low frequency element, and the reflected wave from the rear surface of low frequency element would excite the high frequency receiver again, appearing as an aliasing echo. Such echo may be reflected back and forth which result in a serial of wave packages after the main pulse from real target (Figure 4.9 a). On the contrary, such aliasing echoes were suppressed to < -20 dB in a round loop (Figure 4.9 b) with the acoustic filter layer sandwiched between the high frequency and low frequency elements. Pulse length (-20 dB) was significantly reduced from 555 ns to 152 ns, leading to an axial imaging resolution enhancement from 0.416 mm to 0.114 mm in water.

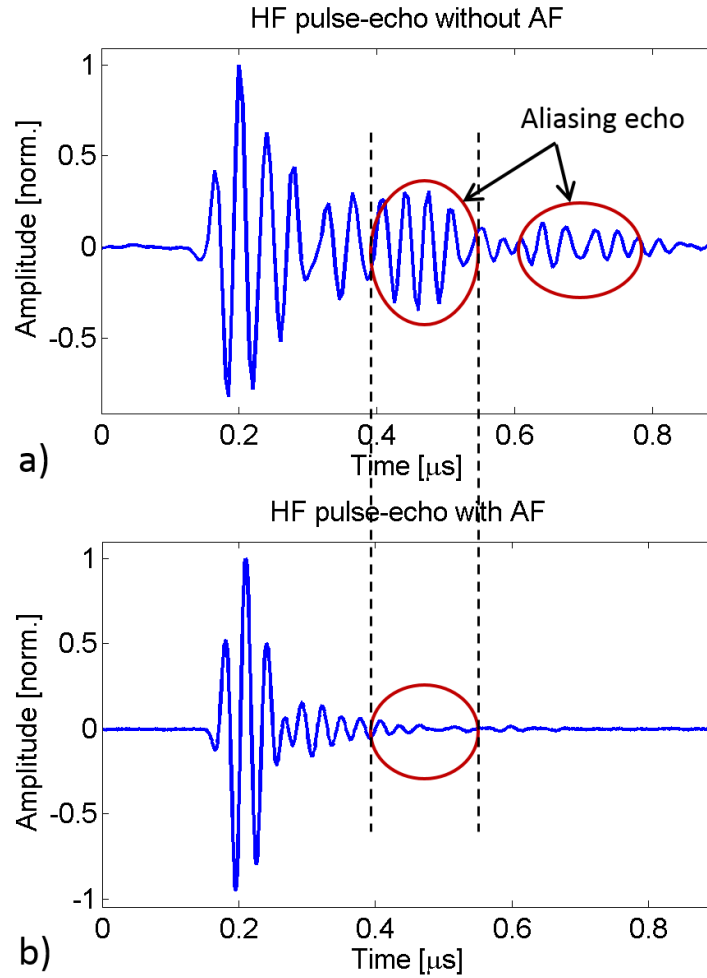


Figure 4.9 High frequency pulse-echo response on transducer prototypes, a) without anti-matching layer and b) with anti-matching layer.

4.3 Passive amplifier for the low frequency transmitting wave

The passive amplifier effect of the acoustic filter for low frequency transmitting wave was not straightforward in mechanical analysis. However, applying the multi-section of

transmission lines discussed in Section 1.3 and the similar equivalent circuit discussed in Section 4.1, the analysis calculation could still be applicable and intuitive.

For the low frequency transmitting wave, the transducer structure (Figure 4.10 a) is equivalent to the transmission line network shown in Figure 4.10 b). The amplification effect is studied by comparing the transmission efficiency with and without the passive amplifier. In the analysis of the low frequency transmission, reflection from the backing layer is neglected. In actual case without perfect backing, the reflected wave from rear side would inevitably lead to the energy accumulation in the low frequency element and compensate the pressure output enhancement. Such compensation will be shown in the experiment. As for analysis, the active low frequency element is considered as a voltage (stress) source with Thevenin impedance of Z_{p2} . The medium is large in space with no phase delay between strain and stress, and hence it is considered as a pure resistive load Z_M . Because the thickness of the front layers (high frequency matching, high frequency active and the passive amplifier layers) are all very short compared to the low frequency transmission wavelength, there are strong interference between the incident wave and the reflected wave. In this case, these layers are considered as sections of transmission lines in cascade connection. As shown in Equation (1.51), the input impedance at Z_{L3} could be calculated from

$$\begin{bmatrix} p_{L3} \\ v_{L3} \end{bmatrix} = \begin{bmatrix} A & B \\ C & D \end{bmatrix}_{AF} \begin{bmatrix} A & B \\ C & D \end{bmatrix}_{HA} \begin{bmatrix} A & B \\ C & D \end{bmatrix}_{HM} \begin{bmatrix} p_M \\ v_M \end{bmatrix}, \quad (4.13)$$

where P_{L3} , P_M are the pressure and v_{L3} , v_M are the volume velocity at the specific material, which satisfy $p_{L3} / v_{L3} = Z_{L3}$ and $p_M / v_M = Z_M$. The subscripts \square_{AF} , \square_{HA} and \square_{HM} at each ABCD matrix indicate the transmission line sections of the passive amplifier (acoustic filter) layer, high frequency active layer and the high frequency matching layer, respectively. The ABCD parameter of each section of the transmission line is defined as

$$\begin{bmatrix} A & B \\ C & D \end{bmatrix} = \begin{bmatrix} \cosh(\gamma_{LF}l) & Z_0 \sinh(\gamma_{LF}l) \\ Y_0 \sinh(\gamma_{LF}l) & \cosh(\gamma_{LF}l) \end{bmatrix}, \quad (4.14)$$

where Z_0 denotes the characteristic impedance of the specific transmission line and Y_0 is the conductance defined as $1/Z_0$. Propagation constant γ_{LF} and the thickness l are also referred to the specific transmission line section. If the attenuation is neglected, then the transmission

coefficient is $T_p = \frac{2Z_{L3}}{Z_{L3} + Z_{P2}^*}$, where $Z_{L3} = \frac{P_{L3}}{v_{L3}}$. Nevertheless, when the attenuation is non-

trivial, no analytical calculation exists and the performance was estimated as a scattering parameter S21 of a 2-port transmission line network simulated by AWR software. Due to the existence of the high frequency element in front of the low frequency element, the traditional quarter wavelength matching layer is always disturbed by the high frequency element. According to wave theory, the insertion of the passive amplifier layer enhances the transmission efficiency and results in a negative insertion loss, suggesting this passive layer functions as an amplifier, and consequently, denominated as a passive amplifier for the low frequency wave.

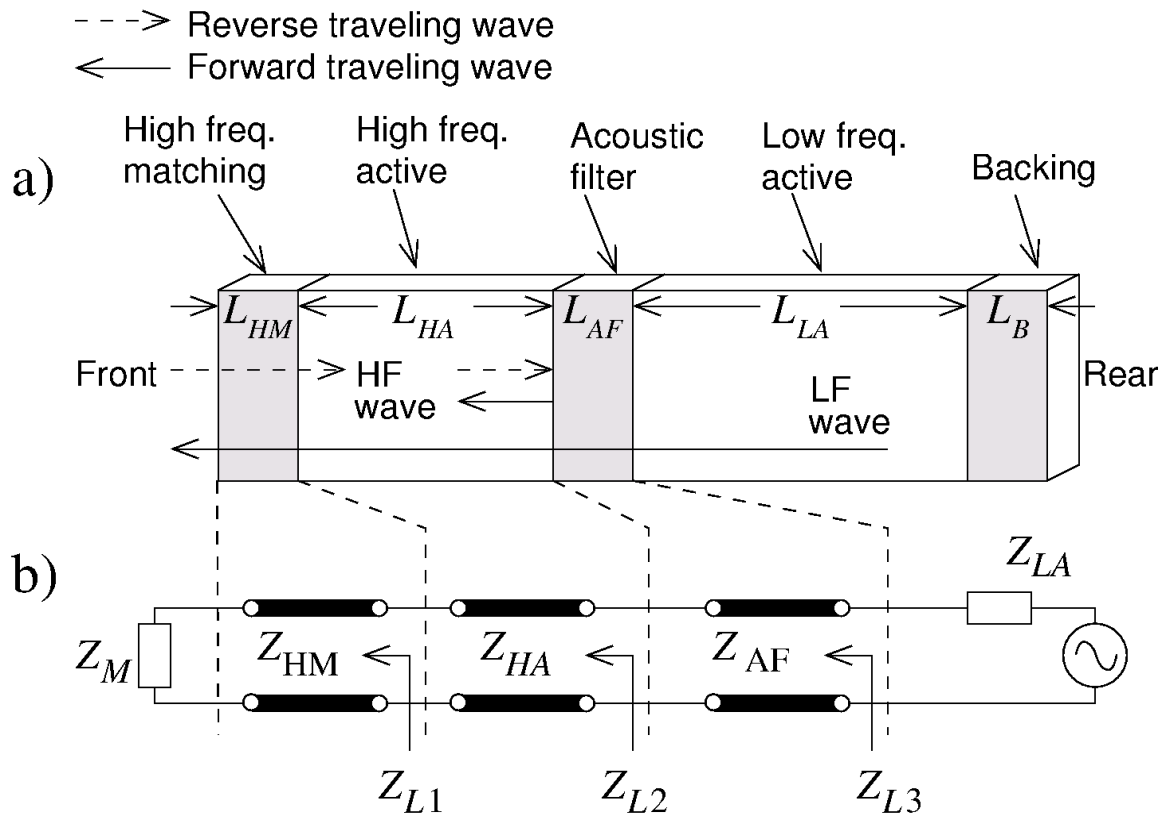


Figure 4.10 Passive amplifier (acoustic filter) design for the low frequency receiving wave. a) Structure of the dual frequency transducer; b) equivalent circuit for the low frequency wave propagation.

The AWR software was used to simulate the performance of the passive amplifier as well on the reflection coefficient and the transmission coefficient. A lot of variables could be adjusted. Different characteristic impedances were assigned to the passive amplifier layer to show the corresponding reflection coefficient. The simulation circuit with lossless transmission line is shown in Figure 4.11. Similarly for the transmission line simulation with loss, the value “Loss” in each transmission line was assigned with multiple times of value defined in “loss_AF”. In order to make the simulation more close to the acoustic wave, the

dielectric constant in the transmission line was specially calculated to make the value at the frequency equal the relative length of the transmission line. Impedances of the components and ports are set according to the acoustic impedances.

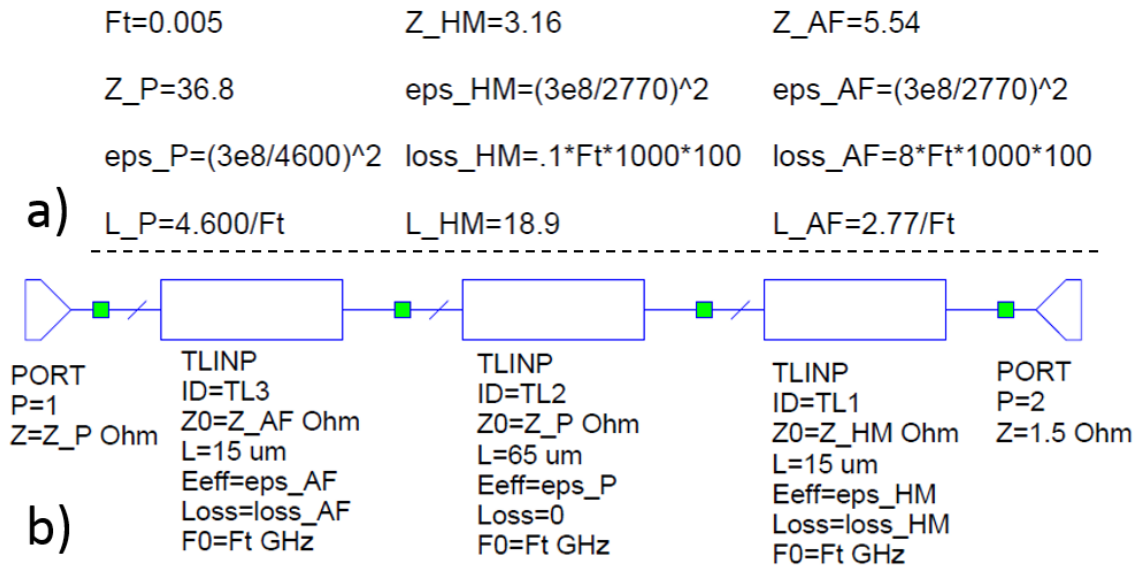


Figure 4.11 Simulation circuit of the passive amplification layer with typical parameters from the dual frequency transducer.

Gain of the passive amplifier was evaluated by the thickness combinations of the high frequency active layer and the passive amplifier layer. The transmission efficiency with these multi-layers is compared to that with $L_{AF} = 0$ (Figure 4.13) because it is the case without the acoustic filter layer and the TE is almost constant (< 0.005 dB variance) at high frequency active layer $L_{HA} \leq 0.1\lambda_{LF}$ (see leftmost edge of Figure 4.13). If $L_{HA} = 0$ and $L_{AF} = 0.25\lambda_{LF}$,

then it is a traditional matching layer as shown in Point A. However, if $L_{HA} > 0$, the TE has not been predicted before because impedances of the layers are far from ideal multiple matching layer design [158]. As L_{HA} increases from $L_{HA} = 0$, L_{AF} with maximum gain decreases as shown on point A \rightarrow D \rightarrow E \rightarrow F \rightarrow G. The magnitude of the maximum gain remains almost constant up to $L_{HA} = 0.03\lambda_{LF}$ (Point E) and decreases as L_{HA} further increasing (Point F and G). This result suggests the feasibility of designing dual frequency transducers with high frequency element in front of the low frequency element without sacrificing the transmission efficiency of the low frequency element. At the green dash line contour marked as Type II in Figure 4.13), $L_{AF} > 2.5L_{HA}$, also $L_{AF} > 1.25\lambda_{HF}$, at least 10 dB insertion loss could be achieved if the attenuation of the acoustic filter layer is 30 dB/cm/MHz (Figure 4.8). For the low frequency ultrasound, however, as the frequency $f_{LF} < f_{HF} / 14$, the attenuation is still sufficiently low so that the transmission efficiency is still good. This is Type II dual frequency transducer (A, D and E in Figure 4.13), in which the acoustic function as an absorber for high frequency element and passive amplifier for low frequency element. If $f_{HF} \leq 10f_{LF}$, and the difference of loss is not sufficient for high frequency absorption and low frequency amplification, then the anti-matching effect could be used based on reflection from impedance mismatch as stated in Section 4.2.3. $L_{HF} \approx 0.5\lambda_{HF}$ and $L_{AF} = 0.25\lambda_{HF}$, so $L_{AF} \approx 0.5L_{HF}$, as shown on the green dash line marked as Type I in Figure 4.13). Although amplification gain is not as good as Type II, it still reaches up to 5 dB gain at certain frequency

ratio compared to that without such an acoustic filter layer. This is Type I dual frequency transducer (G in Figure 4.13) which uses the acoustic as an anti-matching layer for high frequency element and passive amplifier for low frequency element. For both Type I and Type II (green dash lines in Figure 4.13), this acoustic filter resulted in positive gain for low frequency ultrasound. The existence of the high frequency active layer is not negligible (See Point B vs D) as assumed in traditional analysis although it is very thin $L_{HF} \approx 0.02\lambda_{LF}$. This happens because impedance shifting efficiency is not uniform along the locus. If the starting point of the transmission line is almost a short circuit (left most point in Smith chart), $Z_{L3} \approx jZ_{AF} \tan(\beta_{LF}l)$, and $\Delta Z_{L3} \approx jZ_{AF} \tan(\beta_{LF}\Delta l)$ is a small value if $\beta_{LF}l$ is small. This effect is illustrated at the high frequency matching layer (the gray solid line at the starting point of the HF active black solid line), where $L_{HM} = 0.024\lambda_{LF}$ with an impedance of $Z_{rel} = 0.157$. The low impedance thin layer is negligible if its load is almost short circuit (free to move with no phase). However, if the locus goes to the almost open circuit (right most point of Smith chart, then $Z_{L3} \approx -jZ_{AF} / \tan(\beta_{LF}l)$ and $\Delta Z_{L3} \approx jZ_{AF} \tan(\beta_{LF}\Delta l) / \tan^2(\beta_{LF}l)$, indicating ΔZ_{L3} can be pretty large if $\beta_{LF}l$ is small. In Loci of $L_{HF} = 0.02 \sim 0.1\lambda_{LF}$, the existence of the high impedance high frequency active layer shifted Z_{L2} away from the short circuit condition so that the acoustic filter layer shifts Z_{L3} very efficiently. It is not quarter wavelength for L_{AF} to makes zero phase on Z_{L3} , but is much shorter (0.03 - 0.125), as shown in the numbers followed the underscores in the legend of Figure 4.12).

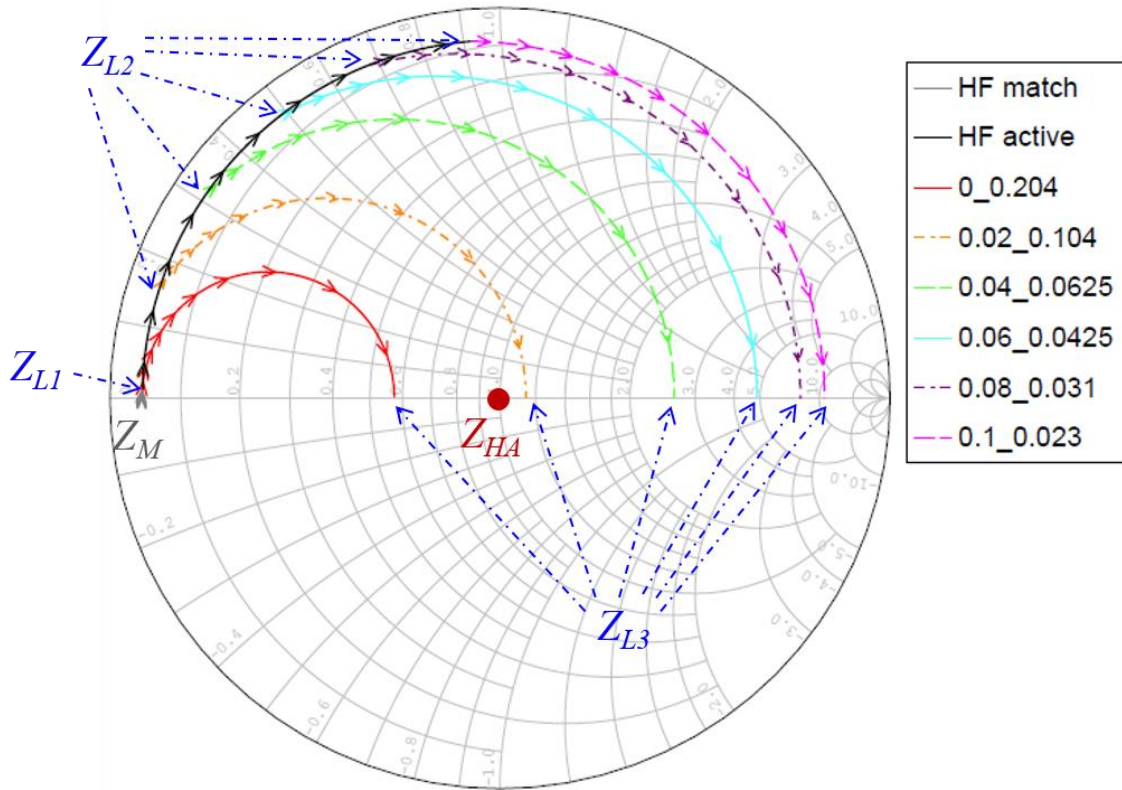


Figure 4.12 Loci of the input impedance of the front layers (high frequency matching, high frequency active and the passive amplifier layers). The numbers ahead of the underscores are the thickness of the high frequency active layer relative to low frequency wavelength. Numbers followed the underscores are the corresponding passive amplifier thickness that make Z_{L3} zero phase. Relative impedance of the passive amplifier is 0.157 (from actual case).

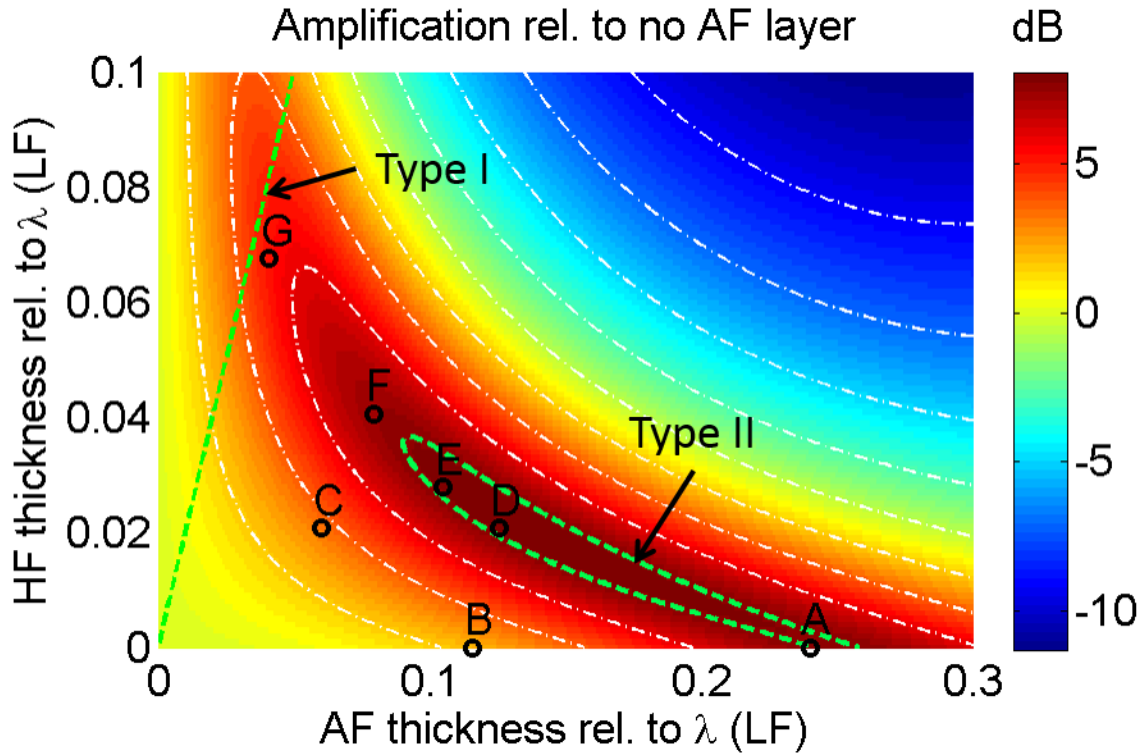


Figure 4.13 Gain of the passive amplifier with different thicknesses of the high frequency active layer and passive amplifier layer. Relative impedance of the passive amplifier is 0.157 (from actual case).

Performance of the passive amplifier was also validated by comparing of the pressure output from transducer prototypes with and without such layer. Thicknesses of the layers for such verification are marked in Figure 4.13 as (A) ideal traditional matching, (B) non-ideal traditional matching, (C) non-ideal condition with high frequency active and acoustic layer, and (D \Rightarrow G) ideal condition with high frequency active and acoustic filter layers. Transmitting pressure was measured by a hydrophone (HGL-0085, Onda Corp., Sunnyvale, CA) at a distance of 1 cm away from the transducers (aperture: 4 x 4 mm, natural focus at about 9.3 mm). The results for transducer A and E are shown in Figure 4.14 and compared

with that without matching. Pressures from both A and E are approximately 1.7 times of that from non-matching transducers. The measured gain was weakened by the reflection from rear side of the low frequency element. Actual gain was compensated by referring to the ideal matching condition (A). After compensation, the predicted and measured gains of the passive amplifier are shown in Figure 4.15. The measured results were in good agreement with the prediction, despite a slight discrepancy, which is possibly attributed to fabrication inaccuracies such as material properties, thickness of layers and boundary conditions.

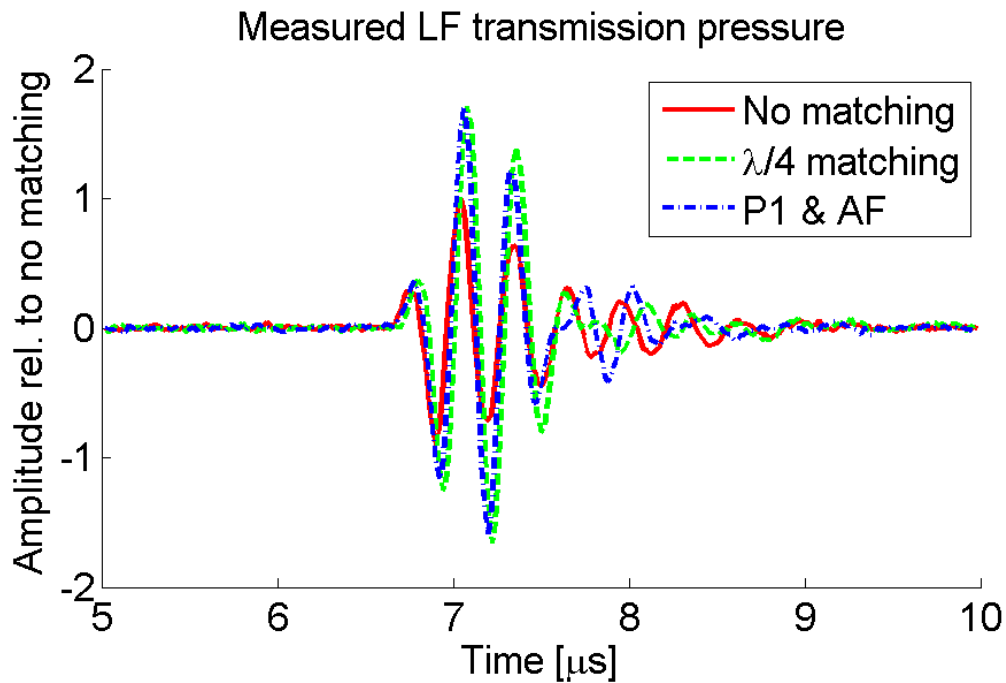


Figure 4.14 Pressure amplitude measured from the traditional matched (transducer A, quarter wavelength matching) and transducer with high frequency active and acoustic layer (transducer E, P1 & AF) normalized to that without matching layers (No matching).

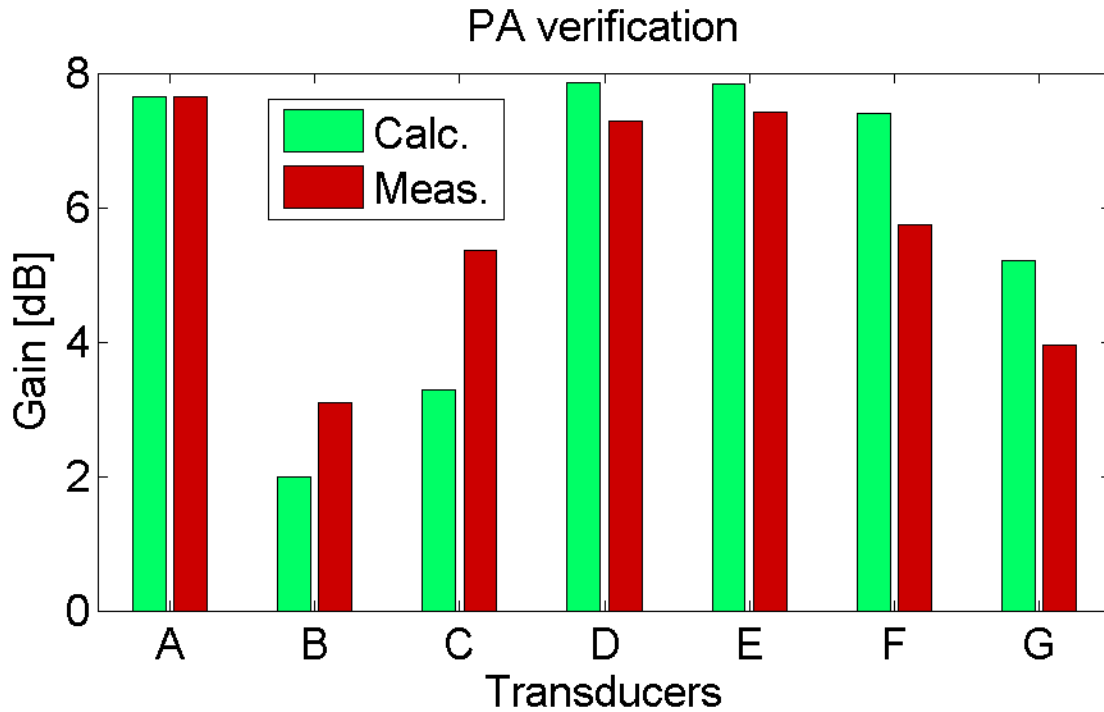


Figure 4.15 Gain of transmitting pressure output on the fabricated transducers normalized to that without matching layers.

4.4 Summary

In summary, this study demonstrated, for the first time, an acoustic filter based wave propagation control that works simultaneously as both a high frequency band stop filter and a low frequency passive amplifier. This acoustic filter is readily implemented in multi-frequency systems such as dual frequency transducers, which could be applied for super-harmonic imaging [86] as well as therapy-imaging [143]. Another potential application of such design is to integrate focusing lens with the matching layer, taking the advantage that different total

acoustic length ($L_{HF} + L_{AF}$ in A, D and E) is needed for keeping high transmission efficiency. This acoustic filter design is guided by microwave theory, and does not involve any microstructures or nonlinearities, making it very cost-effective in fabrication. Besides, the demonstrated acoustic filter is very compact (sub-wavelength along the wave propagation direction), a promising feature in space-limited applications such as biomedical intravascular ultrasound imaging or minimal invasive therapy. This theory and systematic design approach will lay a foundation for design of multi-frequency systems with desired wave propagation control.

Chapter 5.

Conclusion

Multi-frequency ultrasound was found to be an effective tool in biomedical applications, both for therapeutic ablation and for diagnostic acoustic angiography. Specific multi-frequency transducers were designed and demonstrated with prototypes. Special vibration modes and wave propagation control in multi-frequency transducers were analyzed and realized in detail. Microwave matching network methods, especially transmission line effects, were introduced to the mechanical wave control because of the same wave propagation properties. Methods developed in this multi-frequency transducer design are expected to be widely applicable in many other multi-frequency systems.

5.1 Dual frequency transducer for HIFU

In this research, single frequency ultrasound and dual frequency ultrasound were compared on their heat generation efficiency. The temperature at the focal point was numerically recorded with thermal couple at constant energy deposition. Dual frequency ultrasound with certain amplitude combination was validated to benefit from higher heating efficiency than either single frequency ultrasound. Such efficiency benefit was estimated as cavitation effect because more microbubbles were generated by dual frequency ultrasound and the microbubbles induced higher energy absorption efficiency. Inspired by previous work in multi-frequency tissue ablation [3, 103], a specific dual frequency transducer was designed with identical transmitting aperture between the two frequency beams. Such dual frequency

transducers possesses significant advantages in actual applications. First, the intrinsically confocal beam for the dual frequency ultrasound was generated by identical aperture but different vibration modes, which significantly simplified the dual frequency beam alignment. Second, single channel excitation on the transducer by dual frequency wave is much easier than multiple channel excitations to multiple transducers, which greatly reduced the machine cost and increased the portability. Compared with traditional HIFU transducers, this dual frequency transducer has higher heat generation efficiency so that lower energy intensity and less deposition time is needed, which may lead to higher safety in the treatment.

5.2 Dual frequency intravascular transducer for acoustic angiography

New design of dual-frequency IVUS transducers was developed in this work considering difficulties of the intravascular acoustic angiography. In order to realize the coronary wall vasorum imaging, dual frequency transducers were designed with the size small enough to be integrated into commercial catheters. Such dual frequency transducers overcame the limitations above and indicated promising results, which could be concludes as follows:

- A. The stacked multi-layer design of the dual frequency transducer was a success. This structure was negated by Neer *et al* [141] due to its electrical and mechanical coupling between the two active layers although it was one of the easiest to fabricate. In this research, we successfully decoupled the two active layers by an acoustic filter and developed the structure capable of super-harmonic imaging. The low frequency transmitting beam well covered the high frequency receiving beam, so that super-

harmonic signal excited by the low frequency ultrasound could be detected by the high frequency element. At the same time, the high frequency beam was very narrow (-6 dB beam width ~ 0.3 mm), which mainly made sure of the lateral resolution. In short, this acoustic filter assisted stacked layer design is easy to fabricate, free of dual active layer coupling and performed good beam profile compared with the alternatives.

- B. The acoustic filter design was a critical feature that made the stacked layer design functioning, which had significant contribution to both frequencies. For high frequency wave, it acted as an anti-matching layer that reflected majority of the acoustic wave energy so that little aliasing echo showed up in the imaging. For the low frequency wave, it acted as a passive amplifier that enhanced the transmission efficiency so that transmission pressure was high enough at the sensitive region of the receiving beam. However, the design and analysis of the acoustic filter was not straightforward because of the multi-layer interactions. To make the analysis easy and intuitive, microwave methods were introduced, considering the multi-layers of the transducer as transmission line networks.
- C. The multi-layer analysis method developed from microwave networks successfully guided the multi-frequency system design. According to mathematically identical wave equations, the acoustic wave response could be directly plotted in Smith chart that has been widely adopted in microwave design, and the multi-layer acoustic system design was subjected to the manipulation of the loci in Smith chart. Transmission and reflection coefficients at the boundaries could be numerically calculated from cascade

of transmission lines. Transmission coefficient in lossy materials could not be calculated directly, in which case, commercial software are readily available for this estimation. Transducers were fabricated to verify the performance, which showed good agreement with the estimation. The microwave methods were proven very helpful for a multi-layer system wave propagation analysis.

- D. In the transmitter frequency selection, the 5 MHz transmitter generated higher CTR than the 6.5 MHz one at constant pressure output and with constant receiver frequency at 30 MHz. This indicates that reasonably lower frequency transmitter is preferable for a high CTR imaging. However, the transmitter frequency cannot be extremely low because of the dimension limit in catheter. With the width-to-thickness ratio ≥ 2 , the lowest transmitting frequency is about 6.5 MHz if the diagonal dimension of the transducer is limited within 1 mm. It's not preferable to simply increase the thickness of the transmitter, because lateral vibration mode coupling and long reverberation causes low axial resolution. One solution was to use composite materials with 1-3 connections, which are good at lateral mode suppression.
- E. In the transmitter material selection, PMN-PT 1-3 composite exhibited shorter pulse length than PMN-PT single crystal, leading to significant enhancement of axial resolution. Due to the clean thickness vibration mode (lateral mode suppressed) and high piezoelectric performance (high k_t and low impedance), the settle time is much shorter than that in single crystal. With 1-cycle excitation, the PMN-PT 1-3 composite generated single negative peak (within -6 dB), which significantly decreased the

excitation time on microbubbles, resulting in very short pulse ($\sim 70 \mu\text{m}$) super-harmonic signal on the receiving element. Such high resolution is close to the diameter of the second order vasa vasorum (67.99 ± 2.72) [138], indicating the capability of intravascular acoustic angiography to such vasa vasorum.

F. Intravascular acoustic angiography is applicable, so that most cardiovascular diseases are predictable. This dual frequency transducer design overcame the difficulties and the prototypes generated high CTR, high resolution micro-vessel (mimicked by cellulose tube) images with super-harmonic imaging method by transmitting at 5 – 6.5 MHz and receiving at 30 MHz. Such micro-vessel imaging capability demonstrated the viability that the plaque vulnerability could be predicted by intravascular acoustic angiography. An early evaluation of the plaque vulnerability signifies an early diagnosis of most atherosclerosis cardiovascular diseases, and the possibility of early health care for life saving.

5.3 Acoustic filter layer design

The acoustic filter design was derived from microwave networks, and potentially applied to wave propagation control in various multi-frequency systems. Characteristics of each component were taken into account and the overall performance of the system was evaluated by cascading all the components. Pass band and stop band were calculated according to the actual wave propagating in the system. For the specific case of the acoustic filter design in the

dual frequency transducer, certain equivalences were made according to the wavelength, pulse length and the thickness of each layer.

In the high frequency stop band design, the acoustic filter acted as an anti-matching layer that reflected most energy within the stop band. As is shown in Figure 3.11, the high frequency signal is very like a single frequency sinusoidal signal convoluted with Hamming window, so that most energy of the receiving signal is within this frequency range (e.g. 25 – 35 MHz) and little energy is leaked to the harmonics. Such signal was efficiently reflected if the stop band of the filter is properly designed. In this high frequency stop band design, the thickness of the low frequency element is larger than a half of the pulse length, so that the reflected signal does not interfere with the incident wave at the interface. Consequently, the input impedance at the low frequency element was considered as its characteristic impedance. This equivalence was validated to be correct because the measured results matched very well with the calculations based on the equivalence. Overall, the acoustic filter fulfilled the goal that the receiving signal was highly reflected and the aliasing echo was highly suppressed.

In the low frequency pass band design, the acoustic filter acted as a passive amplifier layer that enhanced the transmission coefficient. All the layers in front of the low frequency element (acoustic filter layer, high frequency active layer and the high frequency matching layer) are thin compared to the pulse length or even wavelength of the low frequency acoustic wave. In this case, these layers were considered as sections of transmission lines connected in cascade. With proper design of the multiple layers, the acoustic filter not only passed the wave within

the pass band, but also enhanced the output pressure. Such enhancement made sure that the transmitting pressure was high enough within the sensitive region of the receiver beam.

In the dual frequency ultrasound transducer, the acoustic filter accomplished the goal of both aliasing echo suppression and the transmitting pressure enhancement. The design approach developed in this filter is expected to be widely advisable in multi-layer, multi-frequency systems.

5.4 Suggestions for future work on dual frequency IVUS transducers

The small aperture dual frequency transducers were housed on hypodermic needles to demonstrate that the dimension is suitable for intravascular angiography. In future, such transducers will be integrated into catheters and be rotated by shafts at a very high speed. In order to protect the transducers, it is suggested that the transducers be housed in specifically designed boats at the tip of the catheters.

The catheter length is not negligible compared to the wavelength of the high frequency receiving wave. If the receiving frequency is kept at 30 MHz and the dielectric constant of the electrical cable insulator is about 4, then the electromagnetic wavelength of in the cable is

about $\frac{3 \times 10^8}{\sqrt{4} \times 30 \times 10^6} = 5\text{m}$. The catheter length is usually about 1 m (close to $\lambda / 4$), which

is comparable to the wavelength. Several approaches could be used for the impedance matching. First, tiny matching network could be placed at the front end of the catheter close to the transducer, which matches the impedance to the system impedance (like 50 Ω). In this case,

the length of the cable can be arbitrary if its characteristic impedance is 50Ω . Second, the impedance of the transducers are usually not 50Ω and usually possesses some capacitance. Length and characteristic impedance of the cable could be designed according to the impedance of the transducer, so that the cable acts as a matching network between the transducer and the imaging system. Third, if the dual frequency transducer is replaced by a dual frequency array, then there would be strong crosstalk among the multiple cables which are parallel with one another. Some compact signal processing units could be placed at the front end to increase the information density and robustness of the signal on the cable (for example frequency modulation), so that the number of cables could be reduced and more reliable signals could be transferred to the imaging system.

REFERENCES

- [1] F. A. Duck, A. C. Baker, and H. C. Starritt, *Ultrasound in medicine*: CRC Press, 2002.
- [2] T. L. Szabo, *Diagnostic ultrasound imaging: inside out*, 2 ed.: Academic Press, 2014.
- [3] S. Guo, Y. Jing, and X. Jiang, "Temperature rise in tissue ablation using multi-frequency ultrasound," *IEEE Trans Ultrason Ferroelectr Freq Control*, vol. 60, no. 8, pp. 1699-1707, 2013.
- [4] R. C. Gessner, C. B. Frederick, F. S. Foster, and P. A. Dayton, "Acoustic angiography: a new imaging modality for assessing microvasculature architecture," *Int J Biomed Imaging*, vol. 2013, pp. 936593, 2013.
- [5] P. CURIE, and J. CURIE, "Développement par compression de l'électricité polaire dans les cristaux hémidres à face inclinés," *Bulletin de la Societe ineralogique de Fran*, vol. 3, pp. 90, 1880.
- [6] K. M. Lakin, "Modeling of thin film resonators and filters," in 1992 IEEE Int Microw Symp Dig, 1992, pp. 149-152.
- [7] J. G. Lynn, R. L. Zwemer, A. J. Chick, and A. E. Miller, "A new method for the generation and use of focused ultrasound in experimental biology," *J Gen Physiol*, pp. 179-193, 1942.
- [8] B. Jaffe, R. Roth, and S. Marzullo, "Properties of piezoelectric ceramics in the solid-solution series lead titanate-lead zirconate-lead oxide: tin oxide and lead titanate-lead hafnate," *J Res Nat Bur Stand*, vol. 55, no. 5, pp. 239-254, 1955.

- [9] W. Liu, and X. Ren, "Large piezoelectric effect in Pb-free ceramics," *Phys Rev Lett*, vol. 103, no. 25, pp. 257602, 2009.
- [10] L. E. Cross, "Relaxor ferroelectrics," *Ferroelectrics*, vol. 76, no. 1, pp. 241-267, 1987.
- [11] S. Zhang, J. Luo, W. Hackenberger, and T. R. Shrout, "Characterization of $\text{Pb}(\text{In}_{1/2}\text{Nb}_{1/2})\text{O}_3\text{-Pb}(\text{Mg}_{1/3}\text{Nb}_{2/3})\text{O}_3\text{-PbTiO}_3$ ferroelectric crystal with enhanced phase transition temperatures," *J Appl Phys*, vol. 104, no. 6, pp. 064106, 2008.
- [12] X. Geng, T. A. Ritter, and K. K. Shung, "Optimization of 1-3 relaxor-PT single-crystal/polymer composites," in *Med Imaging 1999*, 1999, pp. 24-30.
- [13] R. Zhang, B. Jiang, and W. Cao, "Elastic, piezoelectric, and dielectric properties of multidomain $0.67\text{Pb}(\text{Mg}_{1/3}\text{Nb}_{2/3})\text{O}_3\text{-}0.33\text{PbTiO}_3$ single crystals," *J Appl Phys*, vol. 90, no. 7, pp. 3471-3475, 2001.
- [14] S. Zhang, J. Luo, W. Hackenberger, N. P. Sherlock, R. J. Meyer *et al.*, "Electromechanical characterization of $\text{Pb}(\text{In}_{0.5}\text{Nb}_{0.5})\text{O}_3\text{-Pb}(\text{Mg}_{1/3}\text{Nb}_{2/3})\text{O}_3\text{-PbTiO}_3$ crystals as a function of crystallographic orientation and temperature," *J Appl Phys*, vol. 105, no. 10, pp. 104506-104506-5, 2009.
- [15] G. Pfister, M. Abkowitz, and R. Crystal, "Pyroelectricity in polyvinylidene fluoride," *J Appl Phys*, vol. 44, no. 5, pp. 2064-2071, 1973.
- [16] H. Ohigashi, "Electromechanical properties of polarized polyvinylidene fluoride films as studied by the piezoelectric resonance method," *J Appl Phys*, vol. 47, no. 3, pp. 949-955, 1976.

- [17] K. H. Lam, and H. L. W. Chan, "Piezoelectric cement-based 1-3 composites," *Appl Phy A*, vol. 81, no. 7, pp. 1451-1454, 2005.
- [18] K. C. Cheng, H. L. Chan, C. L. Choy, Q. Yin, H. Luo *et al.*, "Single crystal PMN-0.33 PT/epoxy 1-3 composites for ultrasonic transducer applications," *IEEE Trans Ultrason Ferroelectr Freq Control*, vol. 50, no. 9, pp. 1177-1183, 2003.
- [19] H. Taunamang, I. Guy, and H. L. Chan, "Electromechanical properties of 1 - 3 piezoelectric ceramic/piezoelectric polymer composites," *J Appl Phys*, vol. 76, no. 1, pp. 484-489, 1994.
- [20] H. Savakus, K. Klicker, and R. Newnham, "PZT-epoxy piezoelectric transducers: a simplified fabrication procedure," *Mat Res Bull*, vol. 16, no. 6, pp. 677-680, 1981.
- [21] M. Lukacs, M. Sayer, G. Lockwood, and S. Foster, "Laser micromachined high frequency ultrasonic arrays," in 1999 IEEE Int Ultrason Symp, 1999, pp. 1209-1212.
- [22] K. A. Snook, C.-H. Hu, T. R. Shrout, and K. K. Shung, "High-frequency ultrasound annular-array imaging. Part I: Array design and fabrication," *IEEE Trans Ultrason Ferroelectr Freq Control*, vol. 53, no. 2, pp. 300-308, 2006.
- [23] J.-P. Desbiens, and P. Masson, "ArF excimer laser micromachining of Pyrex, SiC and PZT for rapid prototyping of MEMS components," *Sensors Actuators A-Phys*, vol. 136, no. 2, pp. 554-563, 2007.
- [24] I. A. Ivan, J. Agnus, and P. Lambert, "PMN-PT (lead magnesium niobate-lead titanate) piezoelectric material micromachining by excimer laser ablation and dry etching (DRIE)," *Sensors Actuators A-Phys*, vol. 177, pp. 37-47, 2012.

- [25] R. Liu, K. A. Harasiewicz, D. Knapik, N. Freeman, and F. S. Foster, "2–2 piezoelectric composites with high density and fine scale fabricated by interdigital pair bonding," *Appl Phy Lett*, vol. 75, no. 21, pp. 3390-3392, 1999.
- [26] R. Liu, K. A. Harasiewicz, and F. S. Foster, "Interdigital pair bonding for high frequency (20-50 MHz) ultrasonic composite transducers," *IEEE Trans Ultrason Ferroelectr Freq Control*, vol. 48, no. 1, pp. 299-306, 2001.
- [27] J. M. Cannata, J. A. Williams, C.-H. Hu, and K. K. Shung, "Development of high frequency linear arrays using interdigital bonded composites," in 2008 IEEE Int Ultrason Symp, 2008, pp. 686-689.
- [28] J. Yin, M. Lukacs, K. Harasiewicz, and S. Foster, "Ultra-fine piezoelectric composites for high frequency ultrasonic transducers," in 2004 IEEE Int Ultrason Symp, 2004, pp. 1962-1965.
- [29] R. J. Meyer Jr, S. Yoshikawa, and T. R. Shrout, "Processing and properties of 15–70 MHz 1–3 PZT fiber/polymer composites," *Mat Res Innov*, vol. 3, no. 6, pp. 324-331, 2000.
- [30] A. Abrar, D. Zhang, B. Su, T. Button, K. Kirk *et al.*, "1–3 connectivity piezoelectric ceramic–polymer composite transducers made with viscous polymer processing for high frequency ultrasound," *Ultrasonics*, vol. 42, no. 1, pp. 479-484, 2004.
- [31] S. Cochran, A. Abrar, K. J. Kirk, D. Zhang, T. W. Button *et al.*, "Net-shape ceramic processing as a route to ultrafine scale 1-3 connectivity piezoelectric ceramic-polymer composite transducers," in 2004 IEEE Int Ultrason Symp, 2004, pp. 1682-1685.

- [32] K. Lubitz, A. Wolff, G. Preu, R. Stoll, and B. Schulmeyer, "New piezoelectric composites for ultrasonic transducers," *Ferroelectrics*, vol. 133, no. 1, pp. 21-26, 1992.
- [33] S. Wang, J. F. Li, K. Wakabayashi, M. Esashi, and R. Watanabe, "Lost silicon mold process for PZT microstructures," *Adv Mat*, vol. 11, no. 10, pp. 873-876, 1999.
- [34] X. Jiang, K. Snook, A. Cheng, W. Hackenberger, and X. Geng, "Micromachined PMN-PT single crystal composite transducers--15-75 MHz PC-MUT," in 2008 IEEE Int Ultrason Symp, 2008, pp. 164-167.
- [35] X. Jiang, K. Snook, W. Hackenberger, A. Cheng, and J. Xu, "Piezoelectric transducers using micromachined bulk piezo substrates," *Sensors*, pp. 573-576, 2008.
- [36] X. Jiang, J. R. Yuan, A. Cheng, K. Snook, and W. Hackenberger, "Micro/Nano Piezoelectric Composites for Advanced M/NEMS," in 2007 First Int Conf Integr Commercial of Micro and Nanosys, 2007, pp. 415-420.
- [37] X. Jiang, K. Snook, W. S. Hackenberger, and X. Geng, "Single crystal piezoelectric composites for advanced NDT ultrasound," in The 14th Int Symp Smart Struct Mat & Nondestruct Eval Health Monitor, 2007, pp. 65310F-8.
- [38] S. Mitragotri, "Healing sound: the use of ultrasound in drug delivery and other therapeutic applications," *Nat Rev Drug Discov*, vol. 4, no. 3, pp. 255-260, 2005.
- [39] J. Ma, S. Guo, D. Wu, X. Geng, and X. Jiang, "Design, fabrication, and characterization of a single-aperture 1.5-MHz/3-MHz dual-frequency HIFU transducer," *IEEE Trans Ultrason Ferroelectr Freq Control*, vol. 60, no. 7, pp. 1519-1529, 2013.

- [40] W. G. Pitt, G. A. Hussein, and B. J. Staples, "Ultrasonic drug delivery-a general review," *Expert Opin Drug Del*, vol. 1, no. 1, pp. 37-56, 2004.
- [41] K. y. Ng, and Y. Liu, "Therapeutic ultrasound: its application in drug delivery," *Med Res Rev*, vol. 22, no. 2, pp. 204-223, 2002.
- [42] D. Dumont, R. H. Behler, T. C. Nichols, E. P. Merricks, and C. M. Gallippi, "ARFI imaging for noninvasive material characterization of atherosclerosis," *Ultrasound Med Biol*, vol. 32, no. 11, pp. 1703-1711, 2006.
- [43] S. Guo, Y. Wang, N. Allbritton, and X. Jiang, "Ultrasound-induced release of micropallets with cells," *Appl Phys Lett*, vol. 101, no. 16, pp. 163703, 2012.
- [44] J.-N. Decarpigny, B. Hamonic, and O. B. Wilson Jr, "The design of low frequency underwater acoustic projectors: present status and future trends," *IEEE J Oceanic Eng*, vol. 16, no. 1, pp. 107-122, 1991.
- [45] V. Sivakumar, and P. G. Rao, "Power ultrasound-assisted cleaner leather dyeing technique: influence of process parameters," *Environ Sci Technol*, vol. 38, no. 5, pp. 1616-1621, 2004.
- [46] B. Andersen, E. Ringgaard, T. Bove, A. Albareda, and R. Pérez, "Performance of piezoelectric ceramic multilayer components based on hard and soft PZT," *Proc Actuator 2000*, pp. 419-422, 2000.
- [47] S. Zhang, and T. R. Shrout, "Relaxor-PT single crystals: observations and developments," *IEEE Trans Ultrason Ferroelectr Freq Control*, vol. 57, no. 10, pp. 2138-2146, 2010.

- [48] X. Huo, S. Zhang, G. Liu, R. Zhang, J. Luo *et al.*, “Elastic, dielectric and piezoelectric characterization of single domain PIN-PMN-PT: Mn crystals,” *J Appl Phys*, vol. 112, no. 12, pp. 124113, 2012.
- [49] Y. Jing, F. C. Meral, and G. T. Clement, “Time-reversal transcranial ultrasound beam focusing using a k-space method,” *Phys Med Bio*, vol. 57, no. 4, pp. 901, 2012.
- [50] C. J. Diederich, and K. Hynynen, “Ultrasound technology for hyperthermia,” *Ultrasound Med Biol*, vol. 25, no. 6, pp. 871–887, 1999
- [51] C. C. Coussios, C. H. Farny, G. Ter Haar, and R. A. Roy, “Role of acoustic cavitation in the delivery and monitoring of cancer treatment by high-intensity focused ultrasound (HIFU),” *Int J Hyperther*, vol. 23, no. 2, pp. 105-120, 2007.
- [52] T. J. Matula, “Inertial cavitation and single-bubble sonoluminescence,” *Phil Trans R Soc Lond A*, vol. 357, no. 1751, pp. 225-249, 1999.
- [53] P. Li, L.-q. Cao, C.-Y. Dou, W. F. Armstrong, and D. Miller, “Impact of myocardial contrast echocardiography on vascular permeability: an *in vivo* dose response study of delivery mode, pressure amplitude and contrast dose,” *Ultrasound Med Biol*, vol. 29, no. 9, pp. 1341-1349, 2003.
- [54] S. Datta, C.-C. Coussios, L. E. McAdory, J. Tan, T. Porter *et al.*, “Correlation of cavitation with ultrasound enhancement of thrombolysis,” *Ultrasound Med Biol*, vol. 32, no. 8, pp. 1257-1267, 2006.
- [55] S. Hernot, and A. L. Klibanov, “Microbubbles in ultrasound-triggered drug and gene delivery,” *Adv Drug Deliver Rev*, vol. 60, no. 10, pp. 1153-1166, 2008.

- [56] F. Forsberg, W. T. Shi, B. Jadidian, and A. A. Winder, "Multi-frequency harmonic arrays: initial experience with a novel transducer concept for nonlinear contrast imaging," *Ultrasonics*, vol. 43, no. 2, pp. 79-85, 2004.
- [57] W. T. Shi, F. Forsberg, R. Bautista, C. Vecchio, R. Bernardi *et al.*, "Image enhancement by acoustic conditioning of ultrasound contrast agents," *Ultrasound Med Biol*, vol. 30, no. 2, pp. 191-8, Feb, 2004.
- [58] A. Bouakaz, S. Frigstad, F. J. T. Cate, and N. D. Jong, "Super harmonic imaging: a new imaging technique for improved contrast detection," *Ultrasound Med Biol*, vol. 28, no. 1, pp. 59 - 68, 2002.
- [59] S. A. Sapareto, and W. C. Dewey, "Thermal dose determination in cancer therapy," *Int J Radiat Oncol Biol Phys*, vol. 10, no. 6, pp. 787-800, 1984.
- [60] S. Vaezy, R. Martin, P. Kaczkowski, G. Keilman, B. Goldman *et al.*, "Use of high-intensity focused ultrasound to control bleeding," *J Vasc Surg*, vol. 29, no. 3, pp. 533-542, 1999.
- [61] J. E. Kennedy, "High-intensity focused ultrasound in the treatment of solid tumours," *Nat Rev Cancer*, vol. 5, no. 4, pp. 321-327, 2005.
- [62] R. Illing, J. Kennedy, F. Wu, G. Ter Haar, A. Protheroe *et al.*, "The safety and feasibility of extracorporeal high-intensity focused ultrasound (HIFU) for the treatment of liver and kidney tumours in a Western population," *Brit J Cancer*, vol. 93, no. 8, pp. 890-895, 2005.

- [63] A. Blana, B. Walter, S. Rogenhofer, and W. F. Wieland, "High-intensity focused ultrasound for the treatment of localized prostate cancer: 5-year experience," *Urology*, vol. 63, no. 2, pp. 297-300, 2004.
- [64] G. T. Haar, and C. Coussios, "High intensity focused ultrasound: Physical principles and devices," *Int J Hyperther*, vol. 23, no. 2, pp. 89 - 104, 2007.
- [65] S. Bobkova, A. Shaw, L. Gavrilov, V. Khokhlova, J. Hand *et al.*, "Feasibility of HIFU tissue ablation in the presence of ribs using a 2D random phased array," in *Aip Conf Proc*, 2010, pp. 27.
- [66] Y. Jing, F. C. Meral, and G. T. Clement, "Time-reversal transcranial ultrasound beam focusing using a k-space method," *Phys Med Biol*, vol. 57, no. 4, pp. 901, 2012.
- [67] J. Kennedy, G. Ter Haar, and D. Cranston, "High intensity focused ultrasound: surgery of the future?," *Brit J Radiol*, 2014.
- [68] K. D. Evans, B. Weiss, and M. Knopp, "High-Intensity Focused Ultrasound (HIFU) for Specific Therapeutic Treatments: A Literature Review," *J Diagn Med Sonog*, vol. 23, no. 6, pp. 319-327, 2007.
- [69] A. Arefiev, F. Prat, J. Y. Chapelon, J. Tavakkoli, and D. Cathignol, "Ultrasound-induced tissue ablation: studies on isolated, perfused porcine liver," *Ultrasound Med Biol*, vol. 24, no. 7, pp. 1033-1043, 1998.
- [70] N. McDannold, G. Clement, P. Black, F. Jolesz, and K. Hynynen, "Transcranial MRI-guided focused ultrasound surgery of brain tumors: Initial findings in three patients," *Neurosurgery*, vol. 66, no. 2, pp. 323-332, 2011.

- [71] C. M. C. Tempny, N. J. McDannold, K. Hynynen, and F. A. Jolesz, "Focused ultrasound surgery in oncology : overview and principles," *Radiology*, vol. 259, no. 1, pp. 39-56, 2011.
- [72] C. Bohris, W. G. Schreiber, J. u. Jenne, I. Simiantonakis, R. Rastert *et al.*, "Quantitative MR temperature monitoring of high-intensity focused ultrasound therapy," *Magnet Reson Imaging*, vol. 17, no. 4, pp. 603-610, 1999.
- [73] S. Vaezy, X. Shi, R. W. Martin, E. Chi, P. I. Nelson *et al.*, "Real-time visualization of high-intensity focused ultrasound treatment using ultrasound imaging," *Ultrasound Med Biol*, vol. 27, no. 1, pp. 33-42, 2001.
- [74] R. E. Kumon, M. S. R. Gudur, Y. Zhou, and C. X. Deng, "High-Frequency Ultrasound M-Mode Imaging for Identifying Lesion and Bubble Activity During High-Intensity Focused Ultrasound Ablation," *Ultrasound Med Biol*, vol. 38, no. 4, pp. 626-641, 2012.
- [75] H. Azhari, "Feasibility study of ultrasonic computed tomography-guided high-intensity focused ultrasound," *Ultrasound Med Biol*, vol. 38, no. 4, pp. 619-625, 2012.
- [76] A. Fenster, and D. B. Downey, "3-D Ultrasound Imaging: A Review," *IEEE Eng Med Biol Magazine*, vol. 15, no. 6, pp. 41 - 45, 1996.
- [77] C. R. Merritt, "Doppler color flow imaging," *J Clin Ultrasound*, vol. 15, no. 9, pp. 591-597, 1987.
- [78] P. J. A. Frinking, A. Bouakaz, J. Kirkhorn, F. J. T. Cate, and N. Jong, "Ultrasound contrast imaging: current and new potential methods," *Ultrasound Med Biol*, vol. 26, no. 6, pp. 965-975, 2000.

- [79] I. G. Calasso, W. Craig, and G. J. Diebold, "Photoacoustic point source," *Phys Rev Lett*, vol. 86, no. 16, pp. 3550, 2001.
- [80] G. Lerosey, and M. Fink, "Acousto-optic imaging: merging the best of two worlds," *Nat Photon*, vol. 7, no. 4, pp. 265-267, 2013.
- [81] T. S. Desser, and R. B. Jeffrey, "Tissue harmonic imaging techniques: physical principles and clinical applications," in *Seminars in Ultrasound, CT and MRI*, 2001, pp. 1-10.
- [82] P. Wells, "Ultrasound imaging," *Phys Med Biol*, vol. 51, no. 13, pp. R83, 2006.
- [83] J. M. Tobis, J. Mallery, D. Mahon, K. Lehmann, P. Zalesky *et al.*, "Intravascular ultrasound imaging of human coronary arteries in vivo. Analysis of tissue characterizations with comparison to in vitro histological specimens," *Circulation*, vol. 83, no. 3, pp. 913-926, 1991.
- [84] C. J. Slager, J. J. Wentzel, J. C. Schuurbiens, J. A. Oomen, J. Kloet *et al.*, "True 3-dimensional reconstruction of coronary arteries in patients by fusion of angiography and IVUS (ANGUS) and its quantitative validation," *Circulation*, vol. 102, no. 5, pp. 511-516, 2000.
- [85] S. Vallabhajosula, and V. Fuster, "Atherosclerosis: imaging techniques and the evolving role of nuclear medicine," *J Nucl Med*, vol. 38, no. 11, pp. 1788-1796, 1997.
- [86] J. Ma, K. H. Martin, P. A. Dayton, and X. Jiang, "A preliminary engineering design of intravascular dual-frequency transducers for contrast enhanced acoustic angiography

- and molecular imaging,” *IEEE Trans Ultrason Ferroelectr Freq Control*, vol. 61, no. 5, pp. 870 - 880, 2014.
- [87] M. B. Steer, *Microwave and RF design : a systems approach*, 2 ed., New Jersey: SciTech, 2013.
- [88] W. J. Fry, W. H. Mosberg, J. W., and F. J. Fry, “Production of focal destructive lesions in the central nervous system with ultrasound,” *J Neurosurg*, vol. 336, no. 119, pp. 471-478, 1954.
- [89] Z. B. Wang, F. Wu, Z. L. Wang, Z. Zhang, J. Z. Zou *et al.*, “Targeted damage effects of high intensity focused ultrasound (HIFU) on liver tissues of Guizhou Province miniswine.” *Ultrason Sonochem*, vol. 4, no. 2, pp. 181-182, 1997.
- [90] M. L. Guzman, “The sesquiterpene lactone parthenolide induces apoptosis of human acute myelogenous leukemia stem and progenitor cells,” *Blood*, vol. 105, no. 11, pp. 4163-4169, 2005.
- [91] F. Marquet, M. Pernot, J. F. Aubry, G. Montaldo, L. Marsac *et al.*, “Non-invasive transcranial ultrasound therapy based on a 3D CT scan: protocol validation and in vitro results.” *Physics in Med Biol*, vol. 54, no. 9, pp. 2597-2613, 2009.
- [92] C. D. Herickhoff, G. A. Grant, G. W. Britz, and s. W. Smith, “Dual-mode IVUS catheter for intracranial image-guided hyperthermia: feasibility study,” *IEEE Trans Ultrason Ferroelectr Freq Control*, vol. 57, pp. 2572 - 2584, 2010.

- [93] P. He, W. Shou, S. Duan, and R. M. Xia, "Dual-frequency high intensity focused ultrasound (HIFU) accelerating therapy," in *IEEE Eng Med Bio Soc*, 2005, pp. 213-216.
- [94] P. A. Tatake, and A. B. Pandit, "Modelling and experimental investigation into cavity dynamics and cavitation yield : influence of dual frequency ultrasound sources," *Chem Eng Sci*, vol. 57, pp. 4987-4995, 2002.
- [95] L. Zhang, H. Zhu, C. Jin, K. Zhou, K. Li *et al.*, "High-intensity focused ultrasound (HIFU): effective and safe therapy for hepatocellular carcinoma adjacent to major hepatic veins.," *Eur Radiol*, vol. 19, no. 2, pp. 437-445, 2009.
- [96] A. Rybyanets, A. Nasedkin, A. Rybyanets, M. Lugovaya, and T. Domashenkina, "Multi-frequency harmonics technique for HIFU tissue treatment," in *2009 IEEE Int Ultrason Symp*, 2009, pp. 1765-1768.
- [97] G. Lerneti, P. Ciuti, N. V. Dezhkunov, M. Reali, A. Francescutto *et al.*, "Enhancement of high-frequency acoustic cavitation effects by a low-frequency stimulation.," *Ultrason Sonochem*, vol. 4, no. 3, pp. 263-268, 1997.
- [98] C. H. Farny, R. G. Holt, and R. A. Roy, "The correlation between bubble-enhanced HIFU heating and cavitation power.," *IEEE Trans Bio-med Eng*, vol. 57, no. 1, pp. 175-184, 2010.
- [99] L. Carpendo, P. Ciuti, A. Francescutto, G. Lerneti, and G. K. Johri, "Space-time interaction of two ultrasonic fields and sonoluminescence during transient cavitation in distilled water," *Acoust Lett*, vol. 11, pp. 178-181, 1987.

- [100] R. Feng, Y. Zhao, C. Zhu, and T. J. Mason, "Enhancement of ultrasonic cavitation yield by multi-frequency sonication.," *Ultrason Sonochem*, vol. 9, no. 5, pp. 231-236, 2002.
- [101] S. Guo, X. Jiang, and W. Lin, "Tissue Ablation Using Multi-frequency Focused Ultrasound," in *IEEE Conf Pub*, 2011, pp. 2177-2180.
- [102] M. Alamolhoda, M. Mokhtari-Dizaji, A. H. Barati, and H. Hasanzadeh, "Comparing the in vivo sonodynamic effects of dual- and single-frequency ultrasound in breast adenocarcinoma," *J Med Ultrason*, vol. 39, no. 3, pp. 115-125, 2012.
- [103] P. Z. He, R. M. Xia, S. M. Duan, W. D. Shou, and D. C. Qian, "The affection on the tissue lesions of difference frequency in dual-frequency high-intensity focused ultrasound (HIFU)," *Ultrason Sonochem*, vol. 13, no. 4, pp. 339-344, 2006.
- [104] R. Chopra, C. Luginbuhl, F. S. Foster, and M. J. Bronskill, "Multifrequency ultrasound transducers for conformal interstitial thermal therapy.," *IEEE Trans Ultrason Ferroelectr Freq Control*, vol. 50, no. 7, pp. 881-889, 2003.
- [105] R. Krimholtz, D. A. Leedom, and G. L. Mattaei, "New equivalent circuits for elementary piezoelectric transducers," *Electron Lett*, vol. 41, no. 13, pp. 398-399, 1970.
- [106] A. Jensen, "Calculation of pressure fields from arbitrarily shaped, apodized, and excited ultrasound transducers," *IEEE Trans Ultrason Ferroelectr Freq Control*, vol. 39, no. 2, pp. 262-267, 1992.
- [107] G. R. Lockwood, and F. S. Foster, "Modeling and optimization of high-frequency ultrasound transducers," *IEEE Trans Ultrason Ferroelectr Freq Control*, vol. 41, no. 2, pp. 225-230, 1994.

- [108] M. R. Bailey, J. A. Reed, B. W. Cunitz, P. J. Kaczkowski, and L. A. Crum, "Effects of nonlinear propagation, cavitation, and boiling in lesion formation by high intensity focused ultrasound in a gel phantom," *J Acoust Soc Am*, vol. 119, no. 3, pp. 1834 - 1848, 2005.
- [109] G. Ierretti, P. Ciuti, N. Dezhkunov, M. Reali, A. Francescutto *et al.*, "Enhancement of high-frequency acoustic cavitation effects by a low-frequency stimulation," *Ultrason Sonochem*, vol. 4, no. 3, pp. 263-268, 1997.
- [110] R. Feng, Y. Zhao, C. Zhu, and T. Mason, "Enhancement of ultrasonic cavitation yield by multi-frequency sonication," *Ultrason Sonochem*, vol. 9, no. 5, pp. 231-236, 2002.
- [111] M. Naghavi, "From Vulnerable Plaque to Vulnerable Patient: A Call for New Definitions and Risk Assessment Strategies: Part I," *Circulation*, vol. 108, no. 14, pp. 1664-1672, 2003.
- [112] A. S. Go, D. Mozaffarian, V. L. Roger, E. J. Benjamin, J. D. Berry *et al.*, "Heart disease and stroke statistics--2014 update: a report from the American Heart Association," *Circulation*, vol. 129, no. 3, pp. e28, 2014.
- [113] R. Glaser, "Clinical Progression of Incidental, Asymptomatic Lesions Discovered During Culprit Vessel Coronary Intervention," *Circulation*, vol. 111, no. 2, pp. 143-149, 2005.
- [114] D. E. Goertz, M. E. Frijlink, D. Tempel, V. Bhagwandas, A. Gisolf *et al.*, "Subharmonic contrast intravascular ultrasound for vasa vasorum imaging," *Ultrasound Med Biol*, vol. 33, no. 12, pp. 1859-1872, Dec, 2007.

- [115] P. Constantinides, "Cause of thrombosis in human atherosclerotic arteries," *Am J Cardiol*, vol. 66, no. 16, pp. G37 - G40, 1990.
- [116] M. Naghavi, *Asymptomatic Atherosclerosis: Pathophysiology, Detection and Treatment*: Humana Press, 2010.
- [117] K. S. Moulton, K. Vakili, D. Zurakowski, M. Soliman, C. Butterfield *et al.*, "Inhibition of plaque neovascularization reduces macrophage accumulation and progression of advanced atherosclerosis," *P Natl Acad Sci USA*, vol. 100, no. 8, pp. 4736 - 4741, 2003.
- [118] R. Virmani, "Atherosclerotic Plaque Progression and Vulnerability to Rupture: Angiogenesis as a Source of Intraplaque Hemorrhage," *Arterioscl Throm Vas*, vol. 25, no. 10, pp. 2054-2061, 2005.
- [119] F. D. Kolodgie, H. K. Gold, A. P. Burke, D. R. Fowler, H. S. Kruth *et al.*, "Intraplaque hemorrhage and progression of coronary atheroma," *N Engl J Med*, vol. 349, no. 24, pp. 2316 - 2325, 2003.
- [120] J. Milei, J. C. Parodi, G. F. Alonso, A. Barone, D. Grana *et al.*, "Carotid rupture and intraplaque hemorrhage: immunophenotype and role of cells involved," *Am Heart J*, vol. 136, no. 6, pp. 1096 - 1105, 1998.
- [121] P. R. Moreno, and V. Fuster, "New aspects in the pathogenesis of diabetic atherothrombosis," *J Am Coll Cardiol*, vol. 44, no. 12, pp. 2293 - 2300, 2004.
- [122] F. A. Jaffer, P. Libby, and R. Weissleder, "Molecular and cellular imaging of atherosclerosis: emerging applications," *J Am Coll Cardiol*, vol. 47, no. 7, pp. 1328 - 1338, 2006.

- [123] J. R. Lindner, "Molecular imaging with contrast ultrasound and targeted microbubbles," *J Nucl Cardiol*, vol. 11, no. 2, pp. 215-21, Mar-Apr, 2004.
- [124] R. P. Choudhury, V. Fuster, and Z. A. Fayad, "Molecular, cellular and functional imaging of atherothrombosis," *Nat Rev Drug Discov*, vol. 3, no. 11, pp. 913-25, Nov, 2004.
- [125] R. Gessner, and P. A. Dayton, "Advances in molecular imaging with ultrasound," *Mol Imaging*, vol. 9, no. 3, pp. 117-27, Jun, 2010.
- [126] G. L. ten Kate, E. J. G. Sijbrands, R. Valkema, F. J. ten Cate, S. B. Feinstein *et al.*, "Molecular imaging of inflammation and intraplaque vasa vasorum: A step forward to identification of vulnerable plaques?," *J Nucl Cardiol*, vol. 17, no. 5, pp. 897- 912, 2010.
- [127] R. C. Gessner, S. R. Aylward, and P. A. Dayton, "Mapping microvasculature with acoustic angiography yields quantifiable differences between healthy and tumor-bearing tissue volumes in a rodent model," *Radiology* vol. 264, no. 3, pp. 733 - 740, 2012.
- [128] S. B. Feinstein, "Contrast Ultrasound Imaging of the Carotid Artery Vasa Vasorum and Atherosclerotic Plaque Neovascularization," *J Am Coll Cardiol*, vol. 48, no. 2, pp. 236-243, 2006.
- [129] D. Staub, A. F. L. Schinkel, B. Coll, S. Coli, A. F. W. van der Steen *et al.*, "Contrast-Enhanced Ultrasound Imaging of the Vasa Vasorum: from early atherosclerosis to the

- identification of unstable plaques.,” *JACC: Cardiovascular Imaging*, vol. 3, no. 7, pp. 761-771, 2010.
- [130] I.-K. Jang, B. E. Bouma, D.-H. Kang, S.-J. Park, S.-W. Park *et al.*, “Visualization of coronary atherosclerotic plaques in patients using optical coherence tomography: comparison with intravascular ultrasound,” *J Am Coll Cardiol*, vol. 39, no. 4, pp. 604-609, 2002.
- [131] S. E. Nissen, J. C. Gurley, C. L. Grines, D. C. Booth, R. McClure *et al.*, “Intravascular ultrasound assessment of lumen size and wall morphology in normal subjects and patients with coronary artery disease,” *Circulation*, vol. 84, no. 3, pp. 1087-1099, 1991.
- [132] J. D. Kasprzak, B. Paelinck, F. J. Ten Cate, W. B. Vletter, N. de Jong *et al.*, “Comparison of native and contrast-enhanced harmonic echocardiography for visualization of left ventricular endocardial border,” *Am J Cardiol*, vol. 83, no. 2, pp. 211 - 217, 1999.
- [133] D. E. Goertz, M. E. Frijlink, D. Tempel, L. C. van Damme, R. Krams *et al.*, “Contrast harmonic intravascular ultrasound: a feasibility study for vasa vasorum imaging,” *Invest Radiol*, vol. 41, no. 8, pp. 631 - 638, 2006.
- [134] N. Jong, A. Bouakaz, and F. J. T. Cate, “Contrast harmonic imaging,” *Ultrasonics*, vol. 40, pp. 567 - 573, 2002.
- [135] A. Bouakaz, B. J. Krenning, W. B. Vletter, F. J. T. Cate, and N. D. Jong, “Contrast superharmonic imaging: A feasibility study,” *Ultrasound Med Biol*, vol. 29, no. 4, pp. 547-553, 2003.

- [136] D. E. Kruse, and K. W. Ferrara, "A new imaging strategy using wideband transient response of ultrasound contrast agents," *IEEE Trans Ultrason Ferroelectr Freq Control*, vol. 52, no. 8, pp. 1320-1329, 2005.
- [137] R. Gessner, M. Lukacs, M. Lee, E. Cherin, F. S. Foster *et al.*, "High-resolution, high-contrast ultrasound imaging using a prototype dual-frequency transducer: in vitro and in vivo studies," *IEEE Trans Ultrason Ferroelectr Freq Control*, vol. 57, no. 8, pp. 1772 - 1781, 2010.
- [138] H. M. Kwon, G. Sangiorgi, E. L. Ritman, C. McKenna, D. R. Holmes Jr *et al.*, "Enhanced coronary vasa vasorum neovascularization in experimental hypercholesterolemia," *J Clin Invest*, vol. 101, no. 8, pp. 1551, 1998.
- [139] J. Ma, Z. Wang, and X. Jiang, "Design, fabrication, and test of a small aperture, dual frequency ultrasound transducer," in Proc of SPIE, San Diego, 2013, pp. 86951H.
- [140] J. Ma, X. Jiang, K. Heath Martin, and P. A. Dayton, "Small aperture, dual frequency ultrasound transducers for intravascular contrast imaging," in 2013 IEEE Int Ultrason Symp (IUS), 2013, pp. 769-772.
- [141] P. L. M. J. v. Neer, G. Matte, M. G. Danilouchkine, C. Prins, F. v. d. Adel *et al.*, "Super-harmonic imaging: development of an interleaved phase-array transducer," *IEEE Trans Ultrason Ferroelectr Freq Control*, vol. 57, no. 2, pp. 455 - 468, 2010.
- [142] K. Martin, B. Lindsey, J. Ma, M. Lee, S. Li *et al.*, "Dual-Frequency Piezoelectric Transducers for Contrast Enhanced Ultrasound Imaging," *Sensors*, vol. 14, no. 11, pp. 20825-20842, 2014.

- [143] T. Azuma, M. Ogihara, J. Kubota, A. Sasaki, S.-i. Umemura *et al.*, “Dual-frequency ultrasound imaging and therapeutic bilaminar array using frequency selective isolation layer,” *IEEE Trans Ultrason Ferroelectr Freq Control*, vol. 57, no. 5, pp. 1211 - 1224, 2010.
- [144] H. M. Garcia-Garcia, M. A. Costa, and P. W. Serruys, “Imaging of coronary atherosclerosis: intravascular ultrasound,” *Eur Heart J*, vol. 31, no. 20, pp. 2456 - 2469, Oct, 2010.
- [145] K. K. Shung, J. M. Cannata, and Q. F. Zhou, “Piezoelectric materials for high frequency medical imaging applications: A review,” *J of Electroceram*, vol. 19, no. 1, pp. 141-147, 2007.
- [146] J. Ma, S. Li, Z. Wang, and X. Jiang, “Anti-matching design for wave isolation in dual frequency transducer for intravascular super-harmonic imaging,” in Proc ASME 2014 IMECE, Montreal, Canada, 2014, in press, pp.
- [147] Y. Li, J. Ma, K. H. Martin, H. Choi, P. A. Dayton *et al.*, “A configurable dual-frequency transmit/receive system for acoustic angiography imaging,” in 2014 IEEE Int Ultrason Symp (IUS), 2014, pp. 731-733.
- [148] M. A. Borden, M. R. Sarantos, S. M. Stieger, S. I. Simon, K. W. Ferrara *et al.*, “Ultrasound radiation force modulates ligand availability on targeted contrast agents,” *Mol Imaging*, vol. 5, no. 3, pp. 139-47, Jul, 2006.

- [149] R. C. Gessner, C. B. Frederick, F. S. Foster, and P. A. Dayton, "Acoustic angiography: a new imaging modality for assessing microvasculature architecture," *Int J Biomed Imaging*, vol. 2013, 2013.
- [150] R. C. Gessner, C. B. Frederick, F. S. Foster, and P. A. Dayton, "Acoustic angiography: a new imaging modality for assessing microvasculature architecture," *Int J Biomed Imaging*, vol. 2013, pp. 14, 2013.
- [151] J. Ma, X. Jiang, K. H. Martin, P. A. Dayton, Y. Li *et al.*, "Dual frequency transducers for intravascular ultrasound super-harmonic imaging and acoustic angiography," in 2014 IEEE Int Ultrason Symp (IUS), 2014, pp. 675-678.
- [152] R. Lerch, "Simulation of piezoelectric devices by two-and three-dimensional finite elements," *IEEE Trans Ultrason Ferroelectr Freq Control*, vol. 37, no. 3, pp. 233-247, 1990.
- [153] A. A. Doinikov, J. F. Haac, and P. A. Dayton, "Resonance frequencies of lipid-shelled microbubbles in the regime of nonlinear oscillations," *Ultrasonics*, vol. 49, no. 2, pp. 263-268, 2009.
- [154] W. P. Mason, "The approximate network of acoustic filters," *Bell Syst Tech J*, vol. 9, no. 2, pp. 332 - 340, 1930.
- [155] L. E. Kinsler, A. R. Frey, A. B. Coppens, and J. V. Sanders, *Fundamentals of Acoustics*, 4 ed., pp. 153, United States of America: John Wiley & Sons, Inc., 2000.

- [156] H. Wang, T. Ritter, W. Cao, and K. K. Shung, "High frequency properties of passive materials for ultrasonic transducers.," *IEEE Trans Ultrason Ferroelectr Freq Control*, vol. 48, no. 1, pp. 78-84, 2001.
- [157] G. Kossoff, "The Effects of Backing and Matching on the Performance of Piezoelectric Ceramic Transducers," *IEEE Trans Son Ultrason*, vol. 13, no. 1, pp. 20-30, 1966.
- [158] T. Inoue, M. Ohta, and S. Takahashi, "Design of Ultrasonic Transducers with Multiple Acoustic Matching Layers for Medical Application," *IEEE Trans Ultrason Ferroelectr Freq Control*, vol. 34, no. 1, pp. 9-16, 1987.